POLITECNICO DI MILANO

Facoltà di Ingegneria Industriale

Corso di Laurea in
Ingegneria Meccanica

Train induced ground vibration: a hybrid time and frequency domain modelling technique

Relatore: Prof. Andrea Collina
Co-relatore: Prof. David J. Thompson
Co-relatore: Dr. Giacomo Squicciarini

Tesi di Laurea di:
Matteo Montagna Matr. 765538

Anno Accademico 2012-2013

Alla mia famiglia

Acknowledgements

At first I would like to thank professor Andrea Collina and professor David Thompson for supervising, helping and guiding me during my work of thesis. A special thanks goes also to Giacomo Squicciarini that helped me during my work in many ways. Then I would like to thank Samuele Usberti that lived with me in Southampton for the past 6 months sharing joys and tough moments. A big thanks to my family that always supported me during the years of university and encouraged me during the hard moments. Thanks also to Laura Broggi for helping me to understand what is more important and for comforting me during periods of tough work. A special thanks to Samuele Reggiani and his family for hosting me in their home when I was homeless. Thanks to Sonia Musicco and her family for being my step mom and family. Thanks to Andrea Erba, Andrea Pellecchia, Andrea Ragazzini, Giacomo Merlini, Pietro Pierpaoli, Riccardo Zanforlin, Federico Perelli, Saul Bosatelli, Lorenzo Pasoli, Emanuele Clerici, Andrea Trianni, Filippo Casadei, Marie Chierichetti, Andrea Zapparoli, and all my friends that I have met during these many years of university.

Contents

Abstract

Ground vibration from trains is an increasingly important environmental problem. This study investigates an efficient methodology to predict the levels of vibration induced by a train pass-by. The vibration induced by trains can be divided in two groups: perceptible vibration, that is confined in the range 2-80 Hz, and the ground-borne noise, which is due to vibration in the range 20-200 Hz and can induce noise radiation from the walls and floors of buildings close to the railway. Two existing softwares have been used during this work of thesis to study this phenomenon: one simulates the passage of the train and operates in the time domain developed at Politecnico di Milano; the other solves the propagation of waves in the ground, developed at University of Southampton, and works in the frequency/wavenumber domain. A post-processing method of the results from the two softwares, called the hybrid method, has been implemented, using some existing theory, in order to obtain the levels of vibration of the ground at a certain receiver, due to the passage of the train. Since this methodology can be applied for any configuration of train and ground, results of the hybrid model, for different configurations, are reported. The two main examples are a case of track lying on a multi-layer ground and a case of an underground tunnel.

Key words: ground vibration, hybrid model, time domain, frequency wavenumber domain, wave propagation in ground, finite element boundary element method

Sommario

Le vibrazioni indotte dal passaggio di treni stanno diventando un problema rilevante per il confort delle aree ad alta densità di popolazione e nelle aree industriali. In questa tesi è proposto un nuovo metodo per calcolare i livelli di vibrazione del terreno in una qualsiasi posizione, indotti dal passaggio di un treno. Le vibrazioni indotte dai treni possono essere divise in due gruppi: vibrazioni che possono essere percepite, che esistono in un range di frequenze comprese tra 2-80 Hz, e ground-borne noise, che sono vibrazioni in un range 20-200 Hz e possono generare emissione acustica dalle pareti e dal pavimento all'interno delle strutture vicino alle linee ferroviarie. Per questo lavoro di tesi sono stati utilizzati due software già esistenti per studiare questo fenomeno: uno che simula il passaggio del treno e opera nel dominio del tempo, sviluppato presso il Politecnico di Milano; l'altro risolve il problema di propagazione delle onde nel terreno e lavora nel dominio delle frequenze numeri d'onda, sviluppato presso la University of Southampton. È stato quindi implementato un metodo di post elaborazione dei risultati dei due software, chiamato modello ibrido, basato su della teoria già esistente, in grado di predire i livelli di vibrazione in una certa posizione dovuti al passaggio del treno. Dato che questa metodologia è molto generale sono proposti risultati per diverse configurazioni di terreno alla fine di questo lavoro.

Parole chiave: vibrazioni nel terreno, modello ibrido, dominio del tempo, dominio delle frequenze, propagazione delle onde nel terreno, elementi finiti boundary element

Estratto in lingua italiana

Negli ultimi anni la preoccupazione della società riguardo i sistemi di trasporto ferroviari stanno crescendo in particolare a causa della tendenza all'aumento della velocità. Insieme con questo c'è l'introduzione di leggi sempre più stringenti riguardo agli standard ambientali. Le vibrazioni e il rumore sono dunque un tema molto importate per le compagnie ferroviarie.

La competitività del trasporto su strada ferrata rispetto a tutti gli altri tipi di trasporto è accentuata dalla sua abilità di operare dal cuore degli stabilimenti urbani e commerciali. Per poter raggiungere questi risultati però spesso è necessaria la costruzione di tunnel sotterranei, sopratutto nelle grandi città. Questo ha portato a comprendere che le vibrazioni dovute al passaggio dei treni nei tunnel possono essere un problema molto rilevante, sopratutto sulle linee ad alta percorrenza. Queste vibrazioni coprono un intervallo di frequenze che vai dai 2 ai 200 Hz, [1] e le frequenze che si trovano nel range tra i 20 e i 200 Hz possono produrre un rumore udibile all'interno delle costruzioni circostanti durante il passaggio del treno, questo viene chiamato ground-borne noise. Inoltre possono essere presenti anche vibrazioni a più bassa frequnza, nel range 2-80 Hz, che sono percepibili dal corpo umano.

Questa tesi è incentrata sul ground-borne noise prodotto dal passaggio del treno, quindi nel range di frequenze 20-200 Hz. Questo fenomeno è principalmente eccitato dalle irregolaità presenti sulla ruota e sulla rotaia che genera delle forze che vengono trasmesse al terreno e possono generare delle onde che propagano in esso.

Storicamente ci sono stati due tipi di approcci a questo problema: l'approccio nel dominio del tempo che studia dettagliatamente la dinamica del veicolo e il meccanismo di interazione ruota-rotaia quindi la generazione delle forze di contatto; e l'approccio nel dominio delle frequenze-numeri d'onda che studia in maniera efficiente la propagazione delle onde nel terreno.

Il principale obiettivo di questa tesi è quello di presentare una metodologia in grado di accoppiare i risultati di questi due mondi. Utilizzare un modello nel dominio del tempo in grado di simulare la dinamica del veicolo e ricavare le forze derivanti dal passaggio del treno. Utilizzare un modello nel dominio delle frequenze-numeri d'onda per ottenere le funzioni di trasferimento del terreno tra il punto di forzamento e un punto di interesse. Attraverso una post elaborazione dei dati ottenuti dai due modelli è possibile ottenere i livelli di vibrazione del punto di interesse scelto.

Nel Capitolo 1 è stata fatta una revisione della letteratura a riguardo del problema del ground-born noise. Nella prima parte è stato trattato l'approccio nel dominio del tempo che è incentrato sulla dinamica del veicolo e sulle forze di contatto. Viene presentata una carrellata dei diversi modelli per il contatto e per lo studio della dinamica del veicolo sviluppati negli anni arrivando poi a descrivere il modello sviluppato presso il Politecnico di Milano e utilizzato in questo lavoro di tesi per simulare il passaggio del treno sui binari. La seconda parte, invece, descrive i diversi approcci utilizzati per la modellazione della propagazione delle onde nel terreno. Qui sono prensetati una serie di modelli analitici, numerici e empirici che sono stati studiati negli ultimi decenni. Questi modelli possono essere in 2D, 3D o il così detto 2.5D che schematizza una sezione bidimensionale del terreno e ricostruisce la risposta nella terza dimensione nel dominio dei numeri d'onda assumendo omogenea la struttura nella terza dimensione. Questa metodologia è più efficiente dal punto di vista computazionale di una struttura tridimensionale dato che il numero di nodi necessari per schematizzare la sezione è contenuto, ma a differenza dei modelli bidimensionali è in grado di studiare la propagazione delle onde in tutte le direzioni. Un modello di questo genere, sviluppato dalla University of Southampton, verrà utilizzato in questa tesi per lo studio delle risposte in frequenza del terreno. L'ultima parte presenta una metodologia ancora in fase di sviluppo in grado di accoppiare le forze risultanti dal modello nel dominio del tempo con le funzioni di trasferimento del terreno derivanti dal modello che simula il terreno nel dominio delle frequenze-numeri d'onda e restituisce lo spettro della risposta del terreno in un punto stabilito, vedi fig. 1.2.

Il Capitolo 2 descrive in dettaglio i modelli utilizzati per questo lavoro di tesi. Il modello sviluppato dal Politecnico di Milano per la simulazione del passaggio del treno è stato sviluppato nel dominio del tempo per poter tenere conto anche delle non linarità dovute al contatto ruota rotaia. Il modello è basato su una rappresentazione a elementi finiti della struttura e della rotaia mentre utilizza un modello multi-body misto rigido flessibile per descrivere la dinamica del treno. Le equazioni di moto di questi due sistemi sono scritte separatamente con le forze di contatto che accoppiano i due sistemi. Il modello di contatto è basato su un multi contatto Hertziano non lineare, questo significa che il coefficiente della formula del contatto di Hertz è legato alle forze normali da una potenza di 3/2 alla compenetrazione elastica di ruota e rotaia. Questo modello restituisce come outputs lo spostamento, velocità e accelerazione di tutti i nodi della struttura FEM, spostamento, velocità e accelerazione di tutti i punti del modello multi body del veicolo e le forze dovute al contatto ruota rotaia e ai componenti elastici della struttura a elementi finiti. Il modello sviluppato dall'Institute of Sound and Vibration della University of Southampton, detto WANDS, è un modello 2.5D che schematizza la sezione del terreno attraverso elementi finiti e boundary element (BE), mentre la terza direzione è descritta nel dominio delle delle frequenze numeri d'onda, questo implica che la struttura nella terza dimensione sia considerata omogenea. I BE sono degli elementi che descrivono solo il contorno dell'oggetto desiderato, questo genera un enorme risparmio in numero di nodi presenti nel modello e quindi di tempo computazionale. Questi diventano molto utili per descrivere il terreno che viene considerato infinito e quindi descritto da un numero molto contenuto di nodi, al contrario nei modelli 3D la descrizione dettagliata del terreno diventa molto onerosa dal punto di vista computazionale. Inoltre sono stati sviluppati, per questo modello, degli elementi detti di bordo che sono in grado di assorbire completamente le onde incidenti senza rifletterle, questo rende possibile descrivere un terreno infinito anche con un numero limitato di nodi al bordo. La risposta forzata del terreno viene calcolata per tutte le frequenze e per tutti i numeri d'onda, che vengono dati in ingresso al programma, e ricostruita nello spazio attravento l'antitrasformata di Fourier. Infine viene spiegato in dettaglio il modello, così detto ibrido, che accoppia i risultati del modello nel dominio del tempo con i risultati del modello nel dominio delle frequenze e numeri d'onda per dare la risposta del terreno in un determinato punto causata dal passaggio del treno. Data la funzione di trasferimento tra il punto di applicazione della forza e un punto qualsiasi della struttura è possibile ottenere la risposta nel punto di interesse moltiplicando la funzione di trasferimento per lo spettro della forza. Dato che nel nostro cosa la funzione di trasferimento è la mobilità del terreno la risposta che si ottiene è la velocità del punto di interesse.

$$v_2(\omega) = Y_{12}(\omega) F(\omega)$$

Dove $Y_{12}(\omega)$ è la mobilità tra il punto 1, di applicazione della forza, e il punto 2, di interesse sulla struttura. Se il sistema è lineare allora è anche possibile applicare la sovrapposizione degli effetti sommando le risposte dovute al forzamento in diversi punti della struttura per ricostruire la risposta completa nel punto 2. Spesso è più significativo guardare al contenuto energetico del segnale trasformando la risposta v_2 in una PSD. Questo è il concetto che sta alla base del modello ibrido proposto in questa tesi. È possibile ricostruire il contenuto energetico di un qualsiasi punto nel terreno conoscendo le forze trasmesse a terra che derivano dalla posizione delle traversine e le funzioni di trasferimento tra la traversina e il punto di interesse nel terreno. Utilizzando gli auto e cross spettri delle forze derivanti dalle traversine non si perde la dipendenza del moto del treno nel dominio del tempo dato che lo sfasamento delle forze è contenuto dei cross spettri.

$$S_{ww} = \boldsymbol{Y}^H \boldsymbol{S}_{FF} \boldsymbol{Y}$$

Dove S_{ww} è la PSD della risposta nel punto di interesse, e $\boldsymbol{S}_{FF}$ è la matrice contenente gli auto e cross spettri delle forze derivanti dalle traversine. Dato che le forze dal modello di interazione treno armamento vengono ottenute nel dominio del tempo queste vanno convertite nel dominio delle frequenze attraverso la trasformata di Fourier.

Il Capitolo 3 presenta in dettaglio il modello che lavora nel dominio del tempo. La prima parte presenta presenta i vari modelli a elementi finiti che sono stati sviluppati durante questo lavoro di tesi per poter condurre le analisi nel dominio del tempo. Tre diversi tipi di modelli per questo motivo sono stati implementati. Il primo e più semplice rappresenta un binario, descritto da degli elementi finiti di tipo trave di Eulero-Bernulli, semplicemente vincolato, tramite delle molle, a un terreno rigido. Questa struttura ha dato la possibilità di confrontare le risposte in frequenza ottenute attraverso il modello a elementi finiti con le risposte in frequeza ottenute con dei modelli analitici più sofisticati, che ad esempio considerano la rotaia come una trave di Timoshenko, che hanno confermato che, nel campo delle vibrazioni strutturali come il ground-borne noise, anche dei modelli semplificati per la rotaia posso dare dei risultati molto validi dato che il range di frequenze è limitato. Successivamente vengono proposti due casi più complessi che si presentano come delle applicazioni particolari: uno dove accoppiata con il binario si trova la struttura a elementi finiti di un tunnel sotterraneo, questo verrà utilizzato per investigare i livelli di vibrazione dovuti al passaggio di un treno metropolitano; mentre il secondo caso presenta sempre la stessa struttura a elementi finiti del tunnel ma sul binario si trova una irregolarità dovuta a una giunzione. La seconda parte del capitolo descrive i risultati dell'integrazione nel dominio del tempo. Anche in questo caso per meglio comprendere i risutati delle simulzioni nel dominio del tempo è stato preparato anche un modello analitico semplificato che genera una previsione delle forze di contato scambiate tra la ruota e la rotaia. È stato così possibile anche un confronto tra i risultati dell'integrazione nel dominio del tempo con i risultati ottenuti dal modello analitico semplificato delle forze di contatto. I risultati prosposti sono le storie temporali e gli spettri delle forze di contatto e delle forze trasmesse al terreno per i vari modelli studiati.

Il Capitolo 4 presenta in dettaglio il modello che lavora nel dominio delle frquenze e numeri d'onda. Anche per quanto riguarda questo modello sono state preparate tre strutture differenti. Come per il caso precende il primo, e il più semplice, rappresenta un semispazio infinito che schematizza il terreno. Attraverso questo modello è stato possibile indagare l'influenza dei vari parametri per poter comprendere al meglio il funzionamento del software e la dipendenza delle risposte dai parametri dati in ingresso. È anche stato possibile confrontare le risposte ottenute da questo modello con un modello analitico semplificato di propagazione delle onde nel terreno. Gli altri due modelli sono stati implementati per riprodurre delle condizioni sperimentali: il primo schematizza un terreno con 2 strati uno superiore più morbido e con delle velocità di propagazione delle onde più basse e un semispazio infinito più rigido con delle velocità di propagazione più elevate; il secondo rappresenta un tunnel circondato dal terreno rispetto al caso precedente di tunnel ad qui è possibile indagare la propagazione delle onde nel terreno circostate. Anche in questo Capitolo la seconta parte riguarda i risultati dell'integrazione nel domino delle frequenze e numeri d'onda. Inizialmente sono mostrati i risultati ottenuti al variare dei parametri per il semplice caso di semispazio infinito. Come risultati sono presentate le risposte delle strutture nel dominio delle frequenze e numeri d'onda, che approsimano bene le curve di dispersione della struttura. Queste mettono in relazione le frequenze con i numeri d'onda e mostrano sotto quali condizioni le onde cominciano a propagare nel terreno. Inoltre vengono mostrate anche le funzioni di trasferimento del terreno a diverse distanze dal punto di applicazione della forza. I parametri che sono stati cambiati per investigarne l'influenza sono: il range e la risoluzione dei numeri d'onda, la dimensione dei BE, il così detto traction vector (che rappresenta la pressione applicata all'elemento), e alla fine cambiamo i parametri del terreno per vedere se le simulazioni sono robuste.

Il Capitolo 5 riporta i risultati del modello ibrido per i vari casi presentati nei Capitoli precedenti. I risultati sono stati calcolati per diverse distanze dall'asse a cui e' stata applicata la forza per investigare come la risposta del terreno vari al variare della distanza. Qui si e' trovato, come prevedibile, che si ha una attenuazione delle vibrazioni del terreno all'aumentare della distanza. Si e' anche visto che le curve rispettano molto quello che succede nelle funzioni di trasferimento e lo spettro delle forze.

Alla fine sono riportate le conclusioni riguardo a questo lavoro di tesi e le appendici.

Introduction

Public concern regarding the impact on society of rail transport systems is growing, in particular with the trend towards higher speeds. Coupled with this is the introduction of increasingly stringent environmental standards and legislation. Noise and vibration are therefore important issues for railway companies and may increasingly affect their future operations and development.

The competitiveness of rail over other forms of transport is enhanced by its ability to operate from the centers of population and commerce. However, in order to achieve this, tunnels are often required in residential or commercial areas of large cities. This has led to the acceptance that vibration created by trains on the surface or in tunnels can be a potentially serious issue for mainline railways. The frequencies of vibration cover a range of about 2-200 Hz, [1]. Vibration in the frequency range 20-200 Hz [2] can cause an audible rumble (ground-borne noise) inside buildings as trains pass beneath. Additionally, lower-frequency perceptible vibration in the range 2-80 Hz can also be present [3], although it is generally less serious than ground-borne noise.

Railway administrations have also been concerned for some years about the levels of low-frequency perceptible vibration from trains operated on surface railways. This has been particularly highlighted by the use high axle load freight wagons. This vibration can cause not only disturbance, but also anxiety over structural damage to property. In some cases, where noise barriers have been erected, problems have occurred due to levels of ground-borne noise inside buildings exceeding the direct (airborne) noise from the trains.

This thesis focuses on the ground-borne noise induced by the passage of the train, so in the 20-200 Hz frequency range. This low frequency ground-borne vibration is mainly caused by the unevenness of the rail and wheel surfaces.

Historically there have always been two separate fields of study: the time domain field, that studies the vehicle dynamics and the wheel-rail interaction to investigate the forces exchanged between them; and the frequency-wavenumber domain, that is used to investigate the propagation of the waves in the ground.

The main aim of this thesis is to present a methodology that permits to couple these two methods: the use of the time domain model to simulate the passage of the train over a track to obtain the forces exchanged and the use of a frequency-wavenumber domain model to obtain the transfer functions of the ground. By combining the results obtained with these models it is possible to estimate the level of vibration, at a certain position, induced by the passage of a train.

In Chapter 1 a literature review is presented about the train-induced ground vibration, addressing the two main ways of studying the problem. In the first part the models are presented that operate in the time domain. These is focused on the vehicle dynamics and on the non linear behavior of the contact force. In the second part are presented the models that describe the ground and the wave propagation, these usually operate in the frequency/wavenumber domain because this way is easier to describe the wave propagation. The last part presents a novel approach called hybrid modelling that uses as inputs the results from the two previous approaches and is able to predict the level of vibration at a receiver.

Chapter 2 presents in detail the two models used in this thesis. The first model was developed from the Mechanical Engineering Department at the Politecnico di Milano, that simulates the pass-by of a train, modelled as a multi-body system, on a finite element structure in the time domain. This way it is able to consider the non linearities present in the model (i.e. the wheel/rail contact model). The second model was developed from the Institute of Sound and Vibration (ISVR) at the University of Southampton and simulates the ground forced response. It is a linear model that operates in the frequency wavenumber domain and it is able to describe the wave propagation in the ground. In the last part the hybrid methodology will be presented that is used in this thesis to couple the results from Politecnico's time domain model and from ISVR's frequency wavenumber domain model in order to obtain the response of the ground due to the pass-by of the train.

Chapter 3 describes in detail the inputs and the results of the time domain model. In the first part a detailed description is presented of the finite element models of the track, the tunnel and the joint irregularity. For the case of the rail also some analytical models have been used to better understand the physical problem. It has been found that for structural noise, like ground-borne noise, also a simplified model for the rail, like an Euler-Bernoulli beam, is sufficient to investigate this phenomenon. The tunnel and the joint irregularity are two examples used to test the hybrid method. In the second part of the Chapter the results of the time domain calculation are shown. Also here for the simple case of the rail an analytical model has been used to increase the knowledge of the problem. Also the results from the tunnel and the joint are presented and a comparison between the results of the rail with and without the tunnel has been made to investigate the influence of the tunnel on the forces exchanged between the train and the rail.

Chapter 4 describes in detail the inputs and the results of the wavenumber/frequency domain model. In the first part are presented the finite element, boundary element models used as input for the wavenumber/frequency domain model. Three different input models of the ground have been prepared: a simple halfspace, with different ground characteristics; a two layer ground and a tunnel structure deep bored in a homogeneous soil. In the second part the results of the numerical calculation in the frequency wavenumber domain are presented. The results of the simple halfspace have been used to investigate the sensitivity of the ground responses to the parameters chosen as input for the calculation procedure. Also a comparison with an analytical model is presented to understand if the numerical model returns reasonable results. In the end also the results for the tunnel are presented.

Chapter 5 presents the results for the hybrid method using the different models for the ground and for the rail presented in the previous Chapters.

Chapter 1

State of the art

This Chapter presents a literature review of the different ways to approach the problem of the ground-borne vibration due to a train pass-by. Because this problem is very complex many different ways to address the problem have been studied.

Since the pass-by of the train generates forces, due to the wheel/rail contact and to the vehicle and structure dynamics, that become the excitation mechanism for the ground-borne vibration. Section 1.1 presents a series of different methods to model the train/track interaction mechanism. These methods are usually conducted in the time domain because it is easier to model a train that moves in time and space.

The ground is a very complex system because it can have different layers and can be non-homogeneous and orthotropic. Section 1.2 illustrates different methods to model the ground that take into account different assumptions to simplify the problem. These methods are usually conducted in the frequency-wavenumber domain because it is easier to describe the wave propagation.

Because the two previous methods can be very heavy in terms of computational resources and time, Section 1.3 reports an innovative method, called the hybrid model. This couples the results from a time domain vehicle dynamics program with the frequency-wavenumber transfer functions of the ground in order to obtain the response at a certain receiver.

1.1 Vehicle dynamics and contact models

Usually railway vehicles used in passenger transportation have the same design principle, as shown in fig. 1.1. The car body rests on two bogies each containing two wheelsets. The springs and dampers connecting the wheelset bearings and the bogie frame are called the primary suspension. The secondary suspension connects the bogie frame and the car body.

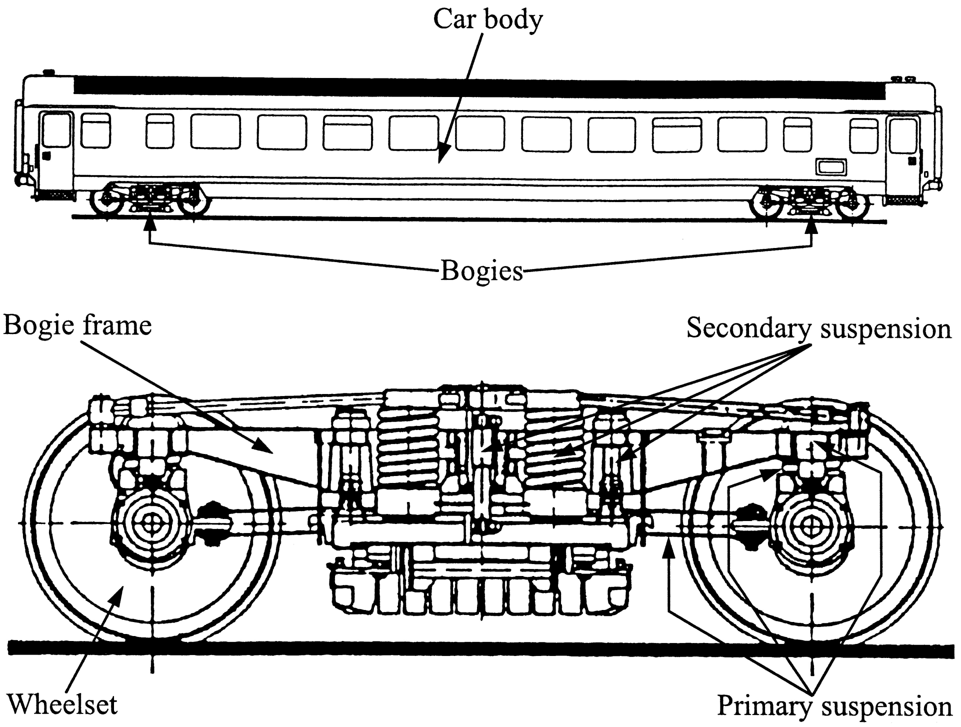

Figure 1.1: Car body and bogie components, reproduced from http://www.railforums.co.uk/

The wheelsets are quite heavy and the the longitudinal and lateral stiffness of the primary suspension are always high. This is necessary for a stable running of the wheelsets. In comparison, the secondary suspension is much softer. Since additionally the mass of the car body is high (about 30 tons), car body and bogies are decoupled by a frequency ratio of about 1:10 [4]. This decoupling gives the possibility to see the car body as mass on top of the secondary suspensions. Since ground-borne noise is generated at frequencies higher than the vehicle dynamics this will not be taken in consideration in this work.

An example of vehicle/track interaction simulation is described in [5], it considers the vehicle dynamics using a multi-body model of the trainset. The entire trainset is subdivided into elementary units. The carbody is modeled as a single rigid body, the bogie assembly is modelled as a rigid bogie frame connected by primary suspensions to two (or possibly three) flexible wheelsets. The elementary units are connected to each other by springs and dampers (linear and non-linear) reproducing the secondary suspensions and other elastic connections such as links between carbodies, elastic motor suspension etc. This software was adopted along the research carried out within this thesis.

Finite element model technique is used for the track. Euler–Bernoulli beam elements are used to model the different rails, while the rest can be modelled by lumped parameters mass-spring-dumper.

Various model of wheel/rail contact can be found in the literature.

Kassa in [6] uses Hertz contact theory [7] to resolve the normal wheel–rail contact problem. The magnitude and orientation of the normal contact force depends on the curvature difference of the two contacting surfaces and the contact angle at the contact point. To find the deformation at the contact point, the contact geometry and the local penetration of the wheel and the rail surfaces are used. Then, the normal force can be calculated on the basis of a linear or a non-linear Hertzian contact stiffness.

Shabana in [8] presents a formulation for the wheel/rail contact problem based on the elastic force approach. The method presented allows for multiple points of contact between the wheel and the rail by using an optimized search for all possible contact points. The normal contact forces are calculated and used with non-linear expressions for the creepages to determine the creep forces.

The Politecnico di Milano software is based on a non-linear multi-Hertzian approach [9]. This procedure includes the effect of the spatial variation of rail profiles occurring during turnout negotiation, to account for the ‘sink and lift’ effect produced on the wheel during the passage over, for example, a crossing nose, and to consider the case of multiple contact between one wheel and two (or more) separate rails, in this thesis this option won’t be adopted being the simulation performed along a straight track.

1.2 Waves propagation in ground models

Many models for the waves propagation in ground have been developed over the past years. These can be divided into analytical methods, numerical methods such as finite element or boundary element method and empirical methods which are based on measurements. Analytical models are usually more efficient than numerical models and less expensive than empirical models but usually they are limited to simple geometry and homogeneous material.

Analytical models

Several analytical models have been developed using either two-dimensional or three-dimensional analysis. The advantage of a two-dimensional model is the shorter computational time. However, it is not able to treat the effect of waves propagating in the third direction. Therefore a three-dimensional model is required for the wave propagation. Three-dimensional models, however, require a larger computing resources [10].

An analytical three-dimensional model was developed by Forrest and Hunt [11] for an underground railway tunnel of circular cross-section. The tunnel was represented as an infinitely long, thin cylindrical shell surrounded by soil of infinite radial extent. A track model was then added to the model in [12] to assess the effectiveness of floating-slab track.

In [13] the use of several discrete wavenumber methods to model ground vibration from underground trains has been investigated. These methods were divided into three categories: the discrete wavenumber fictitious forces method, the discrete wavenumber finite element method and the discrete wavenumber boundary element method. These methods are based on the moving Green's functions for a layered half-space.

Numerical models

An analytical model such as those mentioned above is limited in scope to simple geometries and homogeneous materials. For analysis of more complex geometries or of heterogeneous grounds numerical models using finite elements (FE) or boundary elements (BE) are required, [14]. The boundary element method is a numerical method to solve partial differential equation. The BEM distinguish itself from the FEM because is a boundary method, meaning that the numerical discretization is conducted at reduced spatial dimension. For example, for problems in three spatial dimensions, the discretization is performed on the bounding surface only; and in two spatial dimensions, the discretization is on the boundary contour only. This reduced dimension leads to smaller linear systems, less computer memory requirements, and more efficient computation.

A two-dimensional model has been developed by Chua in [15] where is investigated the ground-bornee vibration in buildings induced by underground railway traffic. This model, however, cannot account for wave propagation in the direction of the track.

A three-dimensional dynamic tunnel–soil interaction problem is presented in [16]. The problem is solved using a finite element formulation for the tunnel and a boundary element method for the soil. The periodicity of the tunnel and the soil in the longitudinal direction is exploited using the Floquet transform [17], limiting the discretization effort to a single bounded reference cell. The proposed model is based on the following hypotheses: the tunnel is assumed to be periodic in the direction of its longitudinal axis with a period L, the tunnel is embedded in a horizontally layered soil, and all displacements and strains remain sufficiently small so that linear models can be used.

In many situations, the ground and built structures can be assumed to be homogeneous in the track direction. For such engineering configurations, an approach has been suggested [18] in which the problem is transformed into a sequence of 2D models depending on the wavenumber in the track direction. For each wavenumber, the finite cross-section of the built structure is modeled using the finite element method, and the wave propagation in the surrounding soil is modeled using the boundary element method. The FE and BE domains are coupled and the global FE/BE equations are then solved, giving the component to the response at this wavenumber. The actual response is then constructed from these components using an inverse Fourier transform. This methods are known as two-and-half dimensional (2.5D) methods.

An example of this method has been presented in [19], for predicting ground vibration from trains running either on the ground surface or in tunnels. This model requires the ground and built structures to be homogeneous in the track direction but allows an arbitrarily shaped cross-section.

With this method the computing resources required are reasonable for practical analyses and predictions of real cases, but still it is a critical resource that has to be taken into account.

The program used in this thesis, WANDS (Wave Number Domain Software), to predict the wave propagation in the ground is a 2.5D model. The theory behind this model is presented in [20] and summarized in Appendix B to explain a simple example.

Empirical models

Nelson and Saurenman [21] presented an empirical procedure to predict ground-borne noise and vibration caused by rail transportation systems on experimental results at residential and commercial building near at-grade and subway tracks. Two particular features of the method are the use of impact-testing procedure to characterize vibration propagation and the use of 1/3 octave band force to represent specific vehicle and track systems. The main steps of the prediction procedure are: selection of a trackbed force density to represent the trains, determination of a line source response from measured mobilities, calculation of building response and calculation of noise.

There are many other example of empirical approaches like Greer's method for the calculation of re-radiated noise [22]. Hood in [23] used Greer's method to develop procedures for assessment criteria and calculation for ground-borne noise and vibration from trains in tunnels.

1.3 Hybrid models

Since the whole 3D models for the vehicle dynamics and waves propagation in the ground has a computational cost too high to be used for complex problems and the frequency-wavenumber models are not able to take into account the vehicle dynamics, a novel methodology was recently developed which is normally addressed as hybrid model.

To the author's knowledge the only publication that deals this topic is [24]. In this thesis the author uses a model that operates in the time and spatial domain and was originally developed to study wheel/rail interaction that consists of a series of wheels running along a track supported by discrete sleepers on ballast and ground springs. The model is used to determine the force time histories of interest. An axisymmetric layered ground analytical model is then applied to represent an elastic layered ground. This is used to obtain the transfer mobilities from each sleeper position to a receiver position. These are combined with force spectra obtained from the whee/rail interaction model to give the response at the receiver location.

The main idea of this thesis is to use the results from a frequency-wavenumber model in order to obtain the ground transfer functions and wave propagation properties. Separately, using a program that simulate the vehicle dynamics to obtain the forces due to the pass-by of the train to give as an input in the hybrid model, for example the wheel/rail contact forces or the forces transfered to the ground. A third program is to be used to post process and couple the results from the frequency-wavenumber domain with the results form the time domain.

Fig. 1.2 shows a simplified block diagram to explain the main idea of the hybrid model.

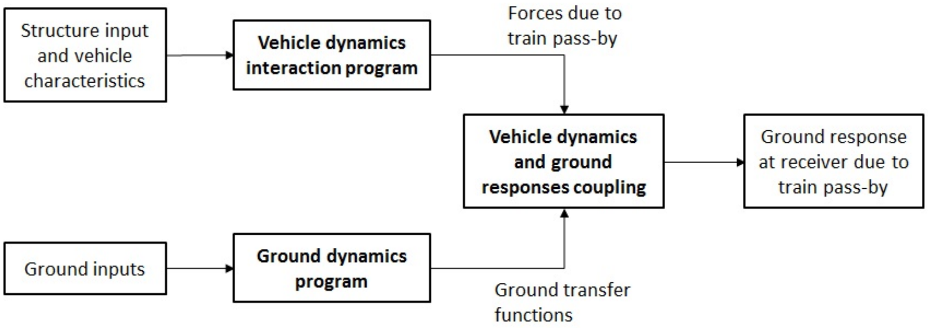

Figure 1.2: Block diagram for the hybrid model

For this work two existing softwares have been used: one, developed at Politecnico di Milano, that simulates the vehicle dynamics; and one, developed at University of Southampton, that simulates the propagation of the waves in the ground. The software for the coupling has been implemented based on the theory found in [24].

Chapter 2

Hybrid modelling of train induced ground vibration

This Chapter describes a methodology for coupling the pass by of a train obtained with a time domain track/vehicle dynamics model with the transfer mobilities of the ground obtained with a frequency-wavenumber domain ground model. This methodology has been described in, [24].

For this work of thesis different softwares, from the ones found in [24], has been used but the main idea of the coupling methodology remains the same: with the time domain track/train model the forces underneath the sleepers are obtained, with the frequency-wavenumber ground model the transfer mobilities from the sleepers to a receiver are obtained and the coupling is done with the auto and cross spectra of the forces in order to reproduce the time dependance due to the movement of the train.

The following Sections describe the different softwares and the methodology used to get the ground response. Section 2.1 describes the track/vehicle dynamics model developed from the Mechanical Engineering department at Politecnico di Milano University which has been use to obtain the forces due to the pass-by of the train. Section 2.2 presents the semi-analytical frequency-wavenumber domain ground model developed at the Institute of Sound and Vibration at University of Southampton that has been used to extract the ground transfer function between the sleepers and the receiver. Section 2.3 describes the coupling methodology that makes possible the interaction between a time domain simulation and a frequency-wavenumber one.

2.1 Polimi train/track interaction model

The model of train–track interaction is defined in the time domain and this allows to take into account the non-linear effects associated with the wheel–rail contact, [9]. The model is based on a three-dimensional finite element representation of the track and everything else that needs to be modelled with the FE method, as presented also in Section 3.1, and on a mixed rigid/flexible multi-body description of the trainset. The equations of motion for these two subsystems are written separately, with wheel–rail contact forces acting as the coupling terms between the two sets of equations and are integrated using a time-stepping algorithm based on the Newmark method.

2.1.1 Finite element model of the track and tunnel

As shown in Sections 3.1.1, 3.1.3 and 3.1.4 three different finite element models have been prepared: one that represents the track alone attached through spring elements, that represent the stiffness of the sleepers, to a rigid ground; one that represents the track coupled with the tunnel and the tunnel is attached to a rigid ground through spring elements that represent the stiffness of the equivalent surrounding ground; the last one is a particular case of the tunnel model where the rail presents a joint irregularity that gives higher levels of the forces. They are all over 40 meters long in order to minimize the effects of wave reflection at the boundaries.

Using a matrix-based notation, the equations of motion for the track, or track and tunnel, finite element model becomes

$$\boldsymbol{M}_t\ddot{x}_t + \boldsymbol{C}_t\dot{x}_t + \boldsymbol{K}_t x_t = F_{ct}(x_t, \dot{x}_t, x_v, \dot{x}_v, V, t) \tag{2.1}$$

where $\boldsymbol{M}_t$, $\boldsymbol{C}_t$ and $\boldsymbol{K}_t$ are the mass, damping and stiffness matrices of the finite element model respectively, x_t is the vector of the nodal coordinates (displacements and rotations), x_v is the vector of trainset coordinates and F_{ct} is a vector of generalized nodal forces representing the effect of wheel–rail contact forces, as shown in [25]. It is observed in equation (2.1) that vector F_{ct} is a function of both the track state x_t, $\dot{x}_t$ and the trainset state x_v, $\dot{x}_v$, and hence acts as a coupling term between the set of equations governing the vibration of the track and those describing the dynamics of the trainset

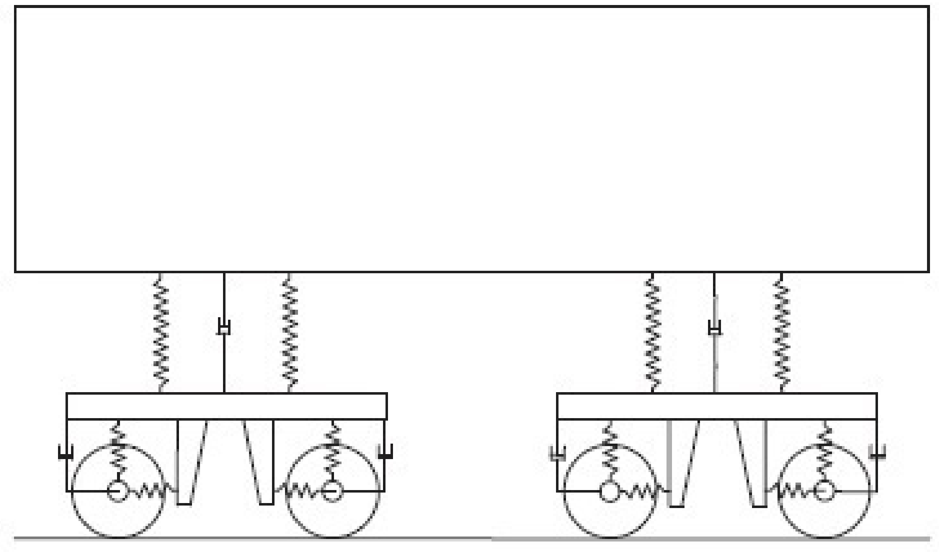

Figure 2.1: Multy-body simplification of the train from [25]

traveling along the track, see below. Additionally, vector F_{ct} depends on the trainset forward velocity V and explicitly on time t.

2.1.2 Multy-body model of the trainset

A multi-body model was developed by the Politecnico di Milano to describe the motion of rail vehicles travelling along a track.

The entire trainset is subdivided into elementary units of the following types:

- carbody, modelled as a single rigid body;
- bogie assembly, modelled as a rigid bogie frame connected by primary suspensions to two flexible wheelsets (or possibly three);
- other bodies attached either to a carbody or to a bogie frame (e.g. motors, converters, etc.), modelled as rigid.

The elementary units are connected to each other by linear and nonlinear springs and dampers reproducing the secondary suspensions and other elastic connections such as links between carbodies, elastic motor suspension etc, as shown in fig. 2.1. By combining the above listed elementary units, any specific trainset architecture may be derived, e.g. rail vehicles formed by two bogies and one carbody, or more complicated configurations like articulated trainsets.

Each rigid body is assigned with five degrees of freedom, the forward speed of body center of mass being set to a constant value V, whereas for each flexible wheelset, the movement with respect to the moving reference is defined as the linear combination of the unconstrained wheelset eigenmodes. In addition to the five rigid motion modes, bending and torsion modes and some modes corresponding to local deformation of the wheels are typically included in the analysis to reproduce wheelset vibration in the 0–500 Hz frequency range.

In order to deal with the possible negotiation of small radius curves along the branch line (which may be the case for urban turnouts, especially in tramway lines), the motion of each elementary unit is described with respect to a moving reference travelling with constant speed along the track centre-line and keeping the Z axis tangent to the track centreline and the X axis orthogonal to the rail level. By assuming for each module in the trainset small displacements relative to the corresponding moving reference, the trainset equations of motion are linearised with respect to kinematic nonlinear effects only, and they become

$$\begin{aligned} \boldsymbol{M}_v \ddot{x}_v + \boldsymbol{C}_v \dot{x}_v + \boldsymbol{K}_v x_v = F_e(V,t) + F_i(V,t) + \\ + F_{nl}(x_v, \dot{x}_v) + F_{cv}(x_t, \dot{x}_t, x_v, \dot{x}_v, V, t) \end{aligned} \tag{2.2}$$

where $\boldsymbol{M}_v$, $\boldsymbol{C}_v$ and $\boldsymbol{K}_v$ are respectively the mass, damping and stiffness matrices of the trainset, x_v the vector collecting the trainset coordinates, F_e the vector of generalised forces produced in the secondary suspensions and carbody links by the different motion of the moving references associated with the modules connected by the suspension, F_i the vector of inertial forces due to the non-inertial motion of the moving references, F_{nl} the vector of nonlinear forces due to nonlinear elements in the suspensions, e.g. bumpstops, and finally F_{cv} is the vector of generalised forces due to wheel/rail contact, which are nonlinear functions of the track and trainset coordinates and of their time derivatives, as shown in [5].

Because the Politecnico di Milano vehicle dynamics software is very versatile any kind of train can be reproduced. The train used to conduct the time domain simulations is the one used in [26] and

The model used to simulate this train is a three cars, in order to reduce the computational time, consisting of two motor cars and one trailer car with the same specification as the one used for the CONVURT project [26] and also reported in Appendix A.

2.1.3 Wheel/rail contact model

The contact model is based on a nonlinear multi-Hertzian approach studied at Politecnico di Milano and presented in [27]. This means that the coefficient C_H, which is the coefficient of the Hertzian formulae, relates the normal contact force to the power 3/2 of the elastic compenetration of the wheel and rail. This coefficient is computed as a function of the local curvatures of wheel and rail profiles in the contact point.

The computation of wheel–rail contact forces is performed first by a geometric analysis of the contacting bodies and the results are stored in the form of contact tables that are then used to compute the wheel–rail contact forces during the simulation of the vehicle motion. This procedure allows a CPU-time efficient computation of wheel–rail forces and has proven to be reliable and accurate when applied to the simulation of 'standard' wheel–rail contact conditions like the ones of interest for this thesis, [9].

During the numerical integration of equations (2.1) and (2.2), wheel–rail contact forces are computed. Three main steps are at the basis of this integration: the displacements and velocities of the rails and of the wheel are computed in all the potential contact points; the kinematic parameters are then used to detect the active contact points (e.g. those points where contact actually takes place), for these points, contact parameters are obtained by contact table lookup and normal and tangential contact forces are derived; at last, wheel–rail contact forces are transformed into the nodal forces F_{ct} acting on the track and the generalised forces F_{cv} acting along the trainset coordinates.

In order to compute wheel/rail contact forces, the displacements and velocities of the potential contact points on the wheel and rail surfaces need to be computed.

Lets start considering the rail displacements and velocities. The local position ξ_j of the wheel along the beam element is computed and, using the beam element shape functions $f_{j,k}(\xi_j)$, the displacements and rotations of the rail section in contact with the wheel are derived. The contact point displacements are computed by multiplying the vector representing rail section displacements and rotations by a matrix relating the contact point displacement with the rigid motion of the rail section. The effect of rail irregularities is accounted for by adding an additional displacement vector $x^r_{irr}(s_j)$, a function of the longitudinal position of the wheel s_j. The irregularity vector is defined only in the X_t, and Y_t directions and is obtained from a precomputed space distribution of irregularity. The rail irregularity used for the time domain simulation is discussed in detail in Section 3.2.1. The same thing can be done to calculate the wheel displacements and velocities. As well as for the rail also for the wheel can be considered a superficial irregularity $x^w_{irr}(\theta_j)$ accounting the wheel roughness also shown in detail in Section 3.2.1.

Based on the calculation of the relative wheel/rail displacements and velocities in all potential contact points, whee/rail contact parameters are computed by interpolation of the multisection contact table, using as inputs the lateral relative wheel/rail displacement and the longitudinal position of the j_{th} wheelset. The normal component of the contact force in the k_{th} potential contact is then computed as a function of the elastic wheel/rail penetration and of the penetration speed, both function of the relative wheel/rail displacement, considering a nonlinear Hertzian contact element with an additional penetration dependent damping term, introduced to improve the stability of the numerical procedure. The longitudinal and transverse components of the contact force, are computed as a function of the normal force components of the longitudinal and transversal creepages and of the spin creepage taking place in the contact patch. Since for this model only a strait rail is considered the effects of the transverse contact force should be negligible.

By the use of the principle of virtual work the vectors F_{cv}, containing the generalised forces along the trainset coordinates, and the vector F_{ct}, containing the generalised nodal forces of the track finite element representation, can be obtained as shown in [5]. The results for the contact forces obtained by the time domain simulation are shown in Section 3.2.

2.1.4 Output

From the Polimi train/track model a whole sort of different output can be obtained. Firstly the time history of the contact forces between the wheel and the rail can be extracted, than also the forces exchanged from any spring element, for example the ones underneath the sleepers in the finite element model of the track used in this thesis. Other types of output are related to the nodes of the FE structure and to the crucial points of the vehicle.

From the FE model all the time histories of displacement, velocity and acceleration for every node of the structure can be extracted, usually to reduce the size of the output and so also the computational time the nodes of interest can be specified before running the analysis.

From the vehicle the time histories of the position, velocity and acceleration of the journal box can be extracted. Those can be used to verify if the time domain simulation has successfully run.

2.2 ISVR ground model

Vibration can propagate in infinite solid elastic materials by two fundamental mechanisms: shear and dilatation. Because of these two mechanisms also two fundamental wave speeds are related to the material properties of the soil. The ground can be represented as an elastodynamic material, described by Navier's equations, [28]

$$\begin{aligned}(\lambda+\mu)\frac{\partial\Delta}{\partial x}+\mu\nabla^2 u&=\rho\frac{\partial^2 u}{\partial t^2}\\(\lambda+\mu)\frac{\partial\Delta}{\partial y}+\mu\nabla^2 v&=\rho\frac{\partial^2 v}{\partial t^2}\\(\lambda+\mu)\frac{\partial\Delta}{\partial z}+\mu\nabla^2 w&=\rho\frac{\partial^2 w}{\partial t^2}\end{aligned}\tag{2.3}$$

where u, v, w are the x, y, z components of displacement u, $\Delta=\frac{\partial u}{\partial x}+\frac{\partial v}{\partial y}+\frac{\partial w}{\partial z}$ is the dilatation and λ and μ are Lamé's constants for the material, λ is the first Lamé constant,

$$\lambda=\frac{\nu E}{(1+\nu)(1-2\nu)}\tag{2.4}$$

and μ is the second Lamé constant, or shear modulus

$$\mu=\frac{E}{2(1+\nu)}\tag{2.5}$$

where E is Young's modulus, and ν is Poisson's ratio.

The first fundamental wave speed is the longitudinal wave speed (the P-wave speed) and the second, the transverse wave speed (the S-wave speed). In a longitudinal wave the particle displacement is parallel to the direction of wave propagation. Simple examples of this kind of waves are the waves propagating along the axis of a beam or the sound waves propagating in air, [29]. In a transverse wave the particle displacement is perpendicular to the direction of wave propagation. Simple examples of this kind of waves are the transversal waves of a string, [29]. The ground longitudinal wave speed is given by

$$c_1 = \sqrt{\frac{\lambda + 2\mu}{\rho}} \tag{2.6}$$

while the transverse wave speed (the S-wave speed), is given by

$$c_2 = \sqrt{\frac{\mu}{\rho}} \tag{2.7}$$

The longitudinal wave speed is always greater than the transverse wave speed. There is a fundamental relation between the wave speed (or speed of sound) c, and the angular frequency ω

$$c = \frac{\omega}{k} \tag{2.8}$$

where k is the wavenumber and is expressed in $[rad/m]$.

In order to model wave propagation in the ground different approaches can be used. The model developed at the University of Southampton, called WANDS (WAve Number Domain Software), is a 2.5D model. The idea of the 2.5D model is to describe a two dimensional section using finite-element (FE) and boundary-element (BE) methods to model the geometry and properties of the ground, while in the third direction the models are formulated in terms of wavenumber so the structure is considered infinitely long and homogeneous.

- Model of the section of the ground using FE and BE methods
- Forced response in the frequency wavenumber domain computed per every frequency and every wavenumber
- Reconstruction of the third dimension from the wavenumber domain
- Forced response in the space frequency domain

Compared with a conventional, three-dimensional finite or boundary-element model, this is computationally faster and requires far less memory, even though calculations must be performed for a series of discrete wavenumbers.

WANDS extracts also the total system matrices from where, as shown in Appendix B, if the geometry is not complex, the dispersion curves can be obtained. These represent the relation between the angular frequency ω and the wavenumbers k. The frequencies obtained with $k = 0$ are called cut-on frequencies and they represent the frequency at which that specific wave starts to propagate. Before the cut-on frequency the wave is a decaying wave, this means that it is present only in the nearfield but it does not propagate. For more complex geometries a numerical integration is needed. WANDS solves the numerical problem for every frequency and every wavenumber in a specific range given as input. From the numerical integration in the frequency-wavenumber domain the dispersion curves of the structure can be obtained. From this results, by applying the inverse Fourier transform the frequency response of the structure can be obtained.

Each type of FE or BE domain is termed a "sub-model". In addition the coupling conditions implemented to join the different FE or BE models are also referred to as sub-models or coupling sub-models. There is a large number of sub-models implemented in WANDS: Plate FE models, Solid FE models, Fluid FE models, Fluid BE models, Solid BE models and the coupling between them. Also Beam elements can be coupled with Plate or Solid FE models. Since the coupling between some sub-models are not yet working properly, in the study carried on in this thesis only the Solid FE models, also coupled with Beam elements, and the Solid BE models have been used.

As shown also in Appendix D the relation that stays as starting point for all models is the Hamilton's principle, [20]

$$\delta(U - T) - \delta W = 0 \tag{2.9}$$

where δ should be interpreted as "the first variation of", U is the potential energy in the system, which for the systems here is the same as the strain energy, T is the kinetic energy and W is the virtual work on the system which includes both external forces as well as internal forces that give rise to losses in the system. In addition to equation (2.9) also Dirichlet boundary conditions must be fulfilled. For structures these boundary conditions impose constraints on the displacements. A second set of boundary conditions, Neuman boundary conditions, are implicitly included in equation (2.9). For structures such boundary conditions prescribes the relationship between displacements and forces of the boundary.

By using expressions for U, T and W and substituting them into equation (2.9), the weak form of the equation of motion can be obtained.

2.2.1 Finite element model

Starting from the equations for the kinetic energy, the potential energy and the virtual work the differential equation of motion of the finite element can be derived (see also [30]):

$$[M]\ddot{q}(x,t) + [K_0]q(x,t) + [K_1]\frac{\partial}{\partial x}q(x,t) - [K_2]\frac{\partial^2}{\partial x^2}q(x,t) = F(x,t) \quad (2.10)$$

where $[M]$, $[K_0]$ and $[K_2]$ are symmetric matrices, $[M]$ and $[K_2]$ are positive definite and $[K_0]$ is non-negative. It can also be shown that $[K_1]$ is an anti-symmetric matrix. From this equation applying the corresponding matrices of the assembled FEM and thus the global differential equation of motion can be assembled.

$$\left[\boldsymbol{K}_0 + i\beta\boldsymbol{K}_1 + \beta^2\boldsymbol{K}_2 - \omega^2\boldsymbol{M}\right]\tilde{u}(\beta) = \tilde{\boldsymbol{F}}(\beta) \quad (2.11)$$

The transformed displacement vector $\tilde{u}(\beta)$ can be evaluated from equation (2.11) for each wavenumber β and then the actual displacements may be obtained using an inverse Fourier transform. For simple cases, as shown in Appendix B, from the system matrices, with a post processing, also the dispersion curves of the model can be obtained.

In WANDS, for the solid finite element models, many topologies are implemented: quadrilateral linear with 4 nodes per element, triangular linear with 3 nodes per element, quadrilateral cubic with 12 nodes per element, triangular cubic with 10 nodes per element, quadrilateral quadratic with 8 nodes per element and triangular quadratic with 6 nodes per element. In order to define a finite element its type must be specified, the material which the element is made and the coordinates of the corresponding nodes. The material can be either isotropic or orthotropic.

2.2.2 Boundary element model

The boundary element method is a numerical method to solve partial differential equations. In some cases a structure can be described simply by what happens at the boundary and that is the main idea of the boundary element method. The boundary of the structure is discretized by a finite number of elements with known shape functions, like for the FE method, and the integration is reduced to just the boundary of the structure due to Gauss' integral theorem.

$$\int_{\Omega} div\, v(x)\, dx = \int_{\partial\Omega} v \cdot n\, ds_x \tag{2.12}$$

Where Ω is the total domain and $\partial\Omega$ is the boundary. This is much lighter than describing with the FE method a whole structure so for big objects, for example a halfspace, it is very convenient because the number of nodes is much smaller. The problem occurs when it is of interest to know what happens inside the structure because the boundary element method is only capable to describe what happens on the boundaries.

The x cross-section of the infinitely long elastic body is denoted by A and the boundary of A in its own plane is denoted by Γ. For this elastic body, two elasto-dynamic states are defined. The firs one is described by displacements $u_k(x, y, z, t)$, body forces $\rho b_k(x, y, z, t)$ and boundary tractions $p_k(x, y, z, t)$, where $k = 1, 2, 3$ corresponds to the x, y and z directions. The second state is described by $u_k^*(x, y, z, t)$, $\rho b_k^*(x, y, z, t)$ and $p_k^*(x, y, z, t)$. As shown in [30] the reciprocal relation between the two states in the wavenumber domain can be derived

$$\begin{aligned}&\int_{\Gamma} \tilde{p}_k(\beta, y, z)\tilde{u}_k^*(-\beta, y, z)\, d\Gamma + \int_{A} \rho\tilde{b}_k(\beta, y, z)\tilde{u}_k^*(-\beta, y, z)\, dA = \\ &= \int_{\Gamma} \tilde{p}_k^*(-\beta, y, z)\tilde{u}_k(\beta, y, z)\, d\Gamma + \int_{A} \rho\tilde{b}_k^*(-\beta, y, z)\tilde{u}_k(\beta, y, z)\, dA\end{aligned} \tag{2.13}$$

When β is set to zero, this recovers the reciprocal theorem in elasto-dynamics for the plane-strain problem. The assembled equation of the boundary element sub-model becomes, [30]

$$\boldsymbol{H}\tilde{u}(\beta) = \boldsymbol{G}\tilde{p}(\beta) + \tilde{\boldsymbol{B}}(\beta) \tag{2.14}$$

where $\boldsymbol{H}$ and $\boldsymbol{G}$ are squared matrices and $\tilde{\boldsymbol{B}}$ are the forces that acts on the body.

In WANDS, for the solid boundary element models, there is only one type of element and it is a quadratic element with 3 nodes per element. In order to define the boundary element the material and the nodes coordinate must be defined. There are some conventions to take into account while building the input file. If the node numbering of the boundary elements is anti-clockwise an internal problem is defined otherwise, for a clockwise numbering, an external problem is specified. To define a semi-infinite problem some special elements are defined, called edge elements, that neglect the reflection of the waves from the borders of the model. In order to achieve this result the perfectly matched layer (PML) have been used, [31]. This is an artificial absorbing layer that neglect the reflection of the incident waves.

For those nodes that are not coupled with any other element boundary conditions have to be defined in order to get a response, they are defined by

$$c_a u + c_b t = cc \tag{2.15}$$

where u is the displacement in the x, y and z directions and t is the traction vector, which is a force per unit area acting on the boundary, in the same directions, while c_a, c_b and cc are complex scalars defining the boundary condition. Hence, for example, if a rigid boundary is considered the condition $u = 0$ is needed, otherwise if a free surface is needed the condition $t = 0$ is required.

2.2.3 Coupling between sub-domains

It can happen, especially while considering complex cases, that different sub-domains have to be modelled. A domain such as a layered ground, which may include built structures like a tunnel and a track, as will be developed in this thesis, has to be divided in different sub-domains. Each of the BE sub-domains is homogeneous. For each sub-domain, a BE equation or a FE equation can be constructed, and coupling of these equations gives the global equation for the whole system.

A single BE equation can be written for all the BE sub-domains. Rearranging equation (2.14) pre-multiplying by $\boldsymbol{G}^{-1}$ it becomes

$$\boldsymbol{R}_{be}\tilde{u}(\beta) = \tilde{p}(\beta) + \tilde{s}_{be}(\beta) \tag{2.16}$$

If, in addition to the BE sub-domains, a FE sub-domain is present, then the FE equation must be coupled with equation (2.16) to give the global equation for the whole model. The displacements, tractions and nodal forces of the nodes at the FE–BE interface are denoted by $\tilde{u}_I(\beta)$, $\tilde{p}_I(\beta)$ and $\tilde{F}_I(\beta)$. Those to the remaining nodes are denoted by $\tilde{u}_{beR}(\beta)$ and $\tilde{p}_{beR}(\beta)$ for the BE sub-domains, and $\tilde{u}_{feR}(\beta)$ and $\tilde{F}_{feR}(\beta)$ for the FE sub-domain. Thus equation (2.16) can be split into

$$\begin{bmatrix} \boldsymbol{R}_{beRR} & \boldsymbol{R}_{beRI} \\ \boldsymbol{R}_{beIR} & \boldsymbol{R}_{beII} \end{bmatrix} \begin{Bmatrix} \tilde{u}_{beR}(\beta) \\ \tilde{u}_I(\beta) \end{Bmatrix} = \begin{Bmatrix} \tilde{p}_{beR}(\beta) \\ \tilde{p}_I(\beta) \end{Bmatrix} + \begin{Bmatrix} \tilde{s}_{beR}(\beta) \\ \tilde{s}_{beI}(\beta) \end{Bmatrix} \tag{2.17}$$

and the FE equation (2.11) can be split into

$$\begin{bmatrix} \boldsymbol{K}_{feII} & \boldsymbol{K}_{feIR} \\ \boldsymbol{K}_{feRI} & \boldsymbol{K}_{feRR} \end{bmatrix} \begin{Bmatrix} \tilde{u}_I(\beta) \\ \tilde{u}_{feR}(\beta) \end{Bmatrix} = \begin{Bmatrix} \tilde{\boldsymbol{F}}_I(beta) \\ \tilde{\boldsymbol{F}}_{feR}(\beta) \end{Bmatrix} \tag{2.18}$$

A transformation matrix, $\boldsymbol{T}$, may be constructed to convert the tractions $\tilde{p}_I(\beta)$ of the boundary element formulation at the FE–BE interface into the equivalent nodal forces to enable assembly with the FE matrices, that is,

$$\tilde{\boldsymbol{F}}_I(\beta) = -\boldsymbol{T}\tilde{p}_I(\beta) \tag{2.19}$$

The dimension of the matrix $\boldsymbol{T}$ depends on the number of nodes at the FE–BE domain interface. Substituting equation (2.19) into equation (2.17) gives

$$\begin{bmatrix} \boldsymbol{R}_{beRR} & \boldsymbol{R}_{beRI} \\ \boldsymbol{T}\boldsymbol{R}_{beRI} & \boldsymbol{T}\boldsymbol{R}_{beII} \end{bmatrix} \begin{Bmatrix} \tilde{u}_{beR}(\beta) \\ \tilde{u}_I(\beta) \end{Bmatrix} = \begin{Bmatrix} \tilde{p}_{beR}(\beta) \\ -\tilde{\boldsymbol{F}}_I(\beta) \end{Bmatrix} + \begin{Bmatrix} \tilde{s}_{beR}(\beta) \\ \boldsymbol{T}\tilde{s}_{beI}(\beta) \end{Bmatrix} \tag{2.20}$$

The tractions on the FE–BE interface have thus been converted into equivalent nodal forces. This means the possible discontinuity of tractions on the FE–BE interface does not have to be considered. Assembling equation (2.18) with equation (2.20) yield

$$\begin{bmatrix} \boldsymbol{R}_{beRR} & \boldsymbol{R}_{beRI} & \boldsymbol{0} \\ \boldsymbol{T}\boldsymbol{R}_{beIR} & \boldsymbol{T}\boldsymbol{R}_{beII} + \boldsymbol{K}_{feII} & \boldsymbol{K}_{feIR} \\ \boldsymbol{0} & \boldsymbol{K}_{feRI} & \boldsymbol{K}_{feRR} \end{bmatrix} \begin{Bmatrix} \tilde{u}_{beR}(\beta) \\ \tilde{u}_I(\beta) \\ \tilde{u}_{feR}(\beta) \end{Bmatrix} = \begin{Bmatrix} \tilde{p}_{beRR}(\beta) + \tilde{s}_{beR}(\beta) \\ \boldsymbol{T}\tilde{s}_{beI}(\beta) \\ \tilde{\boldsymbol{F}}_{feR}(\beta) \end{Bmatrix} \tag{2.21}$$

This is the global equation for the whole system.

2.2.4 Output

WANDS gives as outputs the whole system matrices, that can be use in case of error to verify if the model is correct, the single sub-model matrices that, as shown in Appendix B, can be also used to generate the dispersion curves of the model and a pair of files, representing modulus and phase of the displacements, for each direction which contain the results of the numerical integration of the ground.

Due to the construction of WANDS the results are obtained in the spatial domain so that they represent the transfer functions of the ground. These transfer functions represent the displacements to a certain node and the forced node. Those transfer functions have been calculated also in the third dimension. If a Fourier transform, with respect to the space, is applied to these results then the dispersion curves of the node considered are found. From these it can be calculated the speed of the waves propagating in the material and the relation between the frequency and the wavenumber in the propagation.

2.3 Time domain frequency-wavenumber domain coupling

The hybrid model, as said before, combines the results from the time domain track/vehicle interaction model with the transfer mobilities of the ground obtained with WANDS. The forces can be obtained at different positions depending on what the two different models can and can not reproduce. The forces from the time domain model can be extracted at different levels:

- Contact force between the wheel and the rail
- Force transfered from the sleepers to the ground (or tunnel invert)
- In case of tunnel the forces transmitted from the tunnel walls to the surrounding ground

The forces can be applied at different levels in the wave frequency domain model:

- On the rail top, if the rail is modelled
- On the ground surface (or tunnel invert)

- In case of the tunnel on the ground surrounding the tunnel

The choice depends on the possibility to model the different part of the structure. During the work of this thesis it has been chosen to use the forces transmitted to the ground from the rail.

In order to explain and easily compare the methodology of this approach the case studied in [24] has been replicated. This considers a non ballasted track laid on the surface of a two layered ground.

In [24] the ground model used is able to represent the track along its length, while with WANDS this is not possible so in order to get the transfer mobilities needed a post processing of its results must be performed.

For a system where the transfer function is known the response is simply

$$A(s) = H(s)B(s) \tag{2.22}$$

where $H(s)$ is the transfer function and $B(s)$ are the inputs. In this case of study the transfer function is the mobility of the ground $Y(\omega)$ and the input is the force $F(\omega)$. The mobility between the two points, one where the force is applied and one where the response is observed, can be written as $Y_{1,2}(\omega)$, so the velocity of the point 2 can be found as

$$v_2(\omega) = Y_{1,2}(\omega)F(\omega) \tag{2.23}$$

If the system is linear the superposition of the effects of different point can be used to obtain the velocity of the point 2 due to different points of excitation.

$$\tilde{v}_2(\omega) = \sum_{m=1}^{N} Y_{m,2}(\omega)F_m(\omega) \tag{2.24}$$

where $\tilde{v}_2(\omega)$ is the velocity due to different point of excitation.

Sometimes, in order to get more significant results, it could be better to use the power spectral density (PSD) of the variables of interest, this turns equation (2.23) into

$$v_2^*(\omega)v_2(\omega) = Y^*(\omega)F^*(\omega)F(\omega)Y(\omega) \tag{2.25}$$

where * is the complex conjugate. This is the idea at the base of the linking process.

The link between the two models is made by multiplying the force spectra obtained from the track/vehicle interaction model, including the cross spectra, with the mobilities of the ground. The applied forces at the ground surface are converted into power spectral densities and cross power spectral densities and written into the matrix $\boldsymbol{S}_{FF}$. It is important to include all the cross spectral densities as these include the information about the relative phase of each force that takes into account the movement of the wheels along the track. So the response at the receiver is given by

$$S_{ww} = \boldsymbol{Y}^H \boldsymbol{S}_{FF} \boldsymbol{Y} \tag{2.26}$$

where $\boldsymbol{Y}$ is the matrix of the transfer mobilities of the ground, ^{H} is the Hermitian transpose (complex conjugate transpose) and S_{ww} is the power spectral density of the ground velocity at the receiver.

2.3.1 Forces post process

From the time domain integration the forces from underneath the sleepers can be extracted. Since the sleepers have been modelled as lumped masses and spring elements, from the track/vehicle model the forces from the sleepers spring are extracted. Because the time domain integration needs a very long computational time the length of the rail considered for the simulation time considered might be too short in order to get a consistent result as output. At this purpose, since the forces from the sleepers are not very different, these can be copied in order to have with the same computational time a much larger set of outputs. At this purpose a zero padding, [32], has been used. Zero padding a time history means that the time history is increased by adding a set of zeros. This does not add any new information to the frequency response but it increases the frequency resolution.

Fig 2.2 shows an exhample of the force from underneath a sleeper obtained from the time domain integration. The negative sign of the force is due because of the conventions taken of the Z axis pointing upwards. The lower spikes are due because of the passage of the wheelset on the node of interest and, since the train used in this case is composed of one car and four wheelsets, one sleepers sees 4 maxima. The positive maxima are due to the deformation of the rail in the approach of the wheelset to the sleeper. This or a series of this forces, depending on how many forces from the sleepers

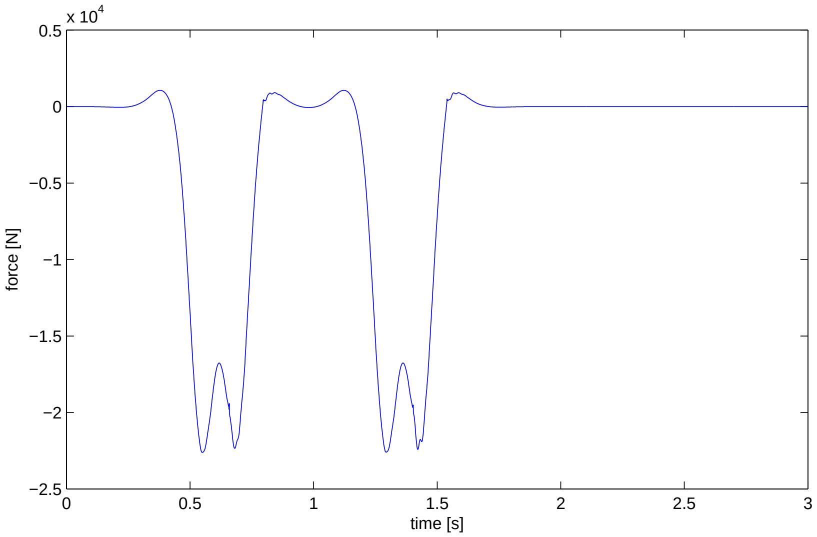

Figure 2.2: Force time history from underneath a sleeper

are extracted from the time domain simulation, can be replicated, with the right delay, to obtain a longer time domain simulation but still keeping the computational time reasonable. As shown in Section 3.2 the forces given as imput to this method do not need to be all the same. This is due because of the possibility of a model of the rail that considers also some kind of irregularity that amplifies the response of the ground at the receiver.

Once the forces are obtained and copied, if needed, the Fourier transform of the time history of these has to be performed, defined as

$$F_g(\omega) = \int_{-\infty}^{+\infty} f_g(t)e^{-j\omega t}\,dt \tag{2.27}$$

where f_g is the time history of the forces from underneath the sleepers, ω is the circular frequency and F_g is the spectra of the force in the frequency domain. Since the time history of the force is not infinitely long and it's not continuous but discrete equation (2.27) can not be used but the discrete Fourier transform (DFT) is required. Here the fast Fourier transform (FFT), [32], which is a faster algorithm to compute the DFT of a signal, implemented in MatLab has been used.

Once the frequency spectra $F_g(\omega)$ of every force is obtained matrix $\boldsymbol{S}_{FF}$, of the PSD and cross PSD of the forces, can be obtained. The PSD or cross

PSD of a signal is defined in, [32], as

$$\boldsymbol{S}_{F_iF_j}(\omega) = \frac{F_i^*(\omega)F_j(\omega)}{T} \tag{2.28}$$

where $i = 1, 2, ..., N$ and $j = 1, 2, ..., N$ where N is the number of sleepers considered and F_i^* is the complex conjugate of the spectra of the force underneath the i-th sleeper and T is the total time of the force time history. As result this gives a $N \times N$ matrix organized as

$$\boldsymbol{S}_{FF}(\omega) = \frac{1}{T} \begin{bmatrix} F_1^*F_1 & F_1^*F_2 & \cdots & F_1^*F_N \\ F_2^*F_1 & F_2^*F_2 & & \vdots \\ \vdots & & \ddots & \\ F_N^*F_1 & \cdots & & F_N^*F_N \end{bmatrix} \tag{2.29}$$

In the end a square matrix, per every frequency, is obtained.

2.3.2 Ground post process

From the frequency-wavenumber domain, as seen in Section 2.2.4, two matrices, one with the displacements, $|w(x)|$, and one with the phases, $\varphi(x)$, are obtained. To get the transfer mobilities first the complex number of the displacement have to be rebuild as

$$\alpha(x) = |w(x)|e^{j\varphi(x)} \tag{2.30}$$

Equation (2.30) represents the receptance of the ground for every node in the x direction. From these the whole set of receptances the ones of the node of interest have to be extracted. Since WANDS sorts the results in such a way that the node is related to the number of wavenumbers gave as input to WANDS, the node of interest is easily found.

Because WANDS does not give a reconstruction of the space in the x direction this has to be obtained from the wavenumber range and discretization used for the frequency-wavenumber integration through the relation $\lambda = 2\pi/k$. The position of the sleepers is known, since the spacing of the sleepers is known from the FE model of the track, so once the third dimension is reconstructed the transfer receptances of the ground can be extracted and turned into transfer mobilities by multipling the receptances by $j\omega$.

$$Y_i(\omega) = j\omega\alpha_i(\omega) \tag{2.31}$$

where Y_i is the mobility of the ground for the i-th sleeper considered. Once the mobilities of the sleepers are obtained the matrix $\boldsymbol{Y}$ of the transfer mobilities of the ground can be assembled as

$$\boldsymbol{Y} = \begin{Bmatrix} Y_1 \\ Y_2 \\ \vdots \\ Y_N \end{Bmatrix} \tag{2.32}$$

In [24] the receiver position was steady and the sleeper position was changing, in this case, since with WANDS this can not be done, the idea is to move the receiver instead in order to extract the right transfer mobilities of the ground.

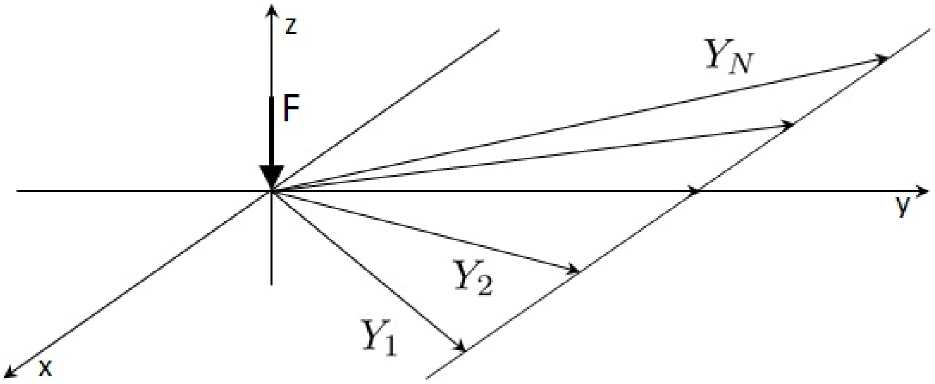

Figure 2.3: Idea of moving the receiver to obtain transfer mobilities

Fig. 2.3 shows the idea of moving the receiver in order to obtain the transfer mobilities of the ground between the forced point and the 'moving' receiver.

Once the matrix of the forces, $\boldsymbol{S}_{FF}$, and the matrix of the ground mobilities, $\boldsymbol{Y}$, are obtained the ground response to the pass-by of the train, S_{ww}, can be obtained from equation (2.26), it has only to be careful about the frequencies since the time domain and the frequency-wavenumber domain models might have a different frequency discretization, so a linear interpolation might be needed in order to obtain the same frequency for either case.

Chapter 3

Time domain model

This Chapter describes the input models for the Polimi time domain track vehicle interaction program and its outputs.

Section 3.1 presents the finite elements model of the rail, of the tunnel and a particular case of the rail with a joint. The specifications for these models have been found in the CONVURT project [26] where an intense experimental campaign has been carried on to investigate the problem of ground-born noise and vibration, an extract of the data is also reported in Appendix A. These models will be used as input to the time domain numerical integration. In order to better understand the physics of the problem also two analytical models for the track are presented and compared with the results from the frequency response of the FE model of the track. Three different configuration have been prepared to simulate the pass-by of the train

- Finite element model of the rail
- Finite element model of the rail coupled with the tunnel
- Finite element model of the rail containing a singularity, a joint, coupled with the tunnel

In Section 3.2 are presented the results from the time domain integration with the Politecnico di Milano model of the train/track interaction. Firstly in Section 3.2.1 an analytical model is used to better understand the physics of the contact force by inspecting in detail every component. It starts by studying the rail and wheel mobilities which are the main causes of the contact force, than it studies the mobility of the contact stiffness that couples the wheel with the rail. In the end it studies the roughness that is the main cause of the magnitude and variability of the contact force. Sections 3.2.2 to 3.2.4 present the contact forces and the forces transfered to the ground (or tunnel invert) using the different FE models presented. In the end a comparison between the forces obtained with the different models is presented.

3.1 Inputs for Polimi time domain model

This Section presents the FE models that have been used as input to the time domain track/vehicle interaction program.

It starts with the FE model of the rail and the frequency responses are presented. Than three different analytical models have been used to increase the knowledge of the problem. It will be seen that for the case of structural noise even a simplified model of the rail, like the Euler-Bernoulli beam used for the FE model, is sufficient.

After all the models of the rail are presented a comparison between them explaining the differences and trying to fit them in order to get a close response with all the different models it is made.

At last the FE model of the rail coupled with a FE model of the tunnel and a FE model of the rail containing a joint coupled with the FE model of the tunnel are shown. The first model helps to inspect the differences between the frequency response of the rail with and without the tunnel and it helps to understand if the tunnel has an influence on the receptance of the rail and also on the forces generated from the passage of the train. The second is prepared in order to inspect the influence of an irregularity on the forces generated by the passage of the train and the response of the ground at such a force.

3.1.1 Finite Element Model of the rail

At first has been considered the track alone, withouth the coupleing with the tunnel, in order to compare the results from the FE model with some analytical models.

The FE model of the track has been assembled, as shown in fig. 3.1, using for the rail Euler-Bernoulli beam elements 0.508 m long. The sleepers have been modelled as a lumped masses placed at 1.016 m apart so it means that the sleepers are modelled every other node of the rail structure, witch is a bit higher than the actual distance found in [26]. This approximation makes it much easier to eventually couple the rail to a model of the tunnel, which is a periodic structure 0.508 m long. As the track is directly attached to the sleepers, the springs in the model are ment to represent just their local compliance.

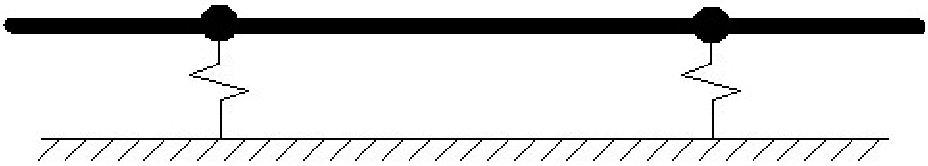

Figure 3.1: Scheme of the FE model of the track

Between the sleepers the FE model of the rail has only one node. This is a limitation for the response at high frequency but since the range of interest for ground vibration goes up to 200-250 Hz it does not affect the results obtained with this approximation, [1]. Since the same model was used for the pass-by of the train, computational time is high and so the number of nodes must be kept low. Also the choice of the Euler-Bernoulli beam has limitation at high frequency because it gives a lower output compared to the Timoshenko beam but, for the same reason, it does not represent a problem, [33]. To determine the following receptances a 48.768 m FE track model has been built. In this model the two rails are totally independent because, since the sleepers are seen has lumped masses, there is no connection between the two sides.

Fig. 3.2 shows the receptance obtained with the FE model. It can be noticed that the model is able to represent the 'pinned-pinned' resonance. From the phase graph it can be seen that at low frequency the track model can be approximated as a spring like structure being the phase near 0 degree and the magnitude flat: the stiffness of the springs are the dominant effect. At high frequency the receptance of the track is like the receptance of a beam, being the phase is near -135 degree and the amplitude proportional to frequency to the power 3/2.

As a consequence of this behavior the frequency responses at midspan and over the sleeper are very close, the mass of the rail acts only as a shift

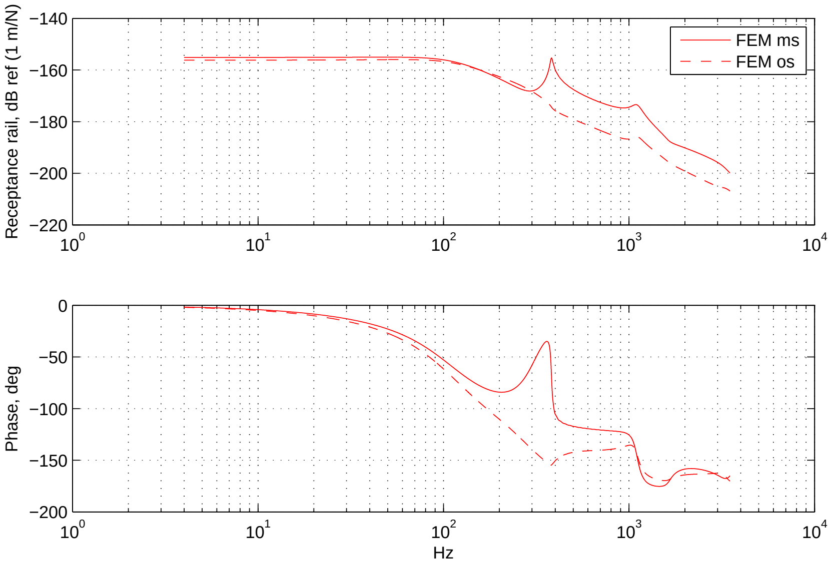

Figure 3.2: FE model rail receptance

in fact the receptance over the sleeper is lower than the one at midspan.

In the range between 300-500 Hz there is a big difference between the two responses because in that range it is present the ‘pinned-pinned’ resonance. Since the ‘pinned-pinned’ mode is connected to the length of the span between the sleepers and it excite the modes of an equivalent simply supported beam of the length of the span it gives a big displacement at midspan and a small one at the sleepers positions.

Fig. 3.3 shows the receptance obtained from the FE model compared with the experimental data. From fig. 3.3 it can be seen that at very low frequency there is a difference between the frequency response of th FE model and the experimental one, this, as said before, it is probably due to some errors in the measurements since the frequency range is very wide. Other than that though the model seems to reproduce well the frequency response of the rail, the ‘pinned-pinned’ mode is in the right position and the hight of it is respected. Still there is a bit of difference at high frequency between the over the sleeper responses, this is probably due to the use of the Euler-Bernoulli beam for the FE model but, as said before, since this range is not of interest it does not represent a problem.

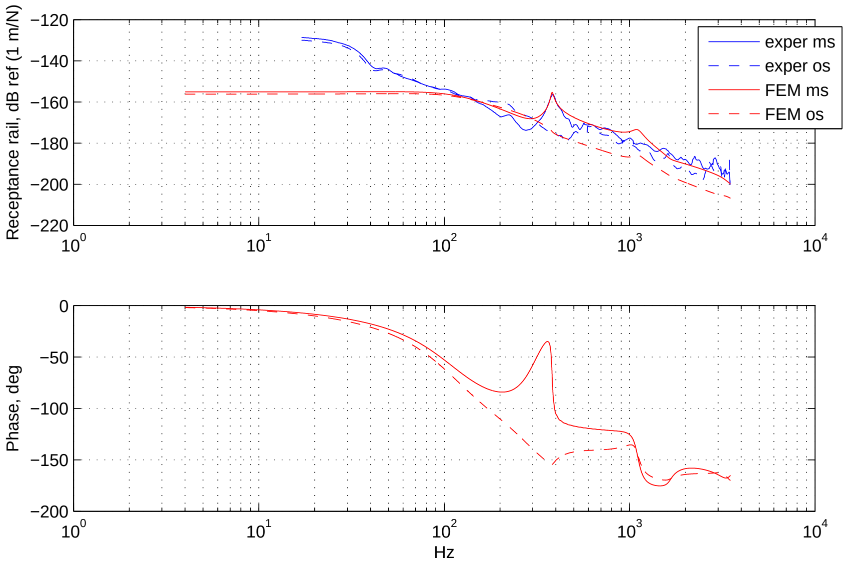

Figure 3.3: FE model rail receptance vs experimental data

3.1.2 Analytical models

Two different analytical models have been use to better understand the dynamics of the rail and to increase level of confidence. One is based on the principle that the track is an infinite beam and lays on a continuous elastic bed, so for this model all the parameters have been converted in per unit length characteristics; the second one is an infinite beam laying on a discrete number of supports. The main difference between the two model is that in the continuous spring bed the ‘pinned-pinned’ frequency is not visible while in the othe model it is.

Continuous elastic bed

This model has been widely used during the last decades to model track vibration for rolling noise simulation and it is normally applied to rail-pad-sleeper-ballast tracks, and its formulation is mainly reproduced in [10]. By setting properly the parameters’ values it can be adopted to descibe the case under study. The system rail-pad-sleeper-ballast or ground can be seen as a continuous two layers support beneath an infinite rail, so that the pad stiffness, the sleeper mass and the ballast stiffness have to be scaled per unit length to fit in the model.

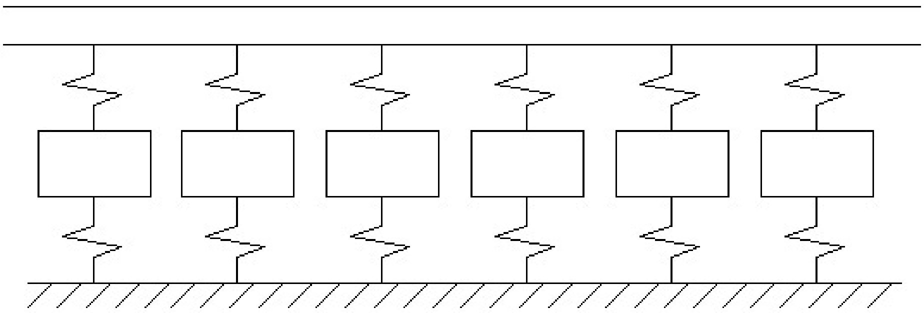

Figure 3.4: Representation of the model on a continuous two layers bed

For this analytical model the rail has been modeled as an infinite Timoshenko beam witch has a better response at high frequency but it is not much different from the the response at low frequency of the Euler-Bernoulli beam.

The two springs' bed and the sleeper's mass can be modelled as a single equivalent frequency dependent stiffness

$$s(\omega) = \frac{s_p \left(s_b - \omega^2 m_s'\right)}{s_p + s_b - \omega^2 m_s'} \tag{3.1}$$

Where s_p, s_b and m_s' are the pad stiffness, the ballast stiffness and the mass of the sleeper per unit length respectively. If we consider the limits we can see that: at low frequency, $\omega \mapsto 0$, the equation (3.1) can be approximated as

$$s(\omega) \mapsto s_0 = \frac{s_p s_b}{s_p + s_b} \tag{3.2}$$

Where s_0 is the equivalent stiffness of the two springs in series. In this particular case $s_b \ll s_p$, since the fasten is considered to be rigid, we can approximate $s_0 = s_b$. At high frequency, $\omega \mapsto \infty$, instead the equation (3.1) can be approximated as

$$s(\omega) \mapsto s_p \tag{3.3}$$

It is found that, for this system, two natural frequencies can be found

$$\omega_1 = \sqrt{\frac{s_b}{m_s'}} \tag{3.4}$$

$$\omega_2 = \sqrt{\frac{s_p + s_b}{m_s'}} \tag{3.5}$$

It is clear that for $\omega = \omega_1$ the equivalent stiffness $s(\omega_1) = 0$, this corresponds to the resonance of the sleeper mass on the stiffness of the ballast, while for $\omega = \omega_2$ the equivalent stiffness becomes $s(\omega_2) = \infty$, this corresponds to the resonance of the mass of the sleeper on the combined stiffness of the ballast and of the pad.

s_b	$4.3\ 10^7$	N/m^2
η_b	1.2	ballast loss factor
s_p	10^{16}	N/m^2
η_p	0.2	pad loss factor
κ_r	0.4	rail share coefficient
η_r	0.2	rail loss factor
m'_s	68.898	kg/m

Table 3.1: Continuous elastic bed parameters

It can be seen from table 3.1 that for the pad has been chosen a very high stiffness this because of the direct fasten of the rail on the sleepers. With this specifications it is obtained that $f_1 = 121.6$ Hz, while $f_2 = 1.8$ MHz so there is no movement between the rail and the sleeper.

After solving the partial differential equations' system the receptance α at a generic position x for a force applied at x' can be expressed as

$$\alpha(x, x') = u_1 e^{-j\, k_e |x - x'|} + u_2 e^{-j\, k_p |x - x'|} \tag{3.6}$$

Where u_1 and u_2 are

$$u_1 = -\frac{k_e^2 + C_1}{GA\kappa_r(1 + j\eta_r)(4k_e^3 + 2C_2 k_e)} \tag{3.7}$$

$$u_2 = -\frac{k_p^2 + C_1}{GA\kappa_r(1 + j\eta_r)(4k_p^3 + 2C_2 k_p)} \tag{3.8}$$

It is obvious that if the receptance of the rail considered in the same point where the force has been applied it can be found that equation (3.6) becomes

$$\alpha = u_1 + u_2 \tag{3.9}$$

Where A is the area of the section of the rail, κ_r the Timoshenko share modulus, G is the tangential modulus of elasticity. It can be obtained that

k_e and k_p are the wave number and can be determined as

$$k_e = \sqrt{-\frac{C_2}{2} + \frac{\sqrt{C_2^2 - 4C_3}}{2}} \tag{3.10}$$

$$k_p = \sqrt{-\frac{C_2}{2} - \frac{\sqrt{C_2^2 - 4C_3}}{2}} \tag{3.11}$$

The terms C_1, C_2 and C_3 are given by the following equations

$$C_1 = \frac{\rho_r J_{22}\omega^2 - GA\kappa_r(1 + j\eta_r)}{EJ_{22}(1 + j\eta_r)} \tag{3.12a}$$

$$C_2 = \frac{m'_r\omega^2 - s(\omega)}{GA\kappa_r} + \frac{\rho_r J_{22}\omega^2}{EJ_{22}(1 + j\eta_r)} \tag{3.12b}$$

$$C_3 = \frac{m'_r\omega^2 - s(\omega)}{EJ_{22}(1 + j\eta_r)} \left(\frac{\rho_r J_{22}\omega^2}{GA\kappa_r} - 1 \right) \tag{3.12c}$$

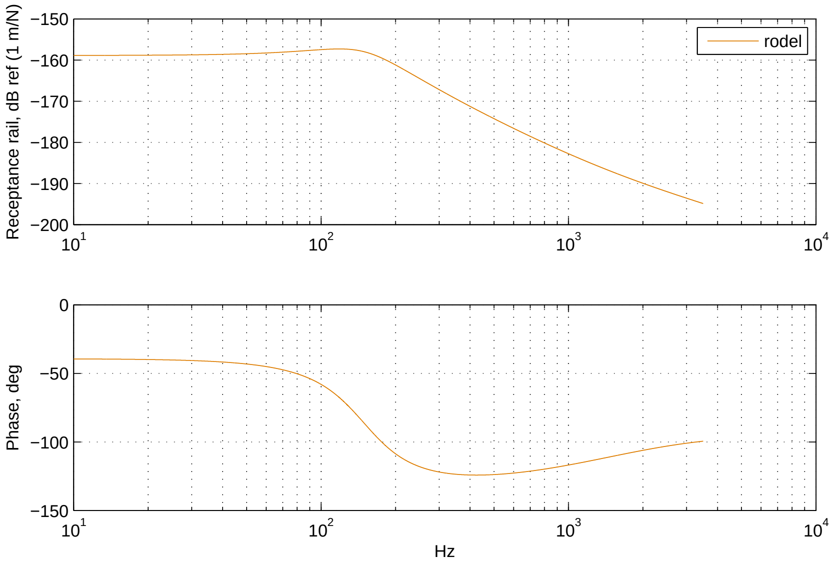

Figure 3.5: Continuous two layers elastic bed rail receptance

Fig. 3.5 shows the receptance obtained with the model presented above and with the characteristics considered. It can be noticed that in this case the receptance seems much like the one obtained with a simple mass-spring system, this is due to the high stiffness of the rail pad so the rail and the sleeper move together as a single mass. Another evident thing that can be seen is that this model does not show any ‘pinned-pinned’ mode because there is no discrete separation between the sleepers, this might be a big approximation.

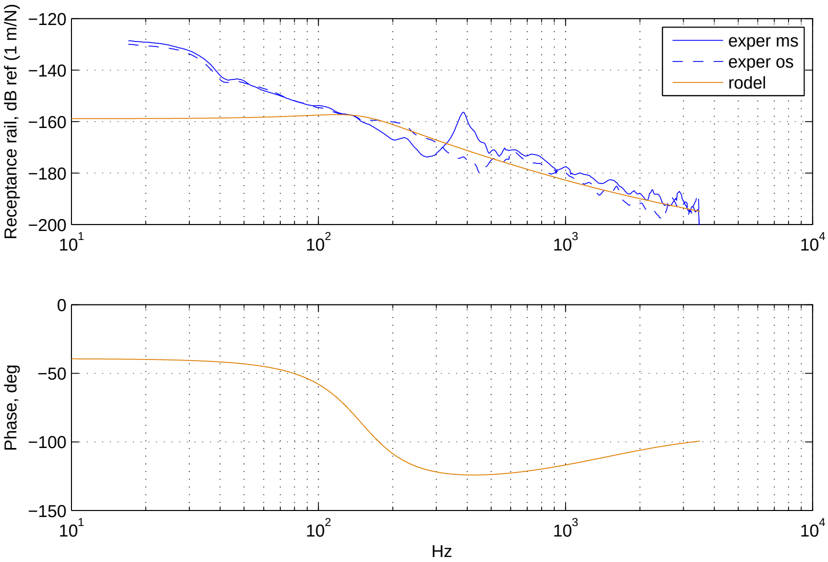

Figure 3.6: Continuous two layers elastic bed rail receptancel vs experimental data

In fig. 3.6 is shown a comparison between the results obtained with the continuous model and the experimental data. At low frequency there is always the problem with the experimental data but this result gives more confidence with what stated before. At hight frequency, since the response is controlled by the beam and the mass of the two rails should not be different from the experimental one, the response of the model is close to the experimental one, it can be seen that comparing this results with the one from fig. 3.3 there is a better fitting with the experimental data probably due to the use of the Timoshenko beam. As said before between 300-500 Hz the continuous model does not fit well the experimental data because it can not reproduce the ‘pinned-pinned’ mode. Moreover in this case it is not possible to divide the response obtained over the sleeper from the response obtain at midspan.

Discretely supported track

The analytical model for the discretely supported track, reported in [10], is very similar to the one just presented. In fig. 3.7 is presented a drawing of the model.

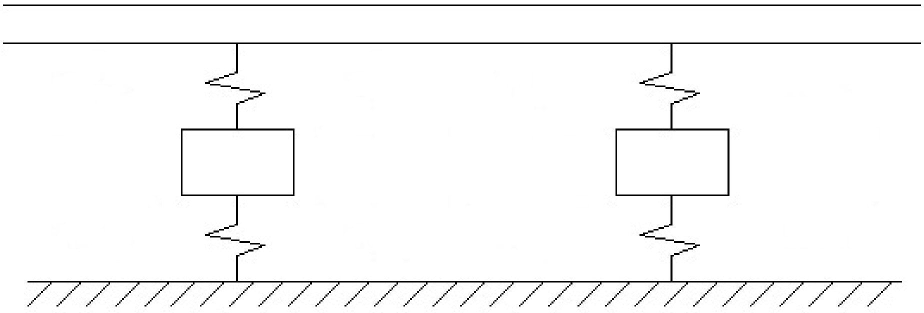

Figure 3.7: Discretely supported track model

The rail, again modelled as an infinite Timoshenko beam, instead of laying on continuous two layers elastic bed is supported by a discrete number of sleepers. The math behind this model is the same of the continuous two layers bed with the only difference that instead of using $s(\omega)$ it has to be used $K(\omega)$ that is the dynamic stiffness for each support separated by a spacing d_z.

$$K(\omega) = \frac{K_p\left(K_b - \omega^2 m_s\right)}{K_p + K_b - \omega^2 m_s} \tag{3.13}$$

Where K_p, K_b and m_s are the stiffness of the pad, the stiffness of the ballast and the mass of the sleeper. So substituting $s(\omega)$ with $K(\omega)$ in equation (3.12) it is possible to obtain u_1, u_2 and the rail receptance α can be obtained from equation (3.9) for a discretely supported Timoshenko beam rail.

Fig. 3.8 shows the rail receptance obtained with the discretely supported analytical model with the same rail and supports parameters use in the FE model and in the continuous two layers bed. With this model the ‘pinned-pinned’ modes and the receptance of the rail above the sleeper and at midspan can be obtained. It can be seen that at low frequency the receptance is flat because the model is spring like and the two responses are close because in this range of frequencies is the ballast stiffness that controls the response. At high frequency the response is the one of the beam but

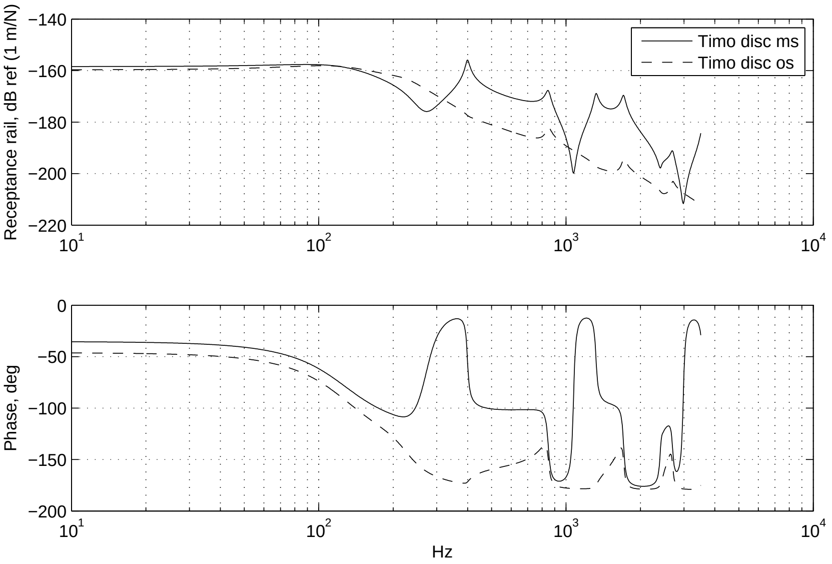

Figure 3.8: Discretely supported rail receptance

it can be seen that are present a lot of resonances that were not present in fig. 3.2, those are higher ‘pinned-pinned’ modes that cannot be seen from the FE model due to the lack of elements between the sleepers to obtain shorter computational time.

It can be seen from fig. 3.9 that at low frequency there is the same problem with the experimental data, at high frequency there is a fine correspondence with the experimental data and that the ‘pinned-pinned’ resonance is not in the right position. Also the over sleeper response is well described by this model. In order to complete the analysis the rail bending stiffness has been decreased by a 8% to better fit the experimental data for the ‘pinned-pinned’ mode. Fig. 3.10 shows the analytical discrete model after the changing of the bending stiffness.

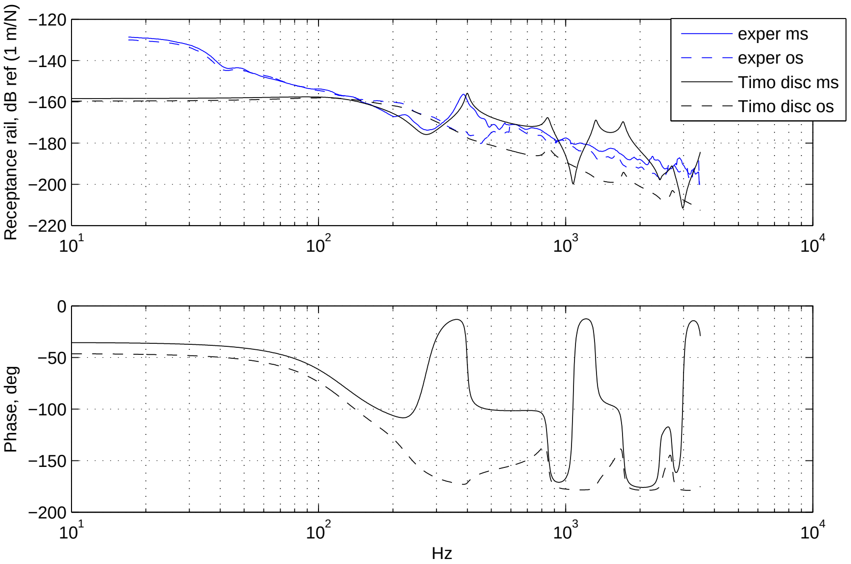

Figure 3.9: Discretely supported rail receptance vs experimental data

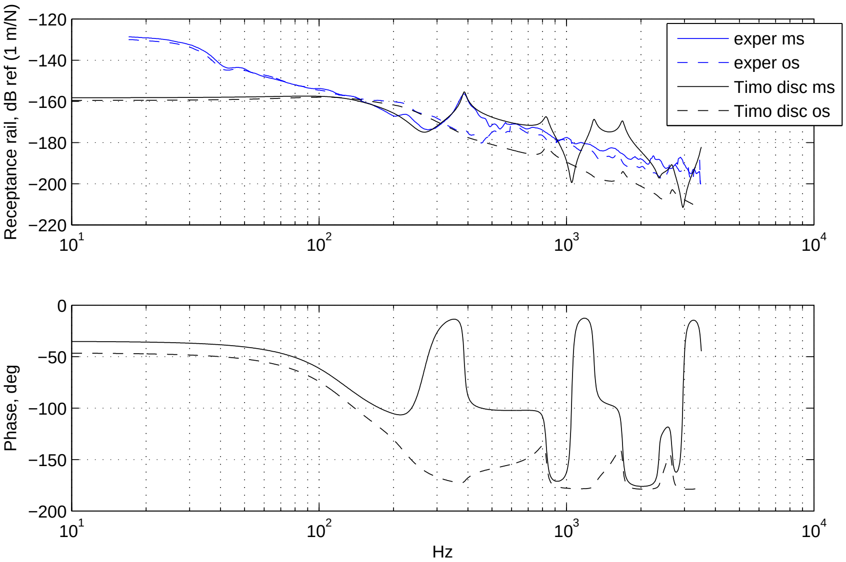

Figure 3.10: Discretely supported rail receptance vs experimental data after parameter tuning

3.1.3 Comparison between analytical and numerical models

Since both, the analytical and the numerical models, represent well the experimental data found in the CONVURT project it could be useful to see if there are differences between them. Usually the numerical model needs a higher computational time than the analytical model, on the other hand the analytical solution can be found only for simple geometries while for more complex ones the numerical solution is the only way.

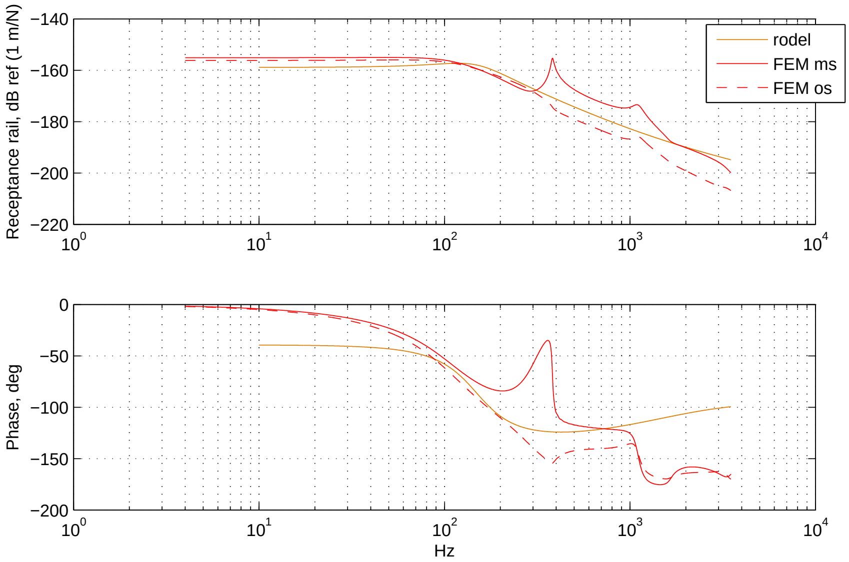

Figure 3.11: FE model vs continuous two layers elastic bed rail receptance

Fig. 3.11 shows the receptance obtained with the FE model compared with the one obtained with the analytical continuous two layers elastic bed. It can be found that for frequencies up to 300 Hz the two models are quite similar, while for higher frequencies they become a bit different mainly due to the absence of the 'pinned-pinned' mode. At frequencies higher than 1 kHz the analytical model has a higher response due to the nature of the Timoshenko beam element used in this case.

Fig. 3.12 presents the receptance obtained with the FE model compared to the one obtained with the analytical discretely supported track. In this case it can be seen that the rail receptance obtained with both models is really close. At low frequency the two models give almost the same response, the 'pinned-pinned' mode is described by both models even if with the same

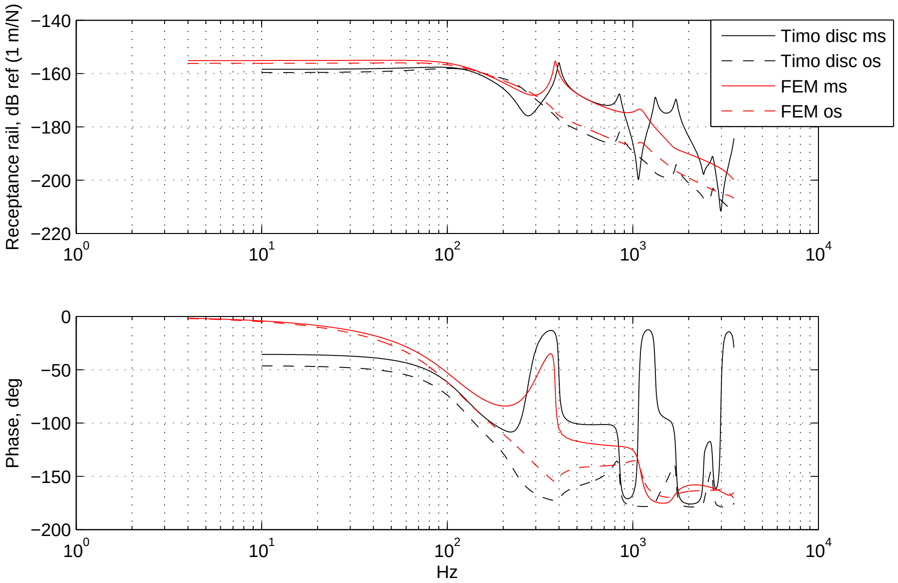

Figure 3.12: FE model vs discretely supported track rail receptance

parameters there are differences in the position of the peak, at higher frequency the analytical model presents a lot of narrow picks that are not seen from the numerical model, this are the higher 'pinned-pinned' modes that cannot be reported from the FE model that has been implemented because, in order to be able to show thees resonances more nodes between the sleepers are needed. Also for this case in fig. 3.13 is reported the comparison between the two model with a change in the bending stiffness of the rail for the analytical discretely supported track model.

In order to give a complete overview of all the models and to summarize the results from fig. 3.14 to fig. 3.17 are reported all the frequency responses divided in main span and over the sleeper with and without the optimization of the property of the rail for the analytical discrete model.

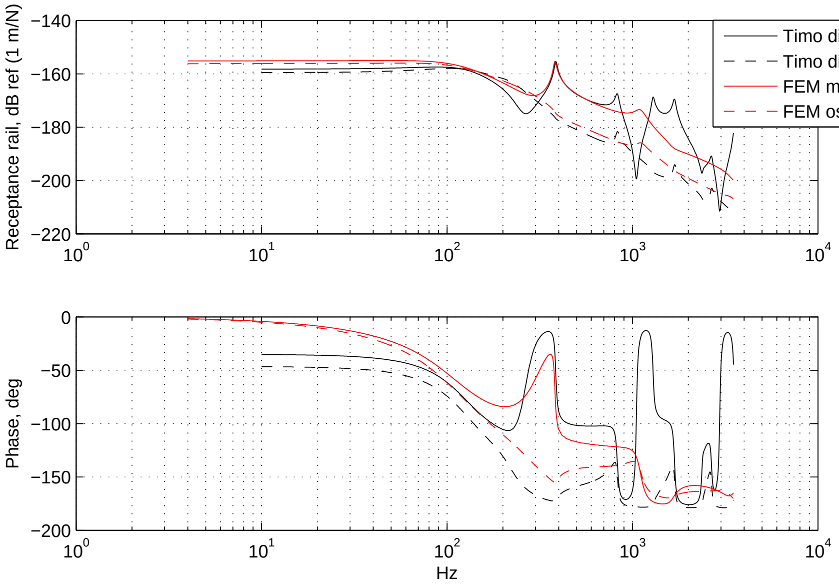

Figure 3.13: FE model vs discretely supported track rail receptance with tuned parameters

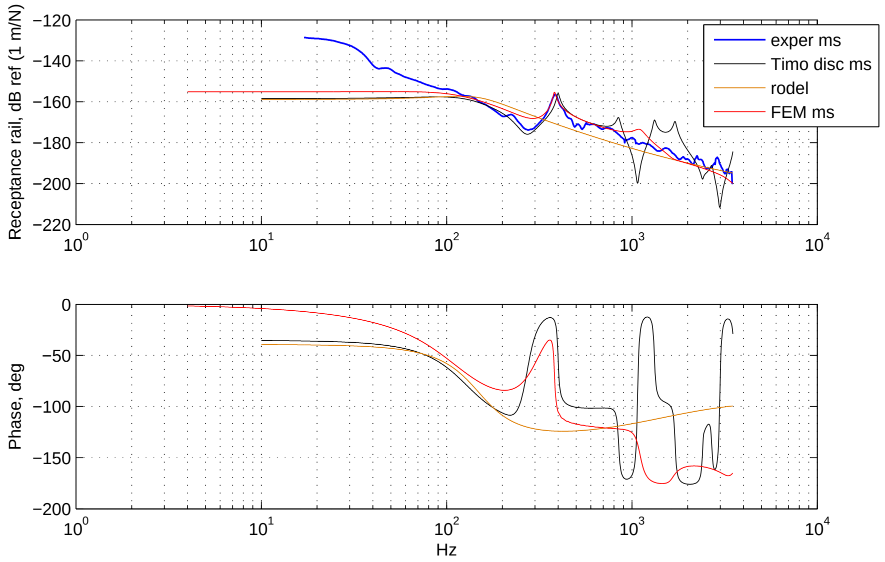

Figure 3.14: FE model, discretely supported track, continuous two layers bed without tuned parameters rail receptance main span vs experimental data

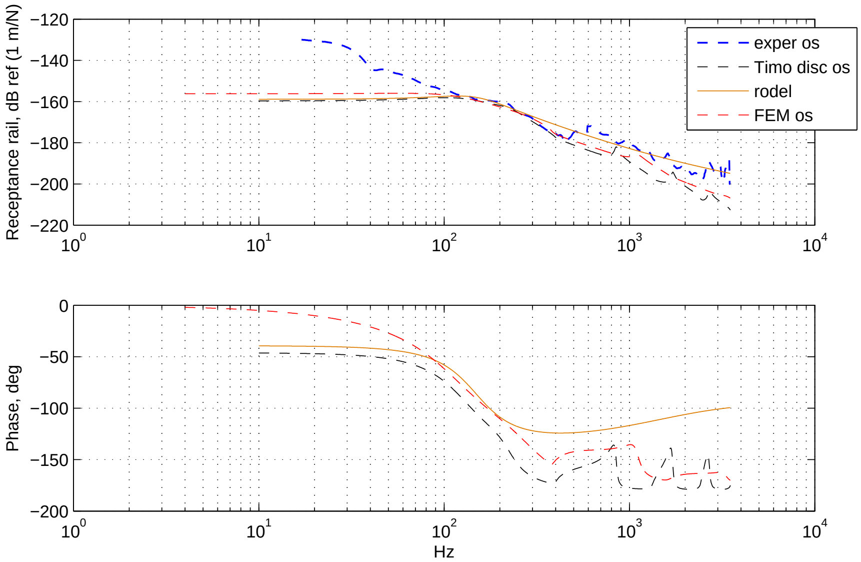

Figure 3.15: FE model, discretely supported track, continuous two layers bed without tuned parameters rail receptance over sleeper vs experimental data

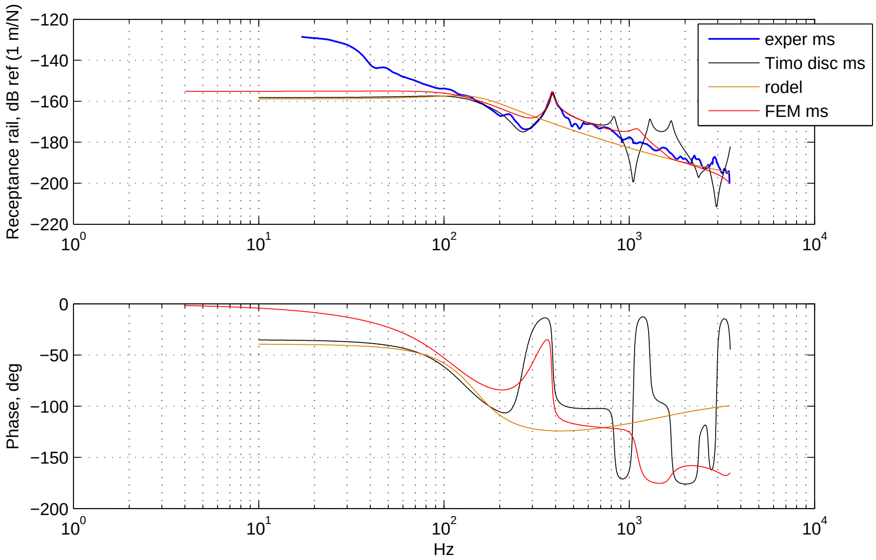

Figure 3.16: FE model, discretely supported track, continuous two layers bed with tuned parameters rail receptance main span vs experimental data

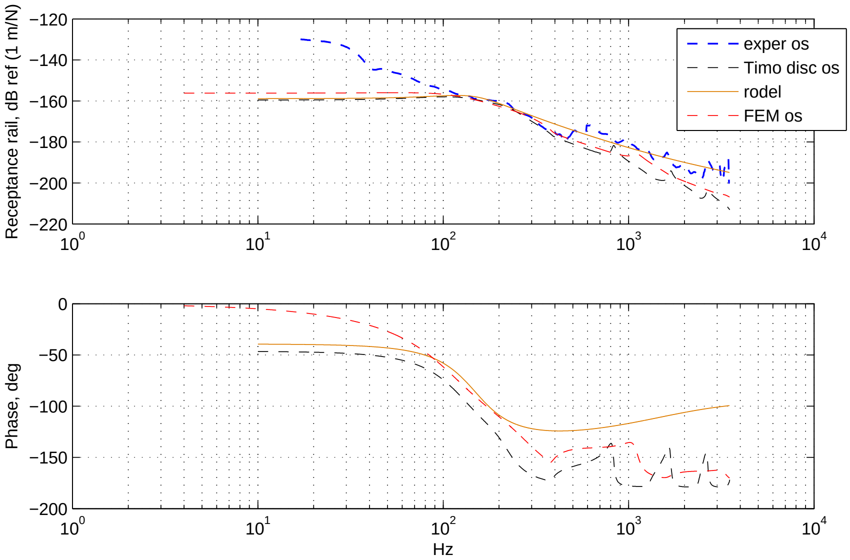

Figure 3.17: FE model, discretely supported track, continuous two layers bed with tuned parameters rail receptance over sleeper vs experimental data

3.1.4 Extension of the FE model

Since the FE model can have any shape two main variations to the previous model of the rail alone have been produced. The first, where the FE model of the tunnel is attached to the rail, in order to investigate the influence of the tunnel on the frequency response of the rail and on the time domain calculation. The second is a FE model of the rail and tunnel but this time the rail has an irregularity.

Many types of irregularity can be found on the rails, [34]: corrugation, which consists of a periodic wear of the rail of a certain length due to different mechanisms; switches, these make possible to the train to change lane; and joints, these are used to connect two different pieces of rail, a little gap is left between the pieces to allow the rail to expand or shorten due to the changes of temperature during the year. The irregularity studied is the joint singularity. Even if nowadays the rails are mostly welded together some joints are still present due to the fact that it is not possible to keep hundreds of kilometer of rail together because, for example the change in dimension due to the temperature would cause big differences in change of length over the year. To avoid this issue the rails are still joined by these systems.

Tunnel

The structure of the tunnel has been modelled in order to see if there could be a considerable difference between the responses of the rail without the tunnel and the rail coupled with the tunnel.

In order to model the tunnel the circumference has been divided in 18 parts to obtain a symmetrical subdivision of the frame of the tunnel, while the tunnel invert has been divided into 7 parts. The longitudinal stiffeners and the circumferential stiffeners have been modeled as Euler-Bernoulli two nodes beam elements while for the rest of the tunnel four nodes plate elements, where the nodes are numbered in a clockwise direction, have been used. The plate elements are divided in two different types: one, used for the shell of the tunnel, is made of cast iron, while the other, used for the tunnel invert, is made of concrete. The rail used for this model is the same presented in Section 3.1.1. In order to attach the rail to the tunnel invert the spring elements have been coupled to the invert plate nodes, instead that to a rigid ground.

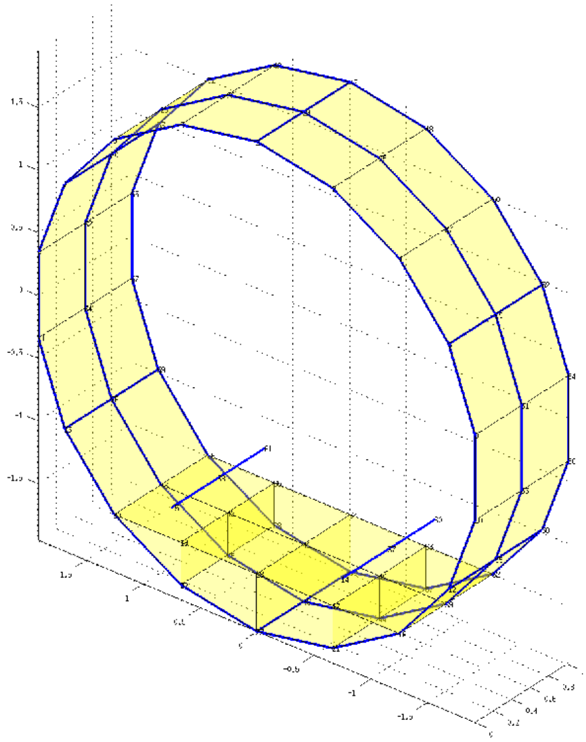

Figure 3.18: FE model of the tunnel obtained from the specifications of the CONVURT project

Fig. 3.18 reports a section of the tunnel 1.016 m long, with the track in it, modelled with the FE method. It can be seen that it represents well the drawing of the tunnel in fig. A.2. To reduce the edges effects on the response a bigger model has been assembled by summing 96 sections as the one presented in fig. 3.18 in this case a 97.536 m long tunnel with track is obtained. By exciting a node on the tunnel invert with a point force that sweeps all the frequencies of interest, the frequency response of the tunnel is obtained.

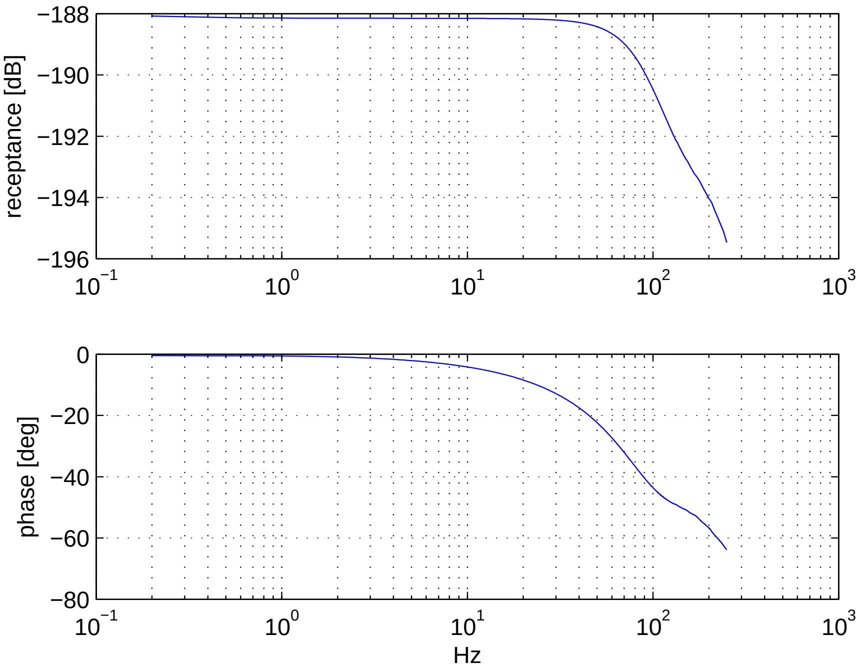

Figure 3.19: Receptance obtained with the FE model of the tunnel

Fig. 3.19 shows the receptance of the tunnel for a point force in the center of the invert. It can be seen from [35] that there is a good agreement between the results obtained with the FE model and the experimental data. By exciting a node on the rail around the middle of the tunnel structure, as presented before, the frequency response of the rail coupled with the tunnel is obtained, this time instead of laying on a rigid soil it lays on the deformable tunnel invert.

Fig. 3.20 shows the receptance of the rail obtained using the FE model of the rail and tunnel coupled. It can be seen that the receptance with this

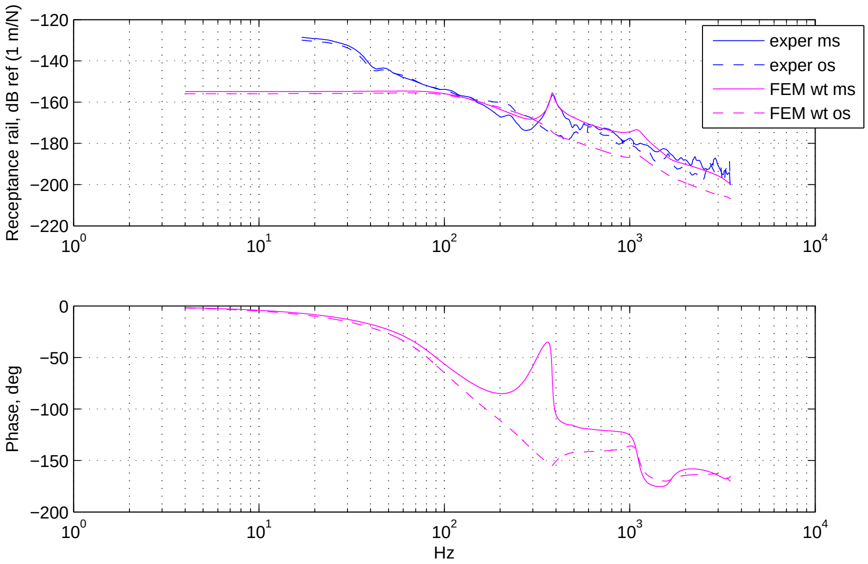

Figure 3.20: FE model with tunnel rail receptance

model is close to the experimental data.

Fig. 3.21 reports both the receptance of the rail with and without the tunnel. From this figure can be noticed that there is almost no difference between the two receptances. The biggest difference is at low frequency, for frequency up to 100 Hz there is a difference of 0.5 dB, while for higher frequencies the difference is very small.

Joint irregularity

In this case the model is really close to the one just presented but for the exception of the FE model of the joint. In order to reproduce this a section of the tunnel has been replaced with a section containing the joint.

The joint is made of two clamps hold together with bolts. Fig. 3.22 shows an example of a joint used in railways.

It has been assumed that the clamp is made of the same material of the rail. In order to build the FE model this irregularity has been divided into two halves, the left and right half. The rails on the right side of the left half and the rail on the left side of the right half have been shorten in such a way that after the two halves are connected a gap of 3 mm is left.

Since the clamp is symmetric its center of mass lays on its symmetry

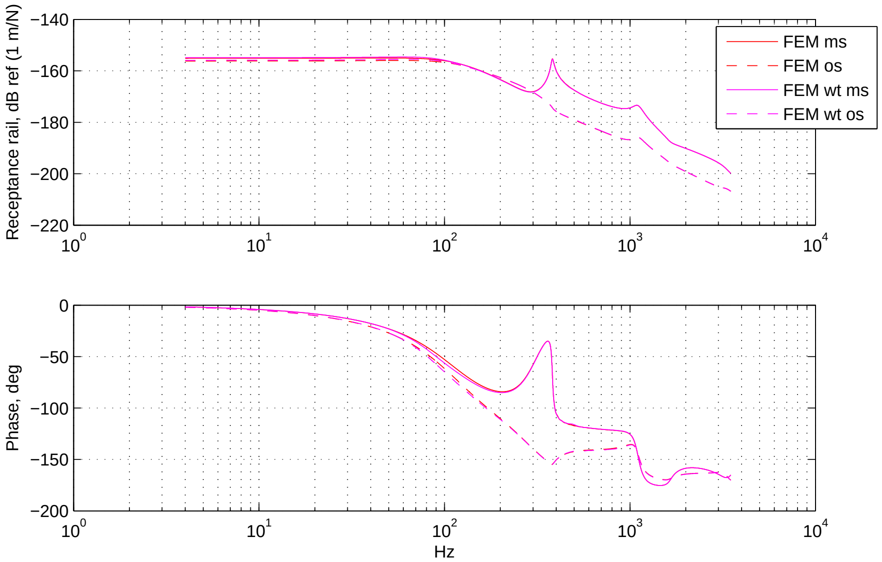

Figure 3.21: FE model with tunnel vs FE model without tunnel rail receptance

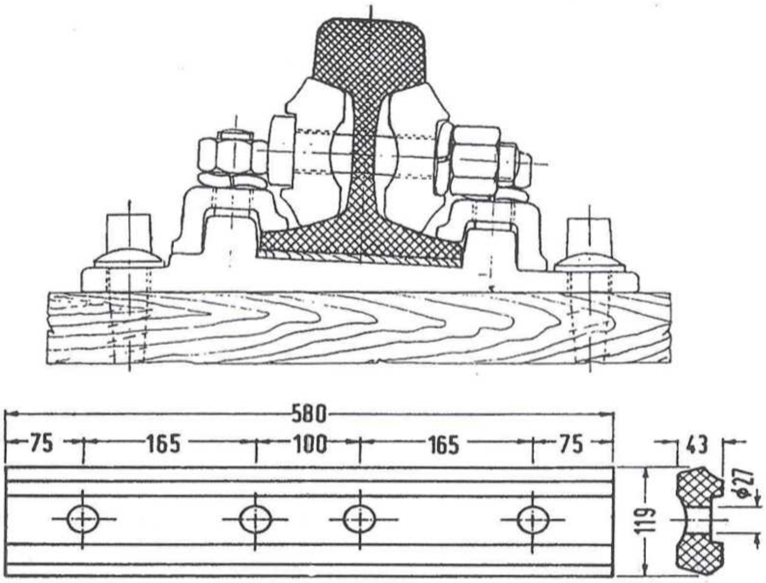

Figure 3.22: Section of the clamp and section of assembled joint with rail, [36]

axis. This give the possibility to place the clamp half way between the tunnel invert and the top of the rail. Table 3.2 shows the parameters used

A	$3.848\,10^{-3}$	m^2
I_2	$2.252\,10^{-6}$	m^4
I_3	$1.755\,10^{-6}$	m^4
J_p	$4.008\,10^{-6}$	m^4
J_T	$9.009\,10^{-6}$	m^4

Table 3.2: Clamp parameters for the joint

for the clamp of the joint calculated considering that the clamp is placed on both sides of the rail. In a real case the clamp is secured to the rail with a set of bolts. Since this is not possible in the FE model it has been decided to connect the clamp to the rail through four springs placed in the position of the bolts. By setting the right stiffness of the springs can be obtained the final configuration of the joint.

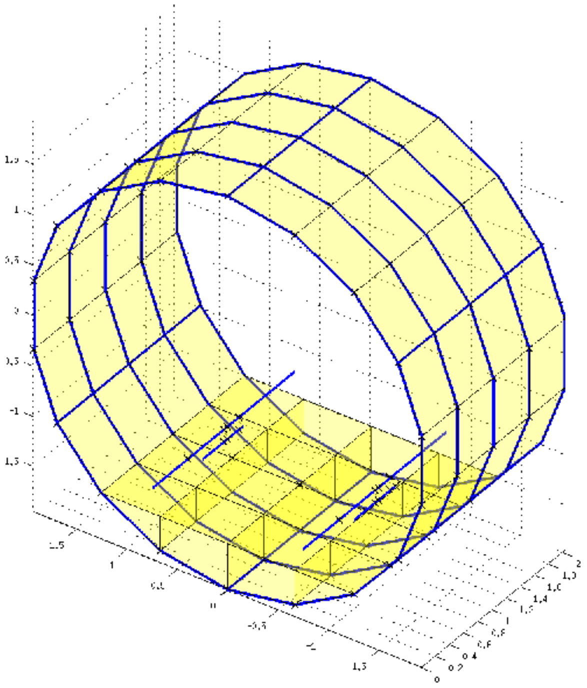

Figure 3.23: Finite element model of the section of the tunnel with the joint

Fig. 3.23 shows the FE model of the section of tunnel with the joint. From fig. 3.23 can be seen the position of the clamp, which is the beam underneath the rail, but not the gap left between the two sides of the rail because the scale is too big to see it.

The frequency responses for this model are the same as the ones shown in Section 3.1.4 so it is not interesting to report them. What changes in this case are the forces from the time domain integration. The singularity due to the gap gives a peak in the force as will be shown further on.

3.2 Results from the time domain integration

From the integration in the time domain of the FE model with the multibody model of the train, it is also possible to obtain the forces exchanged between the wheel and the track.

Firstly an analytical model of the contact forces is presented. It has been used to increase the understanding of the physical problem that generates the forces at the wheel/rail interface. In the second section the results from the numerical integration are presented. Here the finite element model of the track, the tunnel and the joint, presented in Section 3.1, has been used to obtain the contact forces.

3.2.1 Analytical simplified model for the contact forces

The wheel rail system can be seen as two dynamic systems connected at a point and excited by a relative displacement, due to the roughness of the wheel and rail. There is than a third system that represents the contact spring which is connected in parallel with the others.

Fig. 3.24 shows an example of the wheel-rail interaction system. The contact force is then a function of the wheel, rail and contact spring mobilities and of the roughness, as derived in [10].

$$F = \frac{j\omega r}{Y_r + Y_w + Y_c} \tag{3.14}$$

where r is the roughness, Y_r, Y_w and Y_c are the rail, wheel and contact spring mobilities respectively. All of the terms of equation (3.14) will be described in detail in the following Sections.

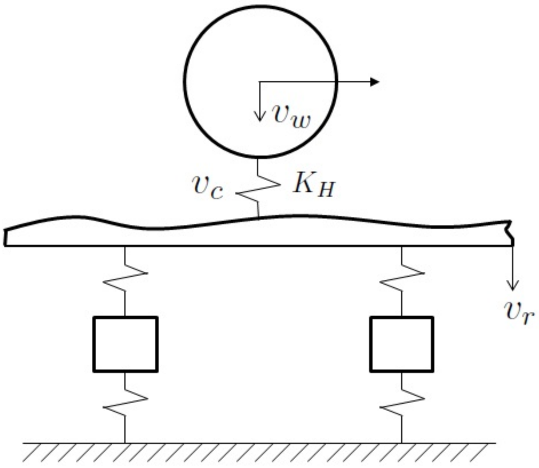

Figure 3.24: Model of the wheel-rail interaction mechanism

Rail mobility

If the rail is excited by a vertical harmonic force $F\,e^{j\omega t}$, where F is the complex amplitude and ω is the circular frequency, its velocity amplitude is

$$v_r = Y_r F \tag{3.15}$$

Where Y_r is the vertical rail mobility.

For the rail mobility are valid all the things explained in Section 3.1 except that the rail mobility is obtained from the rail receptance as

$$Y_r = \dot{\alpha} = j\omega\alpha \tag{3.16}$$

where α is the rail receptance.

Fig. 3.25 shows the mobility of the rail obtained using the FE model receptance of the rail without modelling the tunnel underneath the track. If the receptance of the track with the tunnel is considered the results shown in fig. 3.26 are obtained.

Fig. 3.25 and 3.26 are quite similar but at low frequency the mobility of the rail with tunnel is a bit lower than the one without, around 0.5 dB.

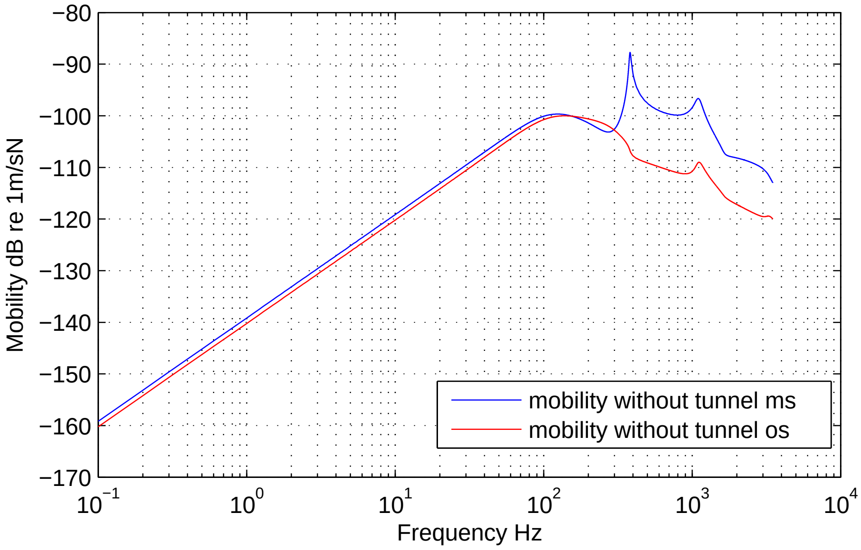

Figure 3.25: FE model rail mobility without tunnel

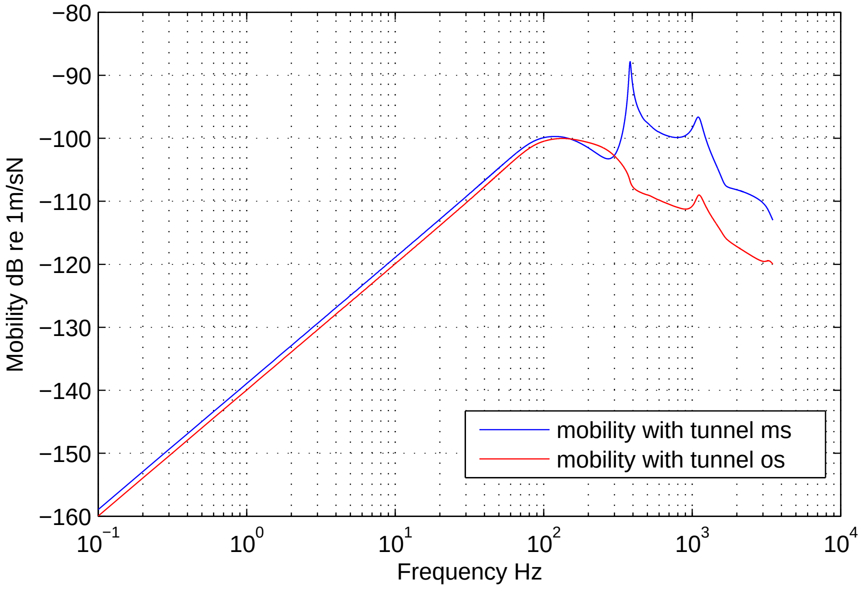

Figure 3.26: FE model rail mobility with the FE model of the tunnel

Wheel mobility

Since the same force that acts on the rail acts also on the wheel, the wheel velocity becomes

$$v_w = -Y_w F \tag{3.17}$$

Where Y_w is the wheel mobility. The negative sign is needed because of the sign conventions taken positive downwards and in this case the force has an upward direction. The mobility of a complex structure can be obtain with the modal summation as

$$Y_{jk} = \sum \frac{j\omega \Phi_{jn} \Phi_{kn}}{m_n \left(\omega_n^2 - \omega^2 + 2j\zeta_n \omega_n \omega\right)} \tag{3.18}$$

Where Φ_{jn} is the modeshape amplitude of the mode n at location j and m_n and ζ_n are the modal mass and modal damping ratio respectively. This technique can also be used to identify the wheel frequency response. The modeshape amplitudes and the corresponding modal masses can be obtained from a finite element calculation along with the natural frequencies. The damping has to be measured or using estimates based on measurements on other wheels.

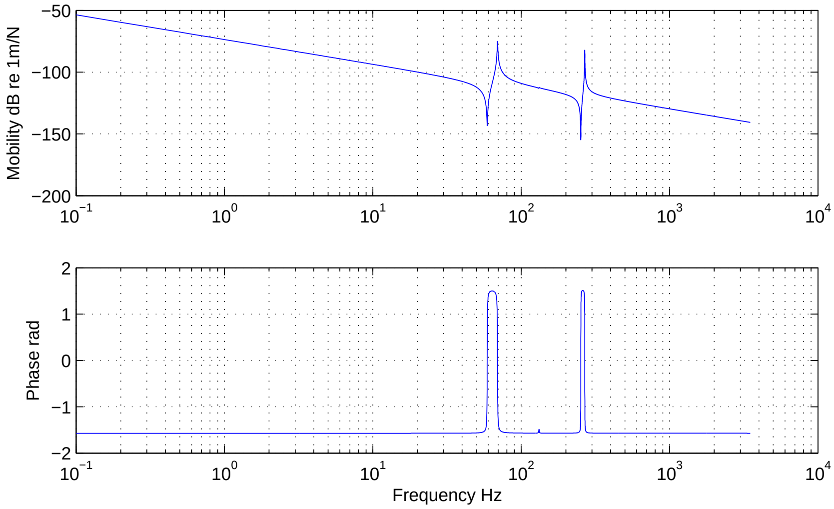

Figure 3.27: Wheelset mobility obtained with modal superposition

Fig. 3.27 shows the wheelset mobility obtain with the modal superposition of the first 4 flexural modes, including the rigid mode. It can be seen that at low frequency the mobility of the wheel is mass-like, this corresponds to the unsprung mass of the wheelset, M_w. So its mobility becomes

$$Y_w = \frac{-j}{\omega M_w} \tag{3.19}$$

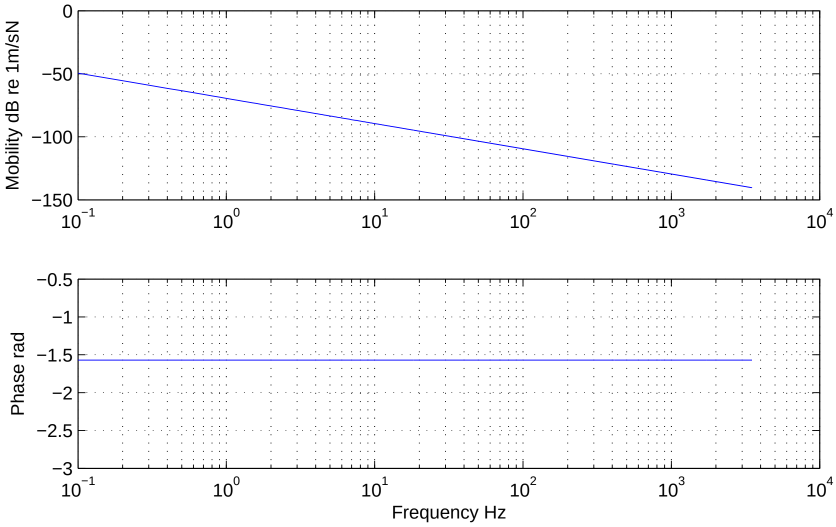

Figure 3.28: Wheel mobility with unsprung mass model

This approximation is valid up to 200 Hz if only the wheel is considered otherwise the wheelset flexural modes have to be taken into account. As a first approximation the wheel alone can be considered. Fig. 3.28 shows the mobility of the wheel for the unsprung mass model, if a grater frequency range it's needed, the anti-resonance at around 500 Hz has to be considered. This can be obtained by adding a spring in series with the mass. So the mobility of the wheel becomes

$$Y_w = \frac{j\left(M_w\omega^2 - K_w\right)}{K_w M_w \omega} \tag{3.20}$$

Where the value of K_w is chosen to best fit the anti-resonance frequency.

Fig. 3.29 shows the wheel mobility obtained with equation (3.20) it can be seen that up to 200 Hz the mobility of the wheel is mass-like and from 500 Hz up to 1.5 kHz is spring-like for higher frequencies this approximation

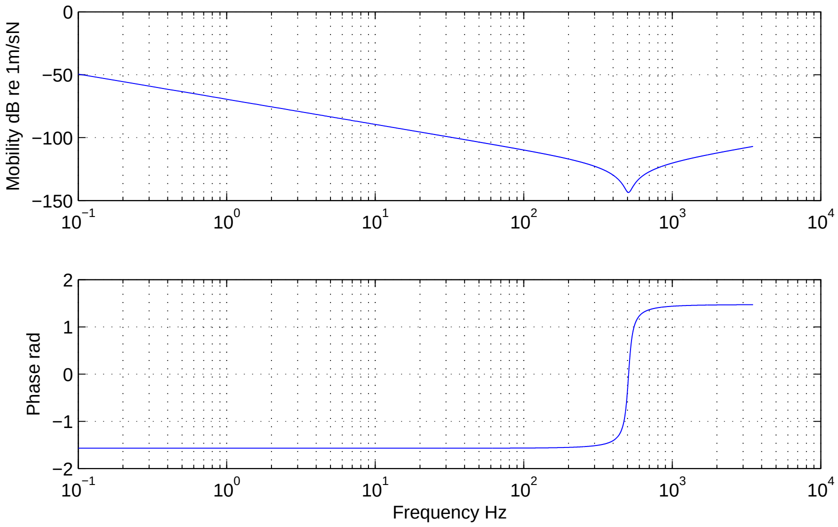

Figure 3.29: Wheel mobility with mass-spring model

is not suitable anymore because of a series of strong resonance peaks which are the radial modes of the wheel.

Contact spring mobility

As for the wheel the relative velocity across the contact spring can be found as

$$v_c = Y_c F \tag{3.21}$$

Where Y_c is the mobility of the contact spring. The vertical mobility of the contact spring can be seen as

$$Y_c = \frac{j\omega}{K_H} \tag{3.22}$$

Where K_H is the linearized Hertzian contact stiffness, [10]. The contact stiffness at the wheel rail contact is caused by the local elastic deformation that generates a contact area, this area increases at the increase of the axial load. If the wheel has a radii R_w in the rolling direction and R_{wt} in the orthogonal direction, and the rail has a radii R_r in the rolling direction and R_{rt} in the orthogonal direction the contact area will be an ellipse with semi-axis a in the rolling direction and b in the transverse direction given by

$$a = \sigma_1 \sqrt[3]{\frac{3F_0 R_0}{2E'}} \tag{3.23a}$$

$$b = \sigma_2 \sqrt[3]{\frac{3F_0 R_0}{2E'}} \tag{3.23b}$$

Where F_0 is the normal load, $E' = E/(1-\nu^2)$ is the plane strain elastic modulus and R_0 is an effective radius given by

$$\frac{1}{R_0} = \frac{1}{2}\left(\frac{1}{R_w} + \frac{1}{R_w t} + \frac{1}{R_r} + \frac{1}{R_r t}\right) \tag{3.24}$$

While the constant σ_1 and σ_2 have to be integrated numerically and can be found on tables as function of $g = a/b$. The approach of the two bodies due to the load F_0 is given by

$$u_0 = \frac{\xi}{2R_0} \sqrt[3]{\frac{3F_0 R_0}{2E'}} \tag{3.25}$$

Where also ξ can be found on table as a function of g.

Although the relation between the approach distance and the load is non-linear, this expression can be linearized for small displacement amplitudes. Thus the incremental contact stiffness can be found as

$$\frac{1}{K_H} = \frac{\xi}{2} \sqrt[3]{\frac{2}{3E'^2 F_0 R_0}} \tag{3.26}$$

For this case a factor $g = 2$ has been chosen and from the tables can be found that $\sigma_1 = 1.4536$, $\sigma_2 = 0.7285$ and $\xi/2 = 0.9436$. With these values the mobility of the contact spring shown in fig. 3.30 is found.

Rail roughness

At first the contact force per unit of roughness, so considering the roughness $r = 1$ m in equation (3.14), can be inspected, see fig. 3.31.

In order to report this to a comparable level with the forces obtained with the simulation in the time domain the roughness has to be taken into account. For this case a standard rail roughness has been generated by a software developed at the Politecnico di Milano that takes as input the range of frequencies of interest and converts it into a roughness profile using the

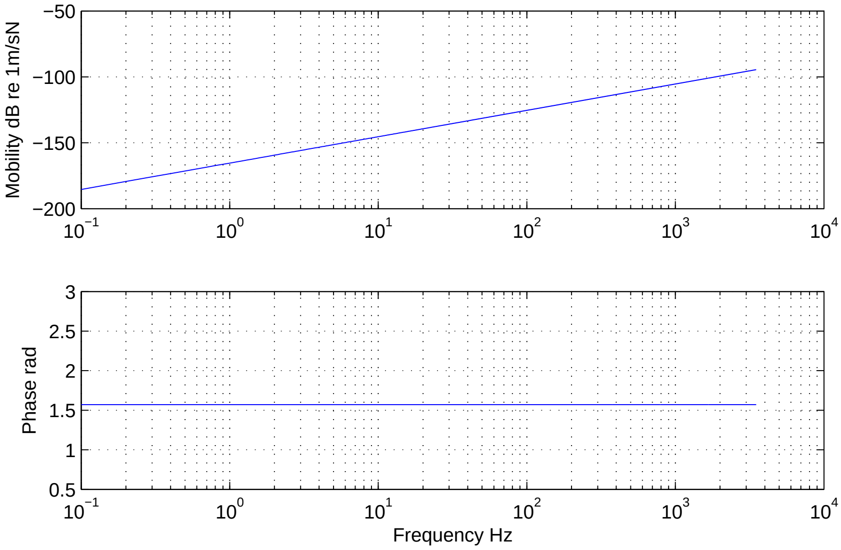

Figure 3.30: Contact spring mobility model

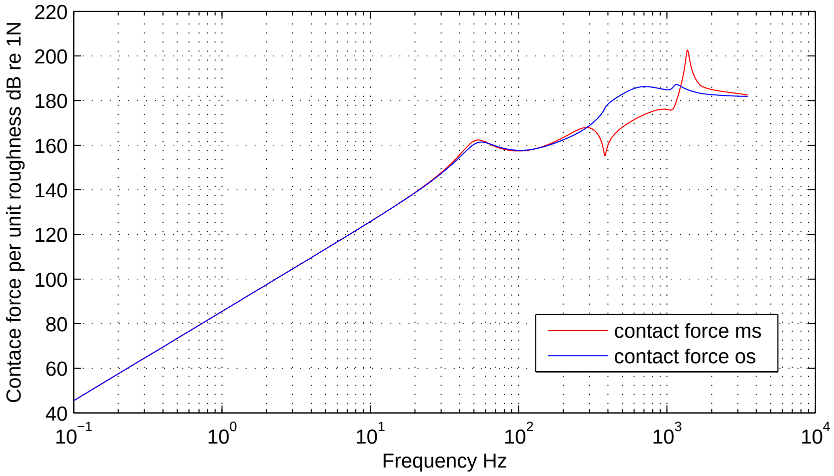

Figure 3.31: Analytical contact force per unit of roughness

ORE standards, [37].

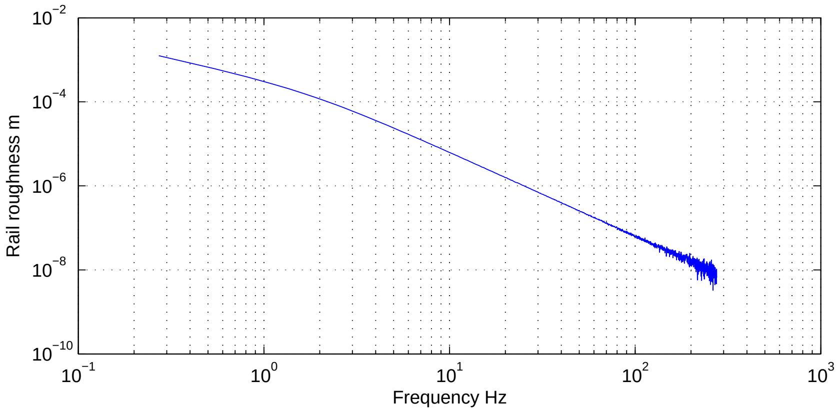

Figure 3.32: Rail roughness spectrum

Fig. 3.32 shows the spectrum of the rail roughness used. It can be seen that the spectrum is truncated for wavelength shorter than 4 cm, this because for a train that travels at 13.9 m/s with a wavelength of 4 cm a frequency of about 350 Hz is obtained and it is already outside of the range of frequencies that interest the ground-borne noise. It can also be seen that for grater wavelengths a higher level of roughness is given rather than for smaller wavelength, this according to the ORE standards. The spectrum of the roughness can also be seen in third octave bands as shown in fig. 3.33.

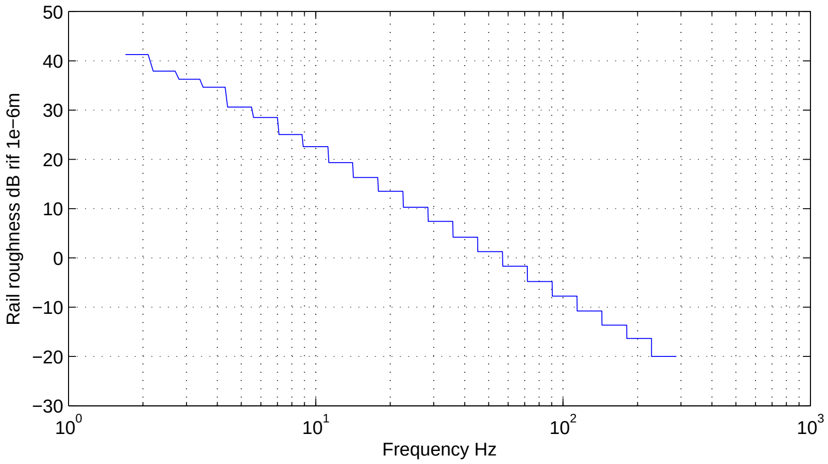

Figure 3.33: Rail roughness spectrum in third octave bands

Wheel roughness

Since in real cases also the wheels are not perfect circles a roughness to the wheel has been given. Also for this case a software developed a the Politecnico di Milano has been used in order to generate a roughness with the harmonic content desired.

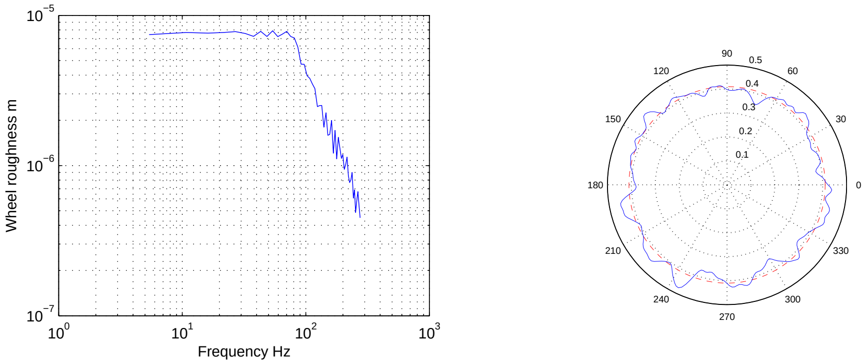

Figure 3.34: Wheel roughness spectrum and reconstruction with amplification 10^3

Fig. 3.34 shows the spectrum of the wheel roughness and its reconstruction with an amplification of 10^3 to make it visible. It can be seen that the spectrum for this case is truncated for the same reason reported in Section 3.2.1.

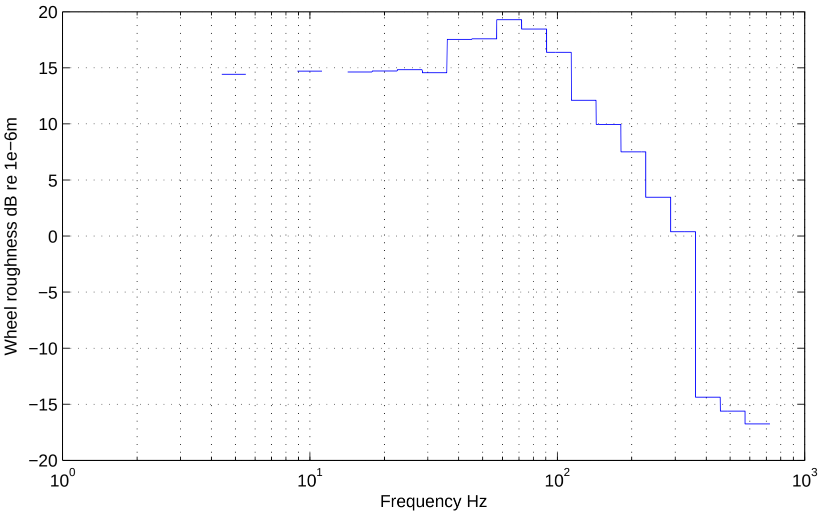

Figure 3.35: Wheel roughness spectrum in third octave bands

Fig. 3.35 shows the spectrum of the wheel in third octave bands.

In order to be used in equation (3.14) the roughness of the wheel and the rail have to be added together this gives the total spectrum showed in fig. 3.36

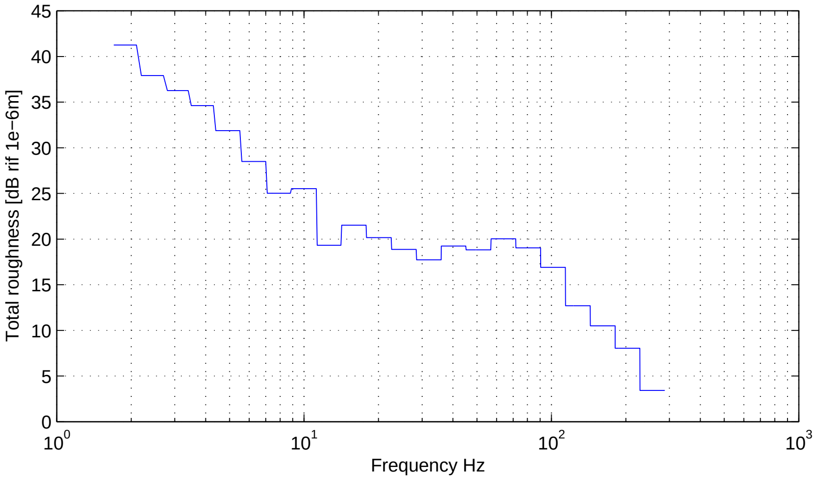

Figure 3.36: Total rail wheel roughness spectrum in third octave bands

Once obtained the spectrum of the total roughness it can be added to the spectrum of the analytical contact force per unite of roughness. To do so both force and roughness must be divided in third octave bands. This will give the analytical contact force that is obtained with the rail mobility, wheel mobility and roughness considered. Fig. 3.37 shows the contact force after adding the wheel rail roughness.

It can be noticed, by looking at fig. 3.37, that with the analytical model the contact forces for the case with and without the tunnel are very close. This is due because the only parameter that changes between the two results is the receptance of the rail with and without the tunnel. As seen previously there is not a relevant difference between them so also the analytical contact forces do not show a significant difference.

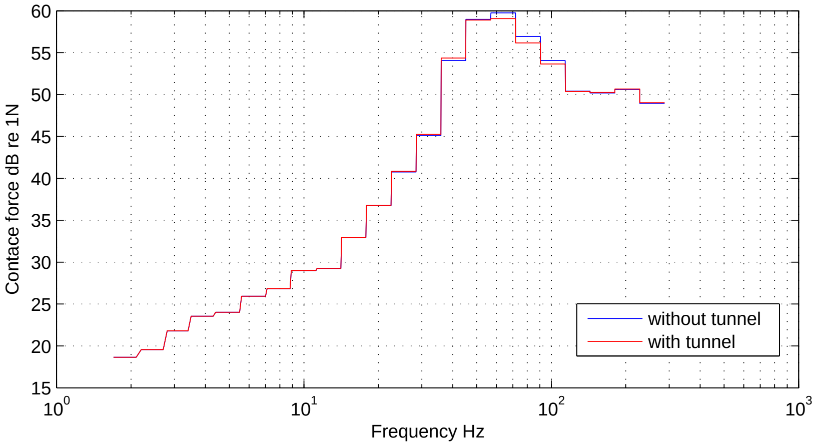

Figure 3.37: Analytical contact force with roughness

3.2.2 Track

The first result shown from the time domain integration is the pass-by of the train on the track alone. This gives a first result of the contact forces. This case is also the one with the lowest computational time because of the low number of nodes of the FE structure. For this case the model of the train used is a three car train with two driving cars and one trailer car.

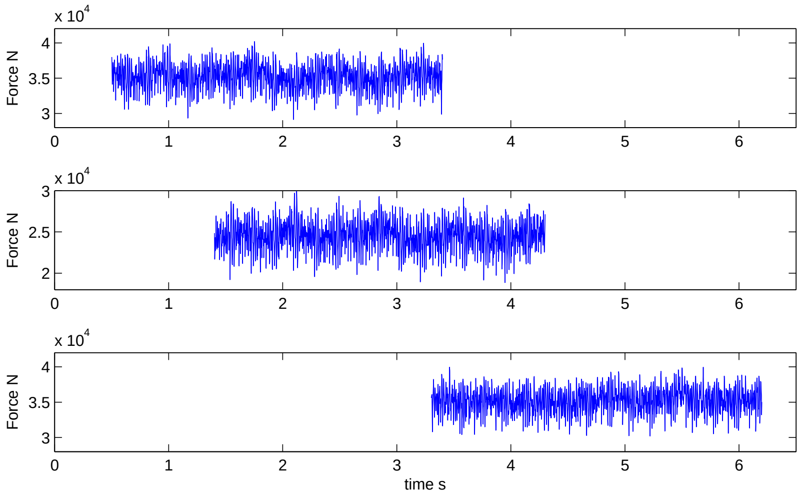

Figure 3.38: Time histories of wheel/rail contact force for the FE model of track only

Fig. 3.38 shows the time histories of the forces of the first wheelset of each car. The time histories are truncated because the length of the FE model of the rail is shorter than the time simulated of the passage of the train. The time histories of the forces when the wheelsets are outside the rail do not have to be taken into account because it is like the wheel is running on a rigid ground so the contact forces are not the real ones. At first it can be seen that the three contact forces have different levels due to the different axial load, because the trailer car is lighter. The vibration of the force around its mean value is due to the irregularity of the wheel and of the irregularity of the rail.

In order to inspect the spectrum of the force the Fourier transform of the time histories has to be performed.

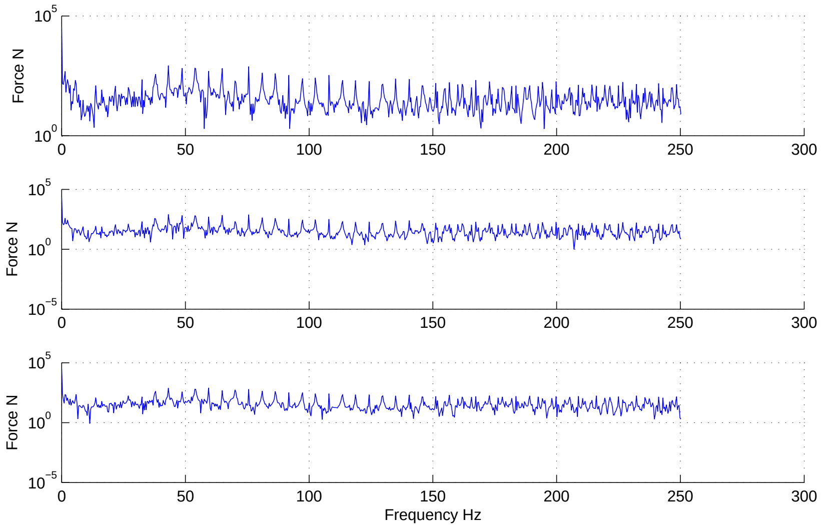

Figure 3.39: Spectrum of the contact forces for the FE model of track only

Fig. 3.39 shows the frequency content of the contact forces. The maximum frequency depends on the time step integration which is kept as large as possible in order to reduce the computational time. The maximum frequency of 250 Hz is enough to describe the ground-borne vibration. It can be seen that the spectrum of the force is almost a constant due to the random nature of the irregularity of wheel and rail. It can also be seen that there are peaks with a periodicity of about 5 Hz, this is due to the wheel roughness which is dependent on the wheel circumference. Also the spectrum in third octave bands can be obtained.

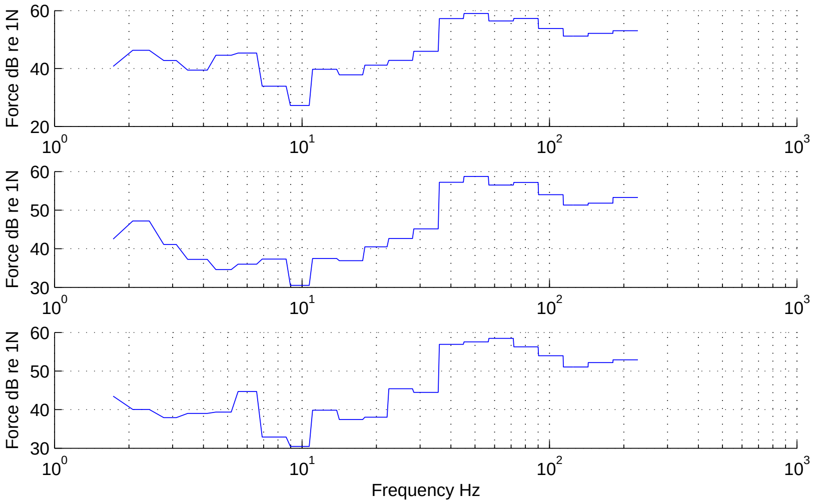

Figure 3.40: Third octave band spectrum of the contact forces for the FE model of track only

Fig. 3.40 shows the third octave band spectrum of the contact forces due to the pass-by of the train. Firstly it can be noticed that the levels, in this case, are not too different for the three different cars. It can be seen that at very low frequencies, below 10 Hz, the response starts high and than it lowers. This is probably due to the vehicle dynamics but this range is outside the range of interest for the ground-borne noise. At higher frequencies it rises again due to the wheel/rail interaction. These forces can be compared to the one obtained with the analytical solution for the rail only.

Fig. 3.41 shows the comparison between the analytical and numerical contact force. It can be noticed that at low frequencies there is a big difference between the two methods. This is most likely due to the vehicle dynamics which is not taken into account in the analytical model of the contact force. While at higher frequencies there is good agreement between the response of the numerical model and the response of the analytical model.

Also the forces from underneath the sleeper can be considered, in this case, these are the forces exchanged between the rail and the rigid ground.

Fig. 3.42 shows the time history of the force exchanged between the rail and the rigid ground. A series of peaks can be observed. These occur when the wheelsets travel over the position of the sleeper. The negative sign is due to the sign convention taken for the Z axis. This time history can be

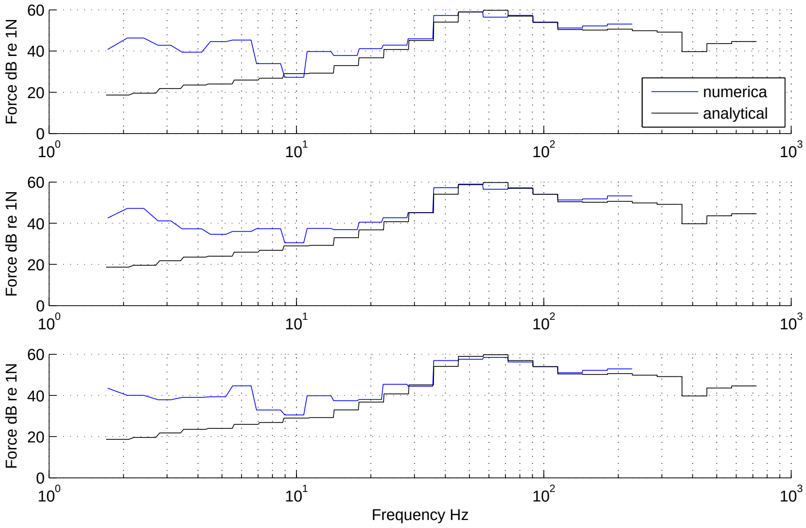

Figure 3.41: Third octave band spectrum of the contact forces from the FE model and the analytical model for track only

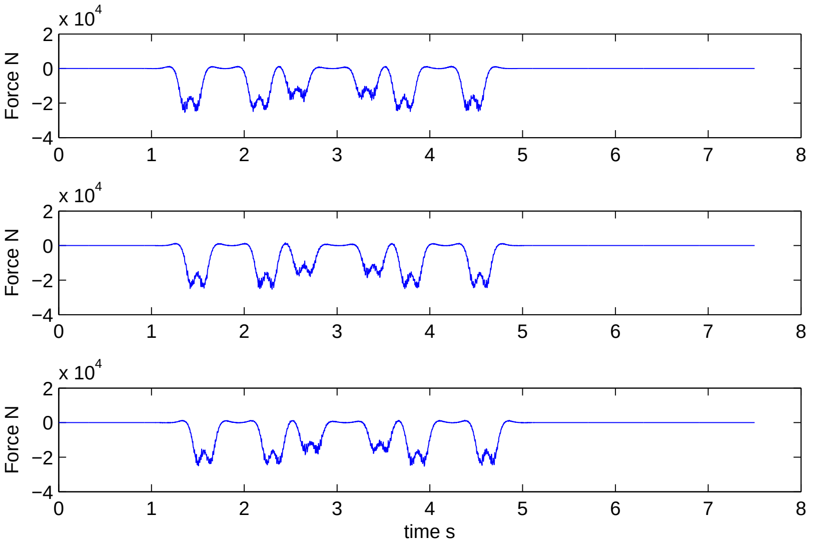

Figure 3.42: Time history of the force underneath one sleeper for the FE model of track only

extracted form every sleeper and it is not necessarily always the same, first, because of the random nature of the roughness and, second, because there might be an irregularity as will be show further on. Also for this case the spectrum of the force can be inspected.

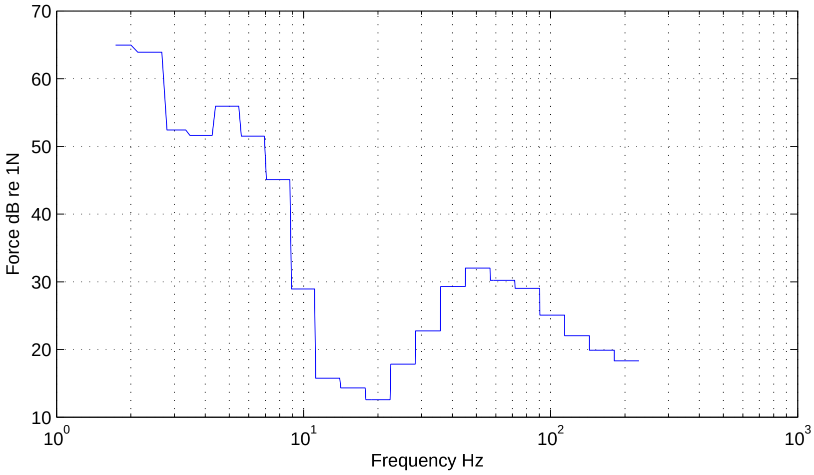

Figure 3.43: Third octave band spectrum of the force underneath the sleeper for the FE model of track only

Fig. 3.43 shows the third octave band spectrum of the force transmitted to the rigid ground. It can be noticed that at low frequencies the response is high while at higher frequencies the response is attenuated compared to the one seen before. This is due to the nature of system that can be simplified as a low-pass filter. This means that at low frequencies the response is almost unchanged than after the cutoff frequency the response is attenuated. For this case as a first approximation the cutoff frequency is around 5.5 Hz.

3.2.3 Tunnel

Here will be shown the results from the time domain integration of the pass-by of the train with the FE model of the track and tunnel. For this simulation the model of the train is a three cars one, like the train used in the previous Section. Also from this case the time histories of the contact forces can be extracted.

Fig. 3.44 shows the time histories of the wheel/rail contact forces for the three cars. Also in this case the time histories are truncated due to the length of the rail considered. Like before also for this case can be analyzed

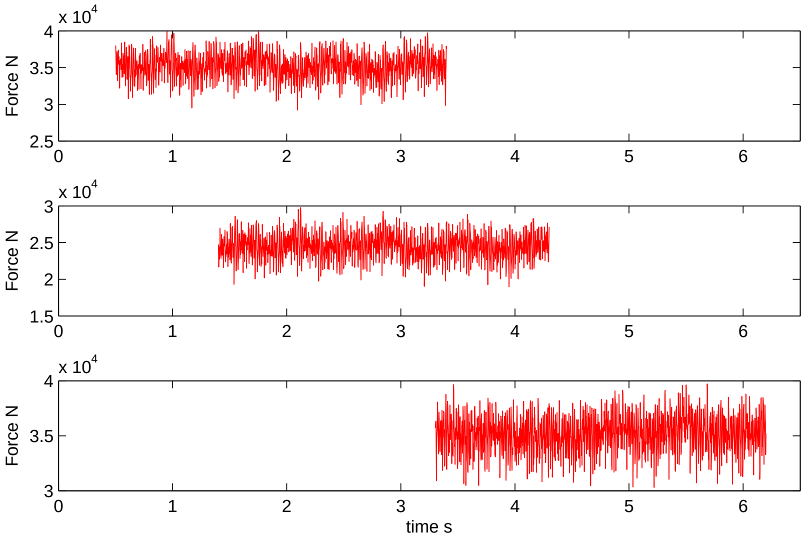

Figure 3.44: Time histories of wheel/rail contact force for the FE model of track and tunnel

the spectrum of the forces.

Fig. 3.45 shows the brad band spectrum of the contact forces due to the wheel/rail interaction for the case of the track coupled with the tunnel. Also for this case can be observed that the spectrum is almost flat random nature of the roughness that is able to excite many different frequencies, and several picks due to the wheel periodicity. Like before it is worth to look at the spectrum in third octave bands to better understand the frequency content of the forces for this case.

Fig. 3.46 shows the spectrum of the force in third octave bands. Like before also for this case the third octave bands shows that at low frequencies the spectrum starts high and lowers up to 10 Hz still due to the vehicle dynamics. Than at higher frequencies it rises again due to the interaction of the wheel with the track. It is worth to compare these results the the results from the analytical model that considers also the tunnel.

Fig. 3.47 shows the comparison between the analytical and numerical contact force obtain with the FE model of the track coupled with the tunnel. It can be seen that at low frequency there is a difference due to the vehicle dynamics while at higher frequencies, above 10 Hz, a good agreement is found between the analytical and numerical results.

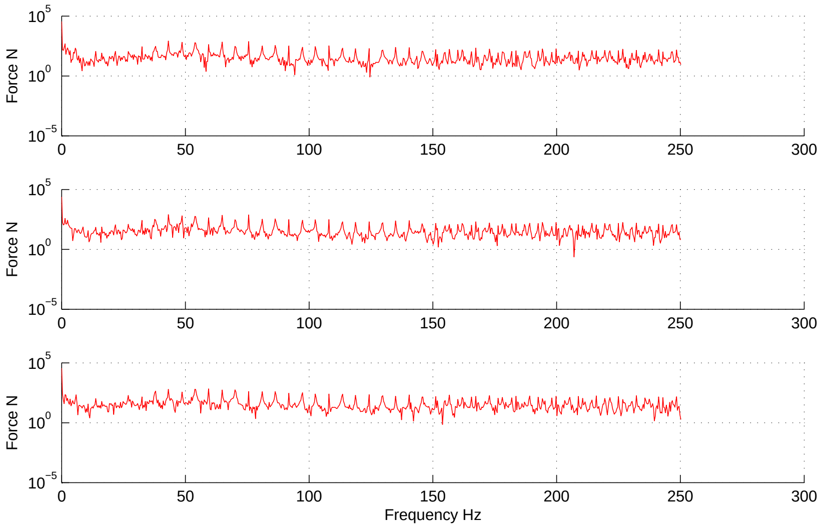

Figure 3.45: Spectrum of the contact forces for the FE model of track and tunnel

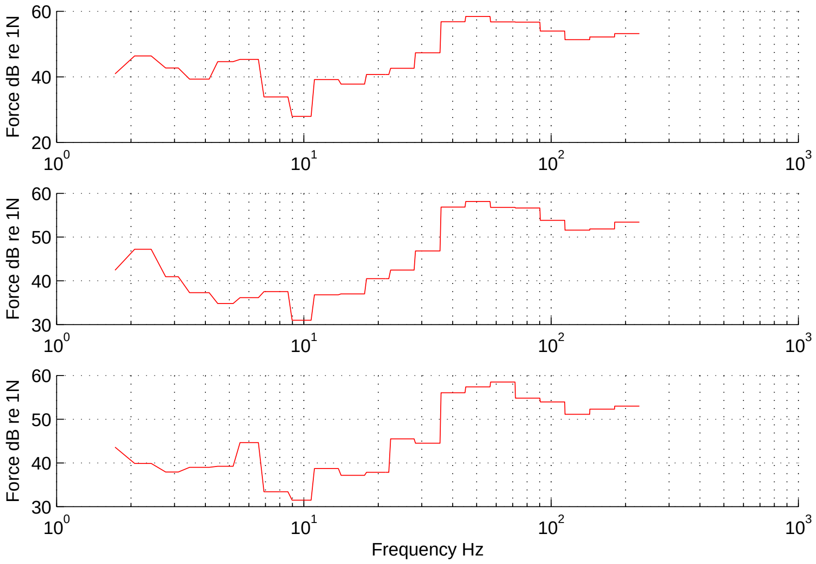

Figure 3.46: Third octave band spectrum of the contact forces for the FE model of track and tunnel

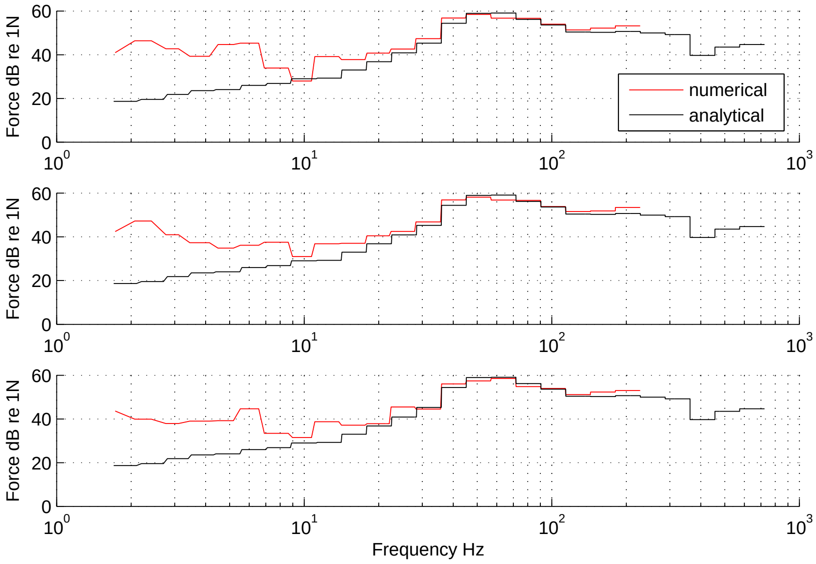

Figure 3.47: Third octave band spectrum of the contact forces from the FE model and analytical for track and tunnel

Also for this case of study the forces transfered from the rail to the ground, or in this case the deformable tunnel invert, can be extracted.

Fig. 3.48 shows the time history of the force transfered from the rail to the tunnel invert. The shape and the levels are similar to the ones of the previous case. The third octave band of the spectra of these forces can be inspected too.

Fig. 3.49 show the third octave band spectra of the forces exchanged between the rail and the tunnel invert. The same considerations made for the previous case of study can be made also for this one.

3.2.4 Joint irregularity

Now will be presented the results of the integration in the time domain of the FE model with the joint irregularity applied to the rail. For this simulation the model of the tunnel is shorter to reduce the integrational time.

Fig. 3.50 shows the time history of the contact force for this case of study. It can be seen that the time history is different from the ones shown previously because of the peak that represents the passage of the wheelset over the irregularity. The shape of this peak can be understood intuitively:

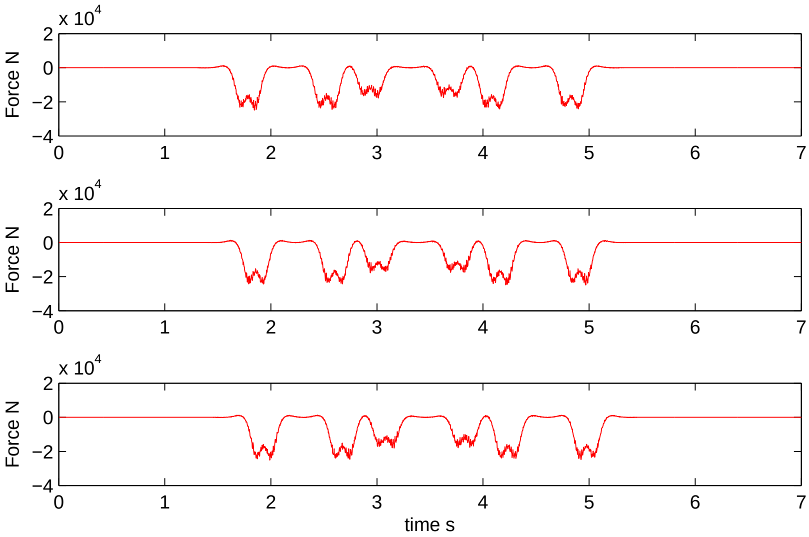

Figure 3.48: Time history of the force underneath one sleeper for the FE model of track and tunnel

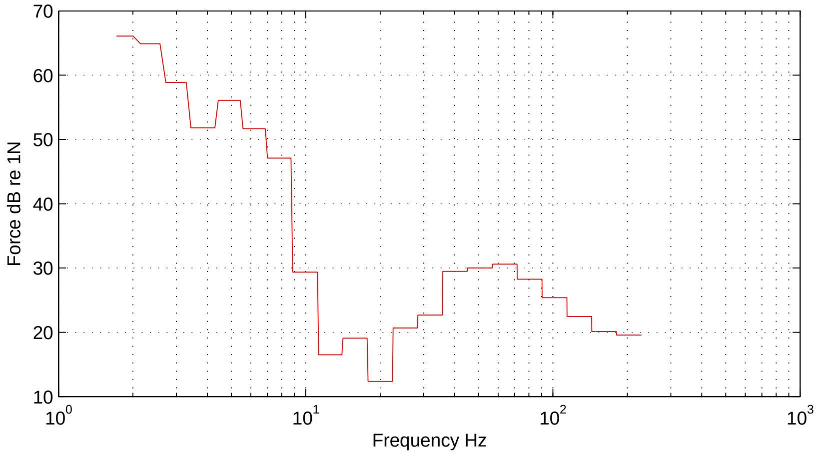

Figure 3.49: Third octave band spectra of the force underneath the sleeper for the FE model of track and tunnel

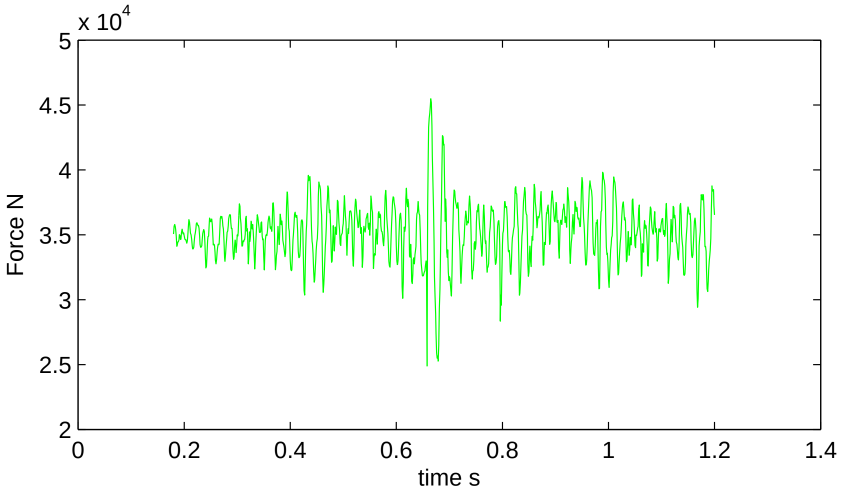

Figure 3.50: Time history of wheel/rail contact force for the FE model with track tunnel and joint

first, while the wheel is approaching the joint, the left rail bends more than the right one because of the disconnection; when the wheel reaches the joint it falls into the gap and hits the step due to the difference in bending and the force rises fast; in the end when the wheel leaves the left rail there is a decrease of the force due probably to the elastic deformation.

Fig. 3.51 shows the third octave band spectra of the forces due to the pass-by of the train over the joint. This can not be compared to an analytical case due to the complexity of the problem, but it will be compared with the model without the joint in order to see if there is a difference between the two.

Again the forces from underneath the sleeper can be shown and analyzed.

Fig. 3.52 shows the time history of the force underneath a sleeper due to the pass-by of the train. Since the joint has been placed at midspan of a certain position each sleeper sees a difference force. Also the spectra of the force can be observed

Fig. 3.53 shows the third octave band spectra of the force underneath the sleeper. This time the shape is different from the previous cases because of the presence of the irregularity. The same consideration made for the first case of study can be made also for this one.

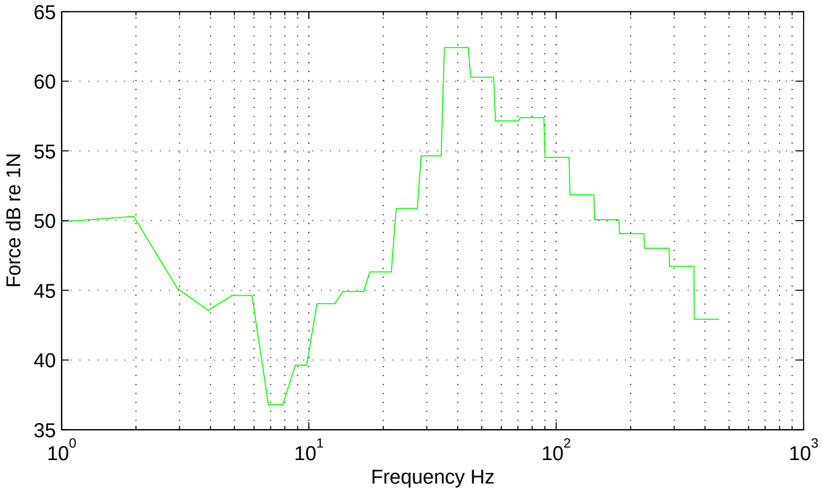

Figure 3.51: Third octave band spectra of the contact force from the FE model with track tunnel and joint

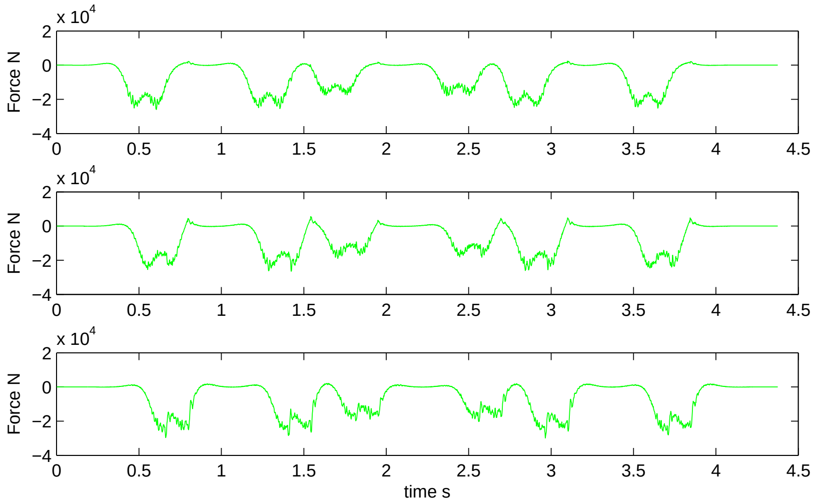

Figure 3.52: Time history of the force from underneath the sleeper from the FE model with the track tunnel and joint

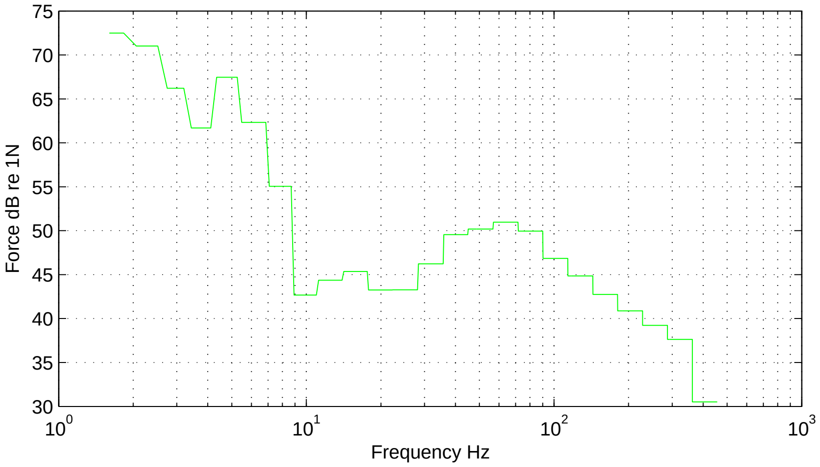

Figure 3.53: Third octave band spectra of the force underneath the sleeper from the FE model with track tunnel and joint

3.2.5 Comparison of the results

It is possible to compare the forces obtained with the different models in order to investigate the influence of the different configuration on the forces exchanged between the wheel and the track and between the track and the ground. This is possible olso because the train used has always the same parameters.

At first the contact force obtained with the models of the rail with and without the tunnel can be inspected.

Fig. 3.54 reports the two time histories of the contact force. It can be noticed that the two time histories are very similar due to the similarities of the receptances of the rail with and without the tunnel. From the time history of the force it is hard to identify the difference in the forces so at this purpose it is more useful to look at the third octave band spectra.

Fig. 3.55 shows the third octave band spectra of the contact forces obtained with the two different models. Also from here it is possible to see that the two spectra of the forces are very similar. This gives good agreement with what found from the simplified analytical model. It is interesting to notice that this way a simplified analytical model could give, as first approximation, a good esteem of the contact force for a train running in a strait line. This result could be used for example to conduct a parametric analysis of the influence of the different parameter, for example the roughness levels,

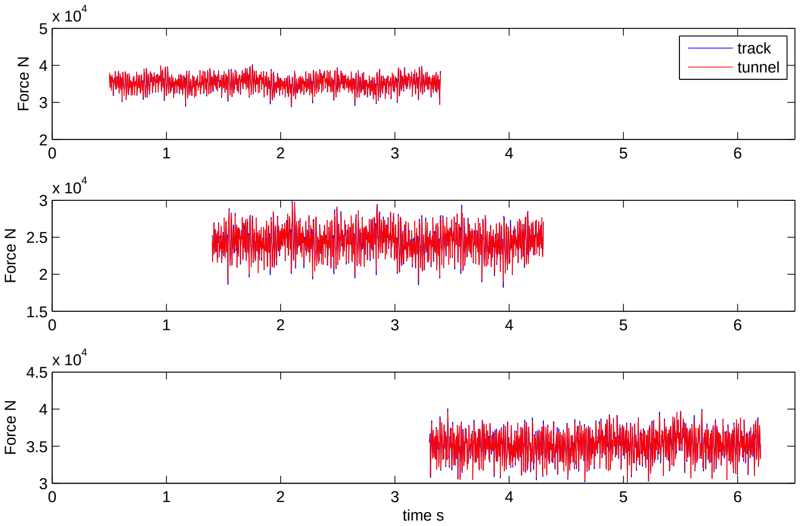

Figure 3.54: Time history of the contact forces for the track and tunnel models

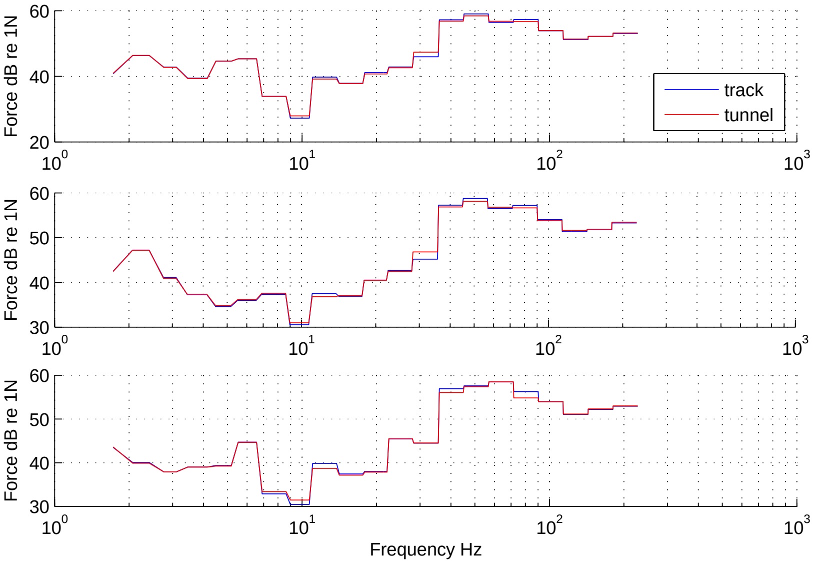

Figure 3.55: Third octave band spectra of the contact force of the track and tunnel models

on the contact force.

The analytical model can not although model the non linearities of the springs or of the dampers so it is valid only for very simple configurations like the train running on a straight line with all the elements considered linear. However for those simple case it gives good results in a very short time.

Also the forces exchanged between the track and the ground can be inspected

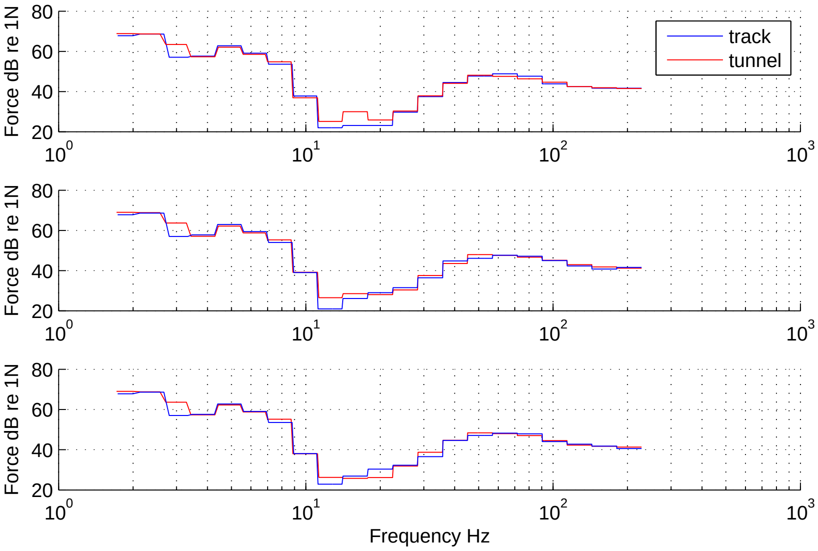

Figure 3.56: Third octave band spectra of the forces from underneath the sleepers of the track and tunnel models

Fig. 3.56 show the third octave band spectra of the forces exchanged from the sleepers to the rigid ground or to the tunnel invert. It is possible to notice that the two forces are very similar for all the sleepers presented this is due to the similarities of the contact force.

Furthermore it is possible to investigate the influence of the presence of the joint on the forces exchanged between the train and the track and between the sleepers and the tunnel invert.

Fig. 3.57 shows the third octave band spectra of the contact force of the tunnel model compared with the contact force of the joint model for only the first wheelset. It is possible to notice that the two spectra are very different. Due to the presence of the joint its spectra is quite higher than the spectra

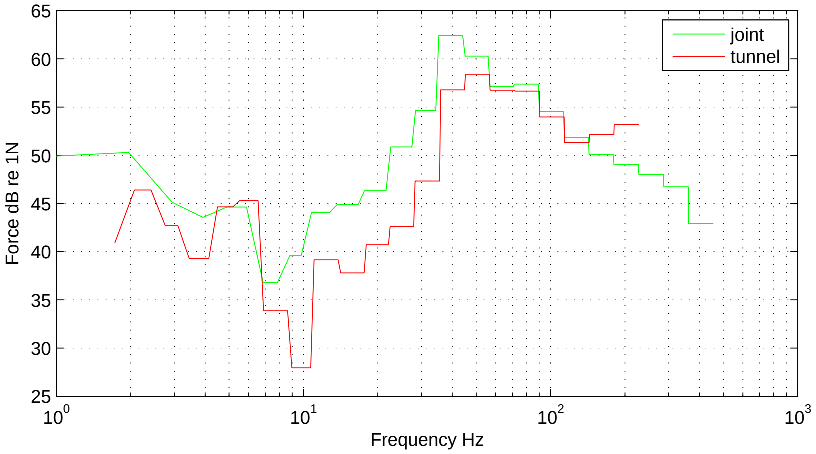

Figure 3.57: Third octave band spectra of the contact force of the tunnel and joint models

of the rail without the joint so it introduces more energy in the system. Also the forces from underneath the sleepers can be compared to see if the joint introduces more energy also in the ground.

Fig. 3.58 shows the third octave band spectra of the forces exchanged with the tunnel invert in the of the two cases studied. It can be noticed that further from the position of the joint the force exchanged is similar to the other case but closer to the position of the joint the difference increases.

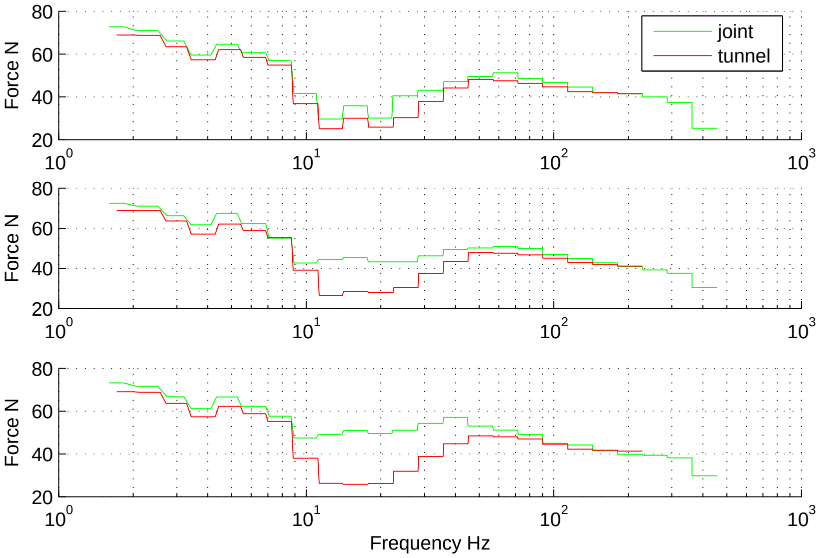

Figure 3.58: Third octave band spectra of the forces from underneath the sleepers of the tunnel and joint models

Chapter 4

Wave frequency domain model

This Chapter presents in detail the inputs for the frequency-wavenumber domain model WANDS, and its outputs.

Section 4.1 describes the different FE-BE structures of the ground used as inputs for WANDS studied in this thesis. Three different models have been prepared to investigate the response of the ground under different parameters:

- A simple halfspace
- A two layered ground
- A deep bored underground tunnel

Section 4.2 presents the result from the frequency-wavenumber domain integration of the ground model in terms of dispersion curves and of ground transfer functions. Different simulation with different parameters as input have been tested to investigate the sensitivity of the ground response:

- Wavenumber resolution and range
- The length of the boundary elements
- The traction vector, which is a pressure applied to the boundary element
- Different types of ground

4.1 Inputs for WANDS

This Section presents the models of the ground used as input for the frequency wavenumber domain program WANDS.

Since the hybrid modelling can be used for any configuration of forces and grounds at first Section 4.1.1 presents a simple case of just an halfspace ground. This has been used to better understand the problem and the outputs of WANDS. This case can be easily compare with the results from an analytical model.

Section 4.1.2 presents the model of a two layered ground, like the one found in [24] and of which the parameters are reported in table 4.1. This will be used as input for WANDS in order to determine the ground transfer functions to reproduce the case of study presented in [24].

		Upper layer	Halfspace
P-wave speed	m/s	240	700
S-wave speed	m/s	120	350
Density	kg/m^3	1800	2000
Young's modulus	MPa	69.12	653.3
Shear modulus	MPa	25.92	245.0
Poisson's ratio		0.333	0.333
Loss factor		0.1	0.1
Layer depth	m	3.0	∞

Table 4.1: Ground properties for the example considered

The last Section 4.1.3 shows the model of the underground tunnel presented in [26] embedded in the ground. This will be used in order to obtain the transfer functions of the ground to reproduce the CONVURT environment.

4.1.1 Halfspace

This is the simplest case of study since with the use of the boundary elements method the halfspace can be discretized just like a line.

Fig. 4.1 shows a simple drawing of a single layer halfspace which has been model with the BE. In order to investigate the effects of the different parameters different models have been prepared. The parameters that can influence the response are:

- the the length of the boundary element

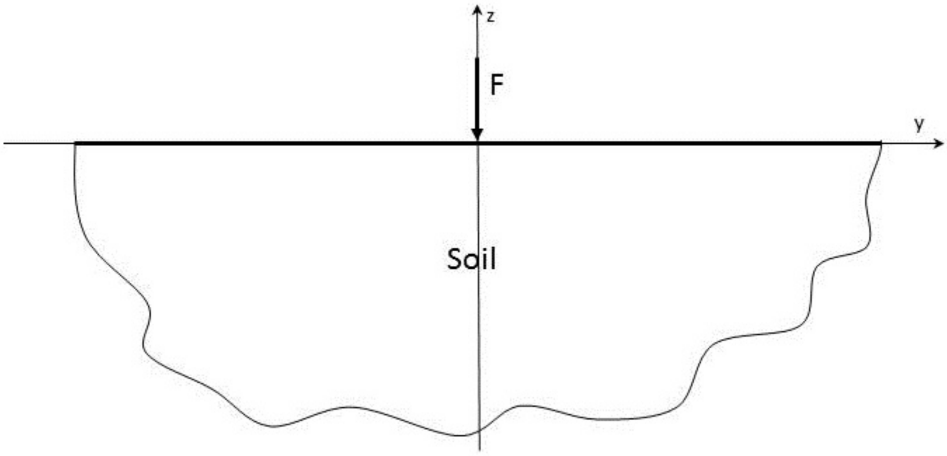

Figure 4.1: Drawing of a single layer halfspace

- the wavenumber range and the wavenumber discretization
- the force given as input

Since on the boundary element is not permitted to apply a point force the force must be applied as a boundary condition. The traction vector is then the variable to look at. The determination of the input force plays an important role in the identification of the transfer function because, since the whole ground model is linear, it determines the magnitude of the transfer functions. The traction vector is defined as pressure and it changes with the size of the boundary element.

Three types of soil have been investigated: the first has the characteristics of the upper layer presented in table 4.1; the second has the characteristics of the halfspace presented in table 4.1; and the third is a completely different ground with characteristics shown in table 4.2

P-wave speed	m/s	1470
S-wave speed	m/s	250
ρ	kg/m^3	1945
E	Pa	$361.1\ 10^6$
ν		0.485
loss factor		0.1

Table 4.2: Parameters of the Horstwalde ground

In order to investigate the influence of the parameters, for the first ground type, have been prepared different cases. The length of he boundary element has been changed from 2 m to 0.2 m, the wavenumber range has been changed from ±6 rad/m to ±30 rad/m and the wavenumber discretization from 128 points to 1024.

4.1.2 Two layers ground

The previous model can be extended in order to represent a two layered ground. This model is made to represent the ground used in [24]. It has a soft top layer and a stiffer halfspace with the characteristics presented in table 4.1.

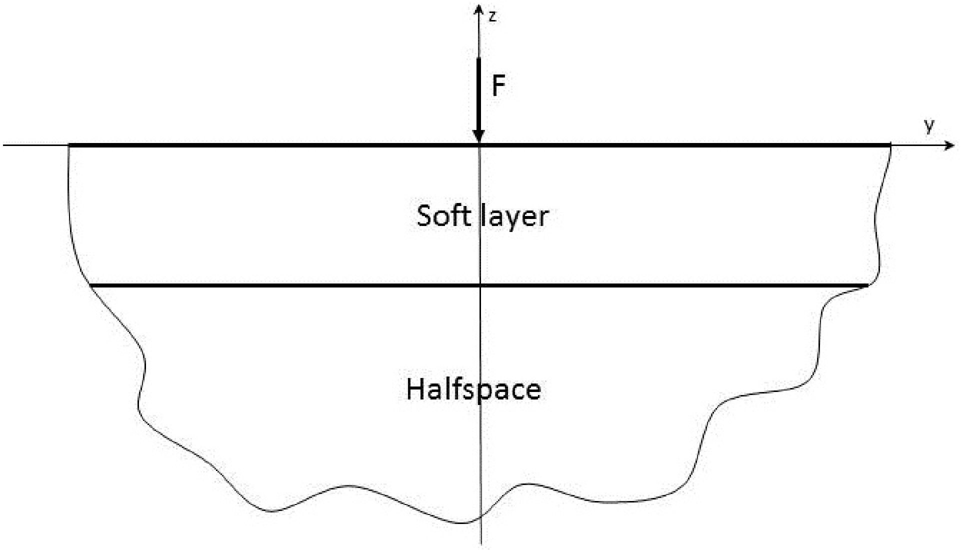

Figure 4.2: Drawing of a two layers ground

Fig. 4.2 shows a drawing of a two layers ground where the two interfaces have been modelled with the BE method.

4.1.3 Underground tunnel

This model represents the underground tunnel presented in [26]. The tunnel is 28 m below the surface and it has been model with the FE method while the ground around it has been modelled with the BE method.

Fig. 4.3 shows the drawing of the FE model of the tunnel coupled with the ground. The specification for the characteristics of the ground and of the tunnel are the same as the one presented in Chapter 3. The element size

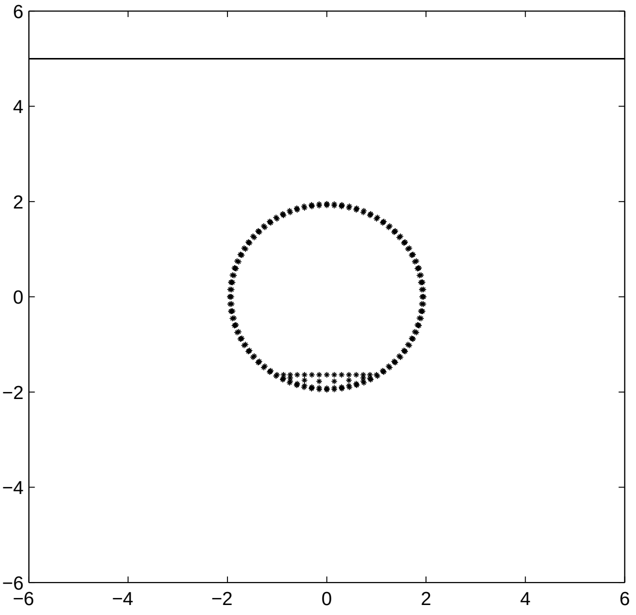

Figure 4.3: Drwaing of the FE model of the tunnel and of the ground, the soil surface has been lowered only to make the image easier to see

has been chosen in order to be able to represent the slowest wave that could be present in the ground. Since the slowest wave that could be present is the shear wave in the softer upper space, which has not been modelled here to keep the computational time lower. The maximum element size depends on the relation

$$\lambda_{min} = \frac{c_{min}}{3f_{max}} \tag{4.1}$$

where λ_{min} is the shortest wave that can be seen without errors, c_{min} is the speed of the slowest wave, f_{max} the highest frequency of interest and the 3 is used to avoid the aliasing effect, [32].

4.2 Results from the frequency-wavenumber domain integration

This Section presents the results from the frequency-wavenumber domain calculation of the models presented in Section 4.1.

Section 4.2.1 shows the results for the tests run on different halfspace grounds used to investigate the influence of the parameters, chosen as input for the simulation, on the outputs. The parameters investigated are the wavenumber range and resolution, the boundary element size, the traction vector, which represents the pressure given as input to the forced response and the ground parameters. A comparison with an analytical multi layers model will be made in order to understand if WANDS returns consistent results.

Section 4.2.2 shows the results for the two layered ground. This case is similar to the previous one, but this time, on the response there is the contribution of both grounds due to the reflected waves. Also for this case a comparison with the analytical model can be obtained to verify the consistency of the results

Section 4.2.3 shows the results for the underground tunnel model. For this case the main difference is that there is a FE structure coupled with the BE structure of the ground and that the force is applied on the FE structure instead that on the BE like in the previous cases. For this case a comparison with an analytical model is not possible due to the complexity of the problem.

4.2.1 Halfspace

Here will be presented the results of the numerical calculation of the simple halfspace model presented in Section 4.1.1. The results obtained by the numerical calculation are the transfer function of the ground and the dispersion curves.

As said before different models have been prepared to investigate the influence of the parameters that can be chosen as input. These will be considered one by one in order to understand better the variations due to the changes in the parameters.

Wavenumber resolution

To study the influence of the wavenumber resolution four simulations have been performed. The parameters of the model that remain constant are: the length of the boundary element set to 0.6 m, the wavenumber range set to ±10 rad/m and the traction vector set to 1 N/m. The wavenumber is linearly divided inside its range and the division must be a power of two due to the construction of the fast Fourier transform implemented in WANDS. To this purpose four powers of two have been chosen: $2^7 = 128$, $2^8 = 256$, $2^9 = 512$ and $2^{10} = 1024$.

At first the forced responses of the ground in the frequency wavenumber domain, that approximate the dispersion curves of the ground, are presented. From these it is possible to identify the cut on frequencies of the waves that propagates in the ground, to identify the slowest wave and its speed this is possible by finding the slope of the curve. This can be easily found from

$$c = \lambda f \tag{4.2}$$

where c is the wave speed, λ its wavelength and f the frequency. If the expression for the wavenumber is substituted $\lambda = 2\pi/k$ it can be found that $f = \frac{c}{2\pi}k$ so by finding two points of the curve the speed of the wave can be determined.

Fig. 4.4 shows the four ground responses in the frequency wavenumber domain that approximate the dispersion curves in the vertical, Z, direction obtained with this case of study. A logarithmic discretization of the frequencies has been used in order to reduce the computational time. From fig. 4.4 can be evaluated the wave speed as shown, and it gives a result of

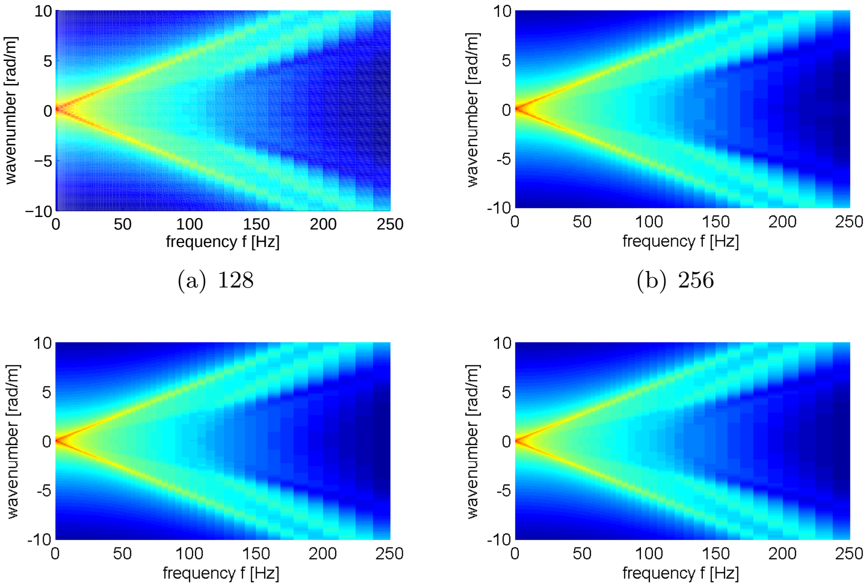

(a) 128 (b) 256

(c) 512 (d) 1024

Figure 4.4: Dispersion curves of the halfspace for different wavenumber discretization

$c = 120\ m/s$, and it can be seen that increasing the discretization number gives a better resolution in the wavenumbers, giving more details, but the dispersion curves do not change.

The increase of wavenumber resolution gives also, as a consequence, that a larger portion of space can be reproduced. The space domain is rebuilt applying the inverse Fourier transform at the wavenumber domain so the maximum distance in space depends on the inverse of the wavenumber resolution, $x = 2\pi/\delta k$, .

Now the response of the ground can be inspected. In order to do so four reference distances from the point at which the force is applied have been taken: 0 m, 6 m, 12 m and 24 m.

Fig. 4.5 shows the ground transfer functions at different distances from the point of application of the force and for different wavenumber resolutions. As pointed out before a higher wavenumber resolution reconstructs a wider portion of space, this is the reason why for the discretization with 128 points the line at 24 m is missing. The high frequency distortion depends on the wavenumber range and will be discussed later on. Instead, the low frequency noise depends on the wavenumber resolution. It can be noticed

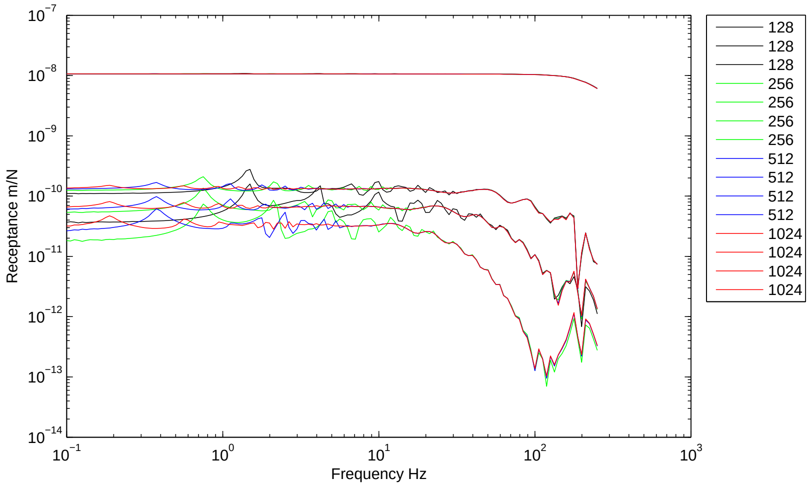

Figure 4.5: Ground transfer functions from 0 m (top line) to 24 m (bottom) for different wavenumber resolution

that for a higher resolution the low frequency noise tends to reduce. This can be understood by looking at the dispersion curves. At very low frequency a low wavenumber resolution is not able to describe everything that happens so by increasing the wavenumber resolution it increase the accuracy of the calculation. The mid frequency range is well described by almost all the wavenumber resolution. It can be noticed that nothing change at the distance 0 because the application of the force drives the displacements.

Wavenumber range

Also to study the influence of the wavenumber range on the frequency responses of the ground four wavenumber range have been investigated: ±6, ±10, ±20 and ±30 rad/m. While the dimension of the boundary element and the traction vector remain the same as the previous case. The wavenumber resolution is hard to keep constant due to the fact that it can be changed only as a power of 2 but it is already been shown that it has an influence only at the low frequencies.

Fig. 4.6 shows the dispersion curves in the vertical direction for the four cases. Widening the wavenumber range is possible to describe a bigger portion of the dispersion curve. Even if it seems like the dispersion curves are changing shape by widening the wavenumber range it is only an effect due to the scaling of the graph; in fact if the wave speed of the slowest

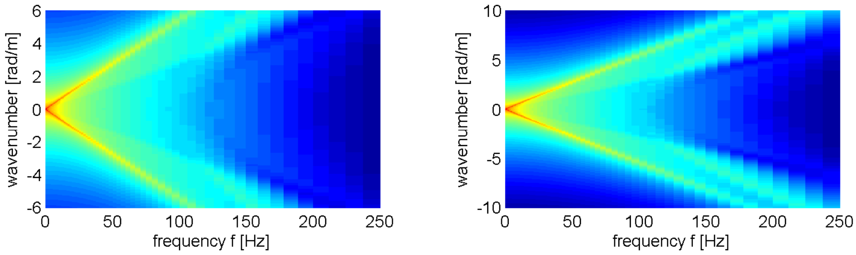

(a) ±6 rad/m (b) ±10 rad/m

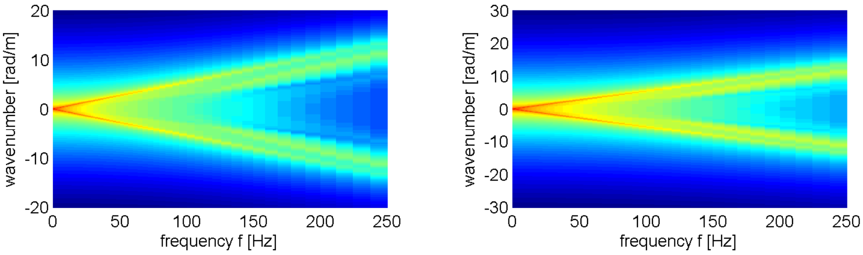

(c) ±20 rad/m (d) ±30 rad/m

Figure 4.6: Dispersion curves of the halfspace for different wavenumber range

wave that propagates is derived from the dispersion curve always the same value of $c = 120\ m/s$ is obtained. A wider wavenumber range gives a higher spatial resolution due to the reconstruction of the spatial coordinates $\delta x = \frac{2\pi}{k_{max}-k_{min}}$. So if the wavenumber discretization is kept with the same number of points and the wavenumber range is increased the wavenumber resolution decreases so the maximum distance reconstructed in the space decreases but the spatial resolution increases.

As shown for the previous case also the receptances obtained can be inspected.

Fig. 4.7 shows the ground transfer functions at different distances from the point of application of the force and for different wavenumber ranges. From fig. 4.7 can be seen that in the far field, the curves at 6, 12 and 24 m have all the same levels and they are very much alike. The low frequency noise is due to the wavenumber resolution as explained before. It can be observed that at high frequency, by widening the wavenumber range, the curves are less noisy this is because of the better description of the dispersion curves. Lets make an example to clarify by considering the two extreme cases of wavenumber range ±6 rad/m and ±30 rad/m and by considering the frequency of 200 Hz. By looking at the dispersion curve of the wavenumber

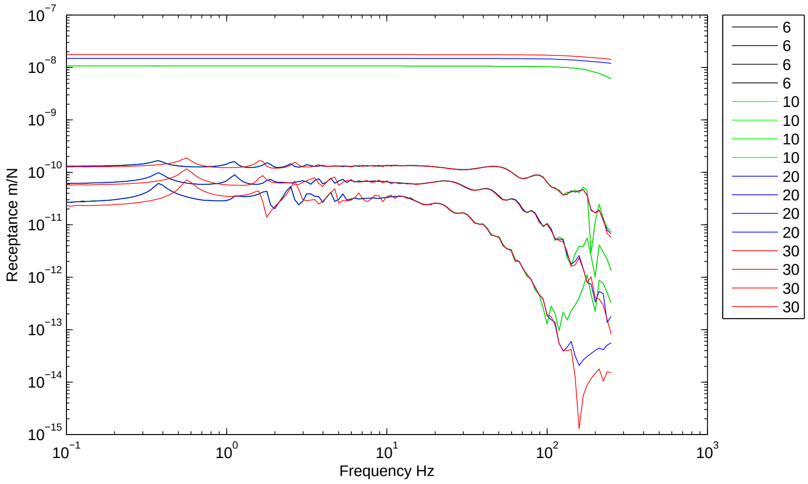

Figure 4.7: Ground transfer functions from 0 m (top line) to 24 m (bottom) for different wavenumber range

range ±6 rad/m it is not able to describe the slowest wave present in the ground, this makes it impossible to reconstruct correctly the response of the ground at a certain point for that frequency. Instead by looking at the dispersion curve of the wavenumber range ±30 it is able to describe well the dynamic response of the ground at the frequency of 200 Hz and so it is able to reconstruct the ground response at a given distance for the 200 Hz frequency.

There is an issue with the responses at 0 m, they tend to increase by widening the wavenumber range. This is due to the reconstruction of the force in the spatial domain. The traction vector is given as a constant in the frequency wavenumber domain so by doing the inverse Fourier transform of the force it would become a Dirac function, but since the force in the frequency wavenumber domain is sampled it gives a discrete Dirac function in the space domain. Since the spatial resolution increases by widening the wavenumber range the traction vector is distributed on a smaller area so the force at the position 0 m is higher even if the integral of the force remains the same. Because in the force in the far field is seen as a point force this mechanism does not affect the responses in the far field while it affects the near field ones. Since the purpose of this thesis is to investigate the far field response of the ground the response at 0 m is not of interest and no farther investigations were made.

BE length and traction vector

Here it is studied the influence of the BE length and the influence of the traction vector on the ground transfer functions. For this purpose four different length have been tested: 0.2 m, 0.6 m, 1 m and 2 m. It is worth to remind that the boundary elements used by WANDS are quadratic elements. At first will be shown the case where the traction vector is constant for all the BE length together with the wavenumber range and resolution. As a second case will be shown the results for different traction vectors for each BE length keeping unchanged the wavenumber range and resolution.

The length of the boundary element affects the maximum wavelength that can be inspected without having the aliasing, [32], this depends on the wave speed and on the maximum frequency of interest.

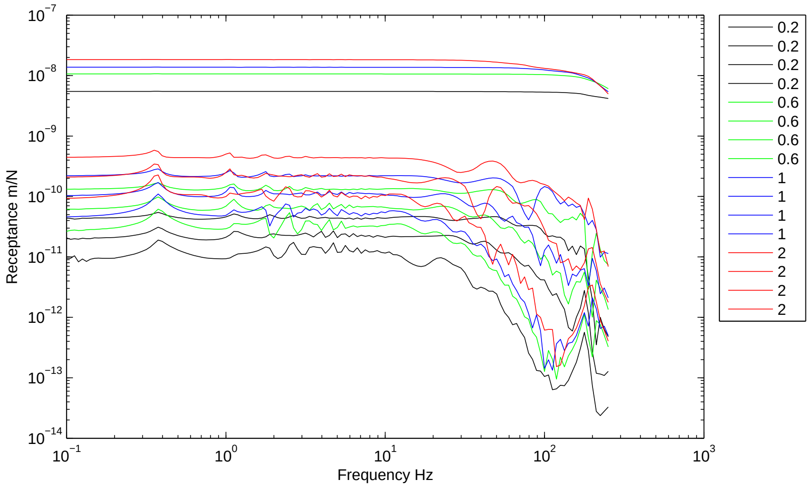

Figure 4.8: Ground transfer functions from 0 m (top line) to 24 m (bottom) for different BE length but same traction vector

Fig. 4.8 shows the ground transfer functions at different distances from the point of application of the force and for different BE sizes. From fig. 4.8 can be seen that there is no agreement between the different simulations. The shapes of the transfer functions at the same distances are similar but the levels are different for all the BE sizes. This is due because of the definition of the traction vector, which is considered a pressure, so it changes with the BE size. This means that by giving the same traction vector as an input to different BE sizes will return different magnitudes in the responses:

the larger the element the grater the equivalent magnitude of the force. Appendix E shows how the traction vector is calculated in order to get the same transfer function of the ground for different boundary element sizes. This problem is not present with the FE because the force applied to a node of the FE model is a point force.

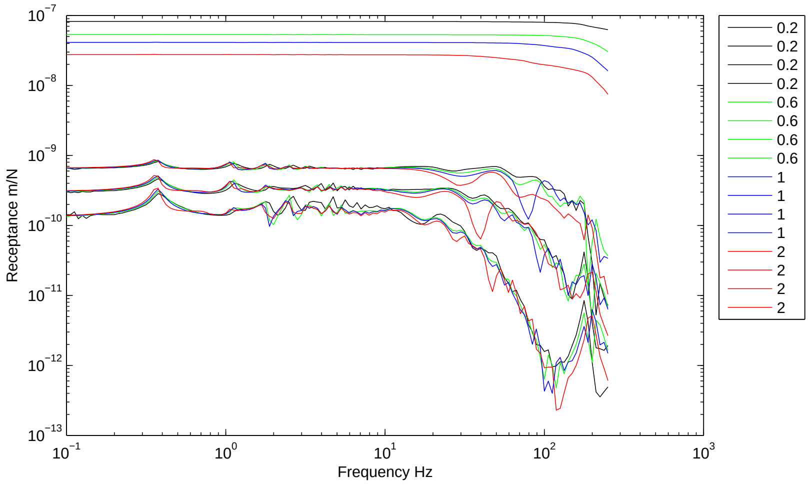

Figure 4.9: Ground transfer functions from 0 m (top line) to 24 m (bottom) for different BE length and same equivalent point force

Fig. 4.9 shows the same ground transfer functions as shown in fig. 4.8 but with the correction of the traction vector. It can be seen that now the responses at the far field have all the same levels while there are still some problems on the near field response. From fig. 4.9 can also be noticed that at higher frequencies the response obtained with wider boundary elements is less accurate, this is due to the aliasing problem addressed before. By increasing the element size it happens that a lower range of frequencies can be inspected with good approximation as seen in equation (4.2).

Comparison with analytical model

In order to investigate if the results obtained with WANDS are consistent the comparison with an analytical model has been made. The analytical model used is an axisymmetric layered ground model based on stiffness matrices, [38]. This has been previously implemented in a MatLab program kandr and it is able to give the ground transfer functions due to a point load at different distances. This can be used for grounds with one or more layers. The force in the kandr model is applied to a rigid circular indenter of defined size. Since in the far field the force is approximated as a point force the indenter does not have an influence on these transfer functions but it influences the transfer functions of the near field.

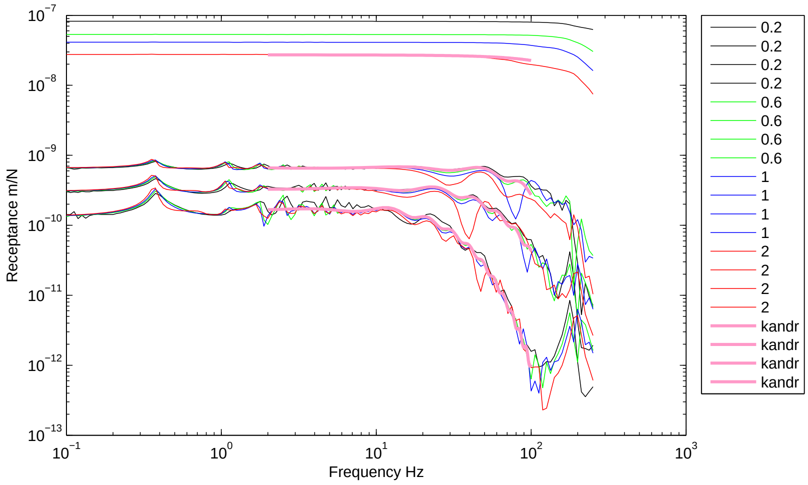

Figure 4.10: Ground transfer functions from 0 m (top line) to 24 m (bottom) for different BE length and same equivalent point force compared with results from kandr

Fig. 4.10 shows the ground transfer functions for different element sizes and adjusted with the right traction vector obtained with WANDS compared with the analytical solutions obtained with kandr. From fig. 4.10 can be noticed that in the far field there is good agreement between the analytical and numerical results. Since the analytical results are not affected by the wavenumber range and resolution, the analytical transfer functions do not present the low and high frequency noise that is present in the numerical solution.

In order to verify if WANDS gives good results under different conditions also two other simulations have been run with two completely different grounds as presented in Section 4.1.1.

Fig. 4.11 shows the dispersion curve in the vertical direction for this stiffer ground. It can be noticed that the slope of the slowest wave present in this ground is much lower than the previous case this ends up in a faster ground.

Fig. 4.12 shows the results from the numerical and analytical models for

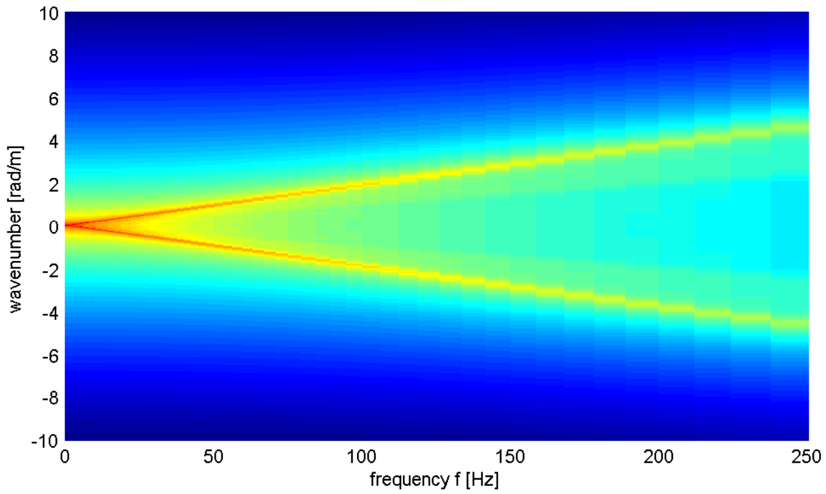

Figure 4.11: Dispersion curve for stiffer ground with characteristics reported in table 4.1

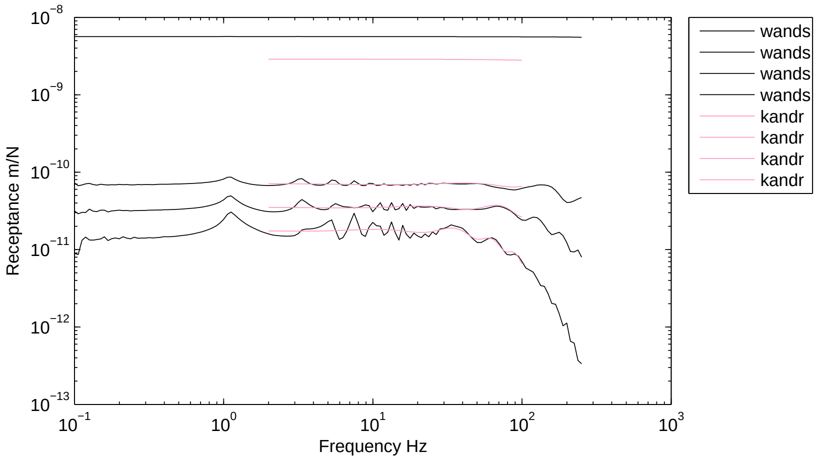

Figure 4.12: Ground transfer functions from 0 m (top line) to 24 m (bottom) for the stiffer ground compared with results from kandr

the stiffer ground compared. From fig. 4.12 can be observed that also for this case the numerical results match well the analytical ones. As said already the low frequency noise is due to the resolution of the wavenumber range. It can also be noticed that the high frequency noise is almost absent even if the wavenumber range is the same as the previous case. This is due to the fact that this type of ground is faster so the wavenumber range chosen is able to describe well the dispersion curve and this describes well all the components of the wave in the frequency rage inspected.

In the end the results for the last ground inspected are presented

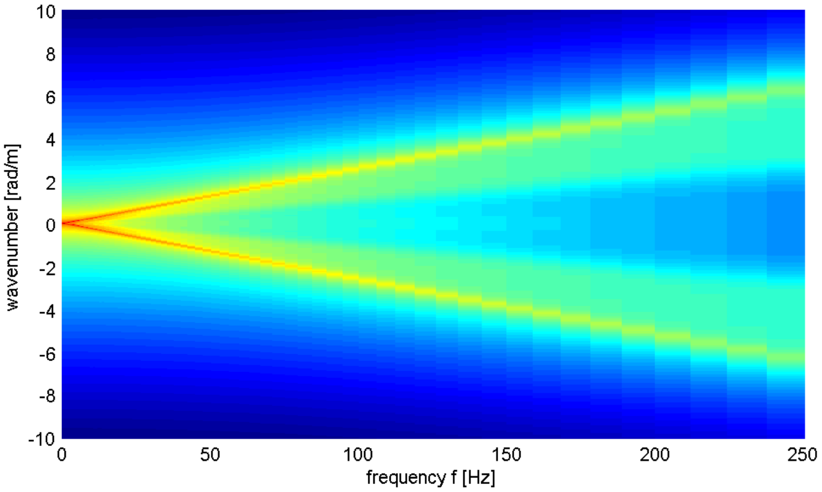

Figure 4.13: Dispersion curves for the Horstwalde ground with characteristics reported in table 4.2

Fig. 4.13 shows the dispersion curve in the vertical direction for the Horstwalde ground. From the dispersion curve it can be noticed that this ground is slower than the previous one but it is faster than the first one. This is in agreement with the data of the grounds that reports the shear waves speed for the three different grounds. For this case the dispersion curve describes well all the waves information in the frequency rage inspected but it might be too narrow at high frequency, this means that high frequency noise can be expected.

Fig. 4.14 shows the ground transfer functions at different distances for both the analytical and the numerical models. It can be seen that for this case there is very good agreement between the analytical and numerical results even if at low frequency there still is the issue of the wavenumber

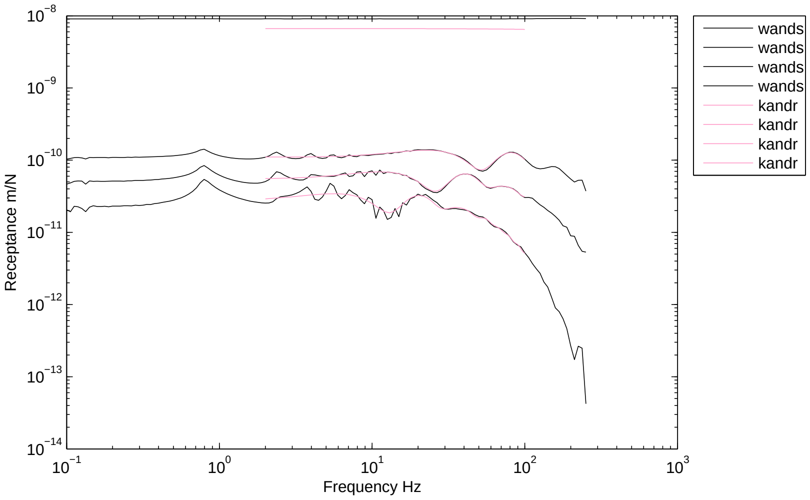

Figure 4.14: Ground transfer functions from 0 m (top line) to 24 m (bottom) for the Horstwalde ground compared with results from kandr

resolution. As predicted a bit of high frequency noise can be found in the numerical results.

4.2.2 Two layered ground

Here the results from the two layered ground presented in Section 4.1.2 are shown. All the assumptions made in Section 4.2.1 are valid also for this case. The main difference for this case is that the waves in the top layer do not only propagate toward infinite but also get reflected from the lower halfspace interface.

Fig. 4.15 shows the dispersion curve in the vertical direction for the two layers ground. For this case the calculation time start to be important due to the high number of nodes. For example for this case the structure has 483 nodes that assemble 240 boundary elements. The wavenumber range chosen is of ±10 rad/m, and the discretization of 512 points. A logarithmic sampling of the frequencies between 1 and 250 Hz has been used and this gives 97 frequencies to be calculated. Using the High Performance Computer (HPC) which has the possibility to run the simulation in parallel on 260 processors it took 13 hours against the average one hour needed for the previous cases where only 161 nodes and 80 boundary element where considered.

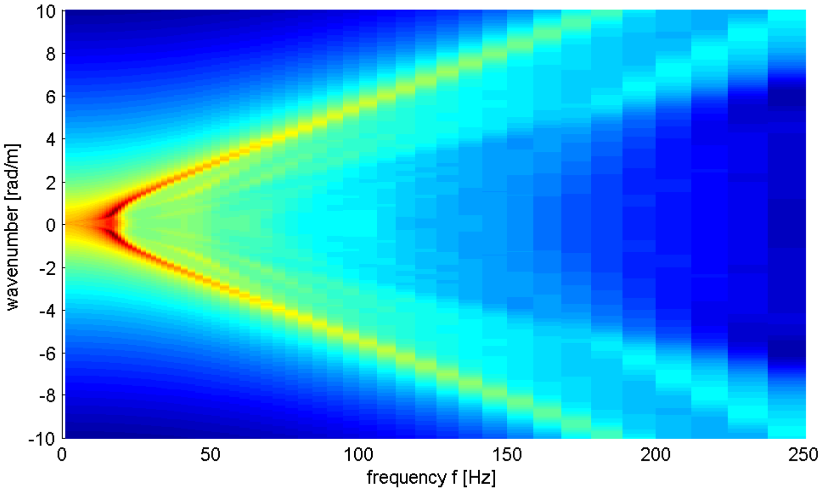

Figure 4.15: Dispersion curve for the two layers ground with characteristics reported in table 4.1

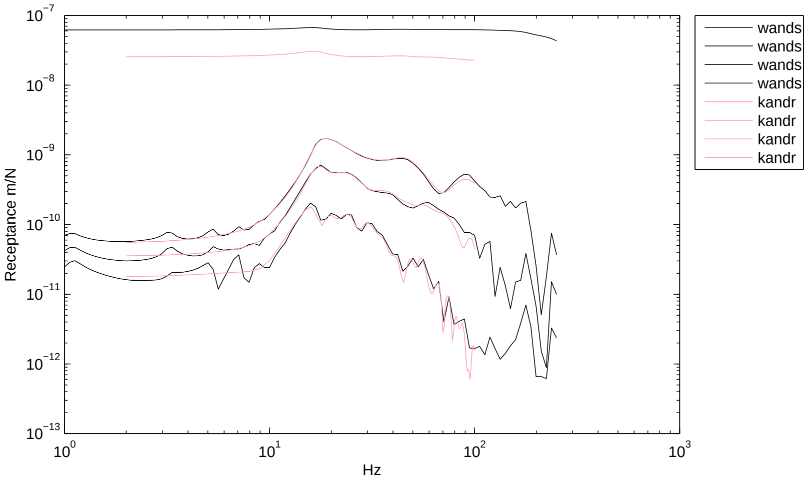

Figure 4.16: Ground transfer functions from 0 m (top line) to 24 m (bottom) for the 2 layers ground compared with the results from kandr

Fig. 4.16 shows the ground transfer functions for the top layer of the two layered ground. From fig. 4.16 can be noticed that the shaped of the transfer functions are completely different from the shapes of the previous ones, this is probably due to the presence of the reflected waves that in the previous cases where absent and to the cut on frequency of the other layer. It can also be noticed that there is good agreement between the analytical and numerical model even if at low and at high frequencies there is noise due to the resolution of the wavenumbers and to the wavenumber range respectively. Also for this case the transfer function at 0 m gives some problems due to the reconstruction of the force in the third dimension but as already explained this is not important for the case discussed in this thesis.

4.2.3 Underground tunnel

Here the results from the underground tunnel presented in Section 4.1.3 are shown. The main difference this time is that the force is not applied on the boundary elements but on the FE structure of the tunnel. For the results shown in this Section the force has been applied to the center of the tunnel invert.

Since no experimental data has been found about the receptance of the tunnel or of the transfer receptance from the tunnel to the ground surface no actual comparisons can be made. For this case only the comparison with the FE model of the tunnel presented in Section 3.1.4 can be made.

Fig. 4.17 shows the two receptances obtained with the Polimi FE model and with WANDS FE model of the tunnel plus the BE model of the ground, the spikes of WANDS' frequency response are due to the low resolution of the wavenumber range chosen this way to keep the computational time low. It can be noticed that can not be found agreement between the two models, this is because of the circumferential stiffeners present in the Polimi model. These can not be reproduced in WANDS but, in order to find agreement with the Polimi model, an equivalent hight of the tunnel walls can be obtained, this reports the mass per unit length of the two models the same.

Fig. 4.18 shows the invert receptance of the WANDS model after the adjustment of the hight and mass. The receptance got closer to the one obtained with the Polimi FE model but not yet enough. This is because the circumferential stiffeners act as rib of the tunnel inhibiting the circumferential deformation. A test with the walls as thick as the stiffeners has

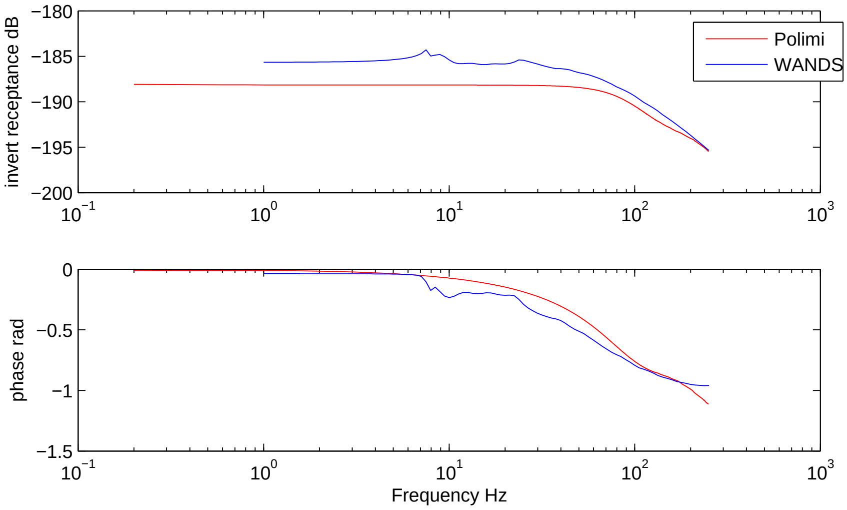

Figure 4.17: Tunnel invert receptance obtained with WANDS model compared to the Polimi model

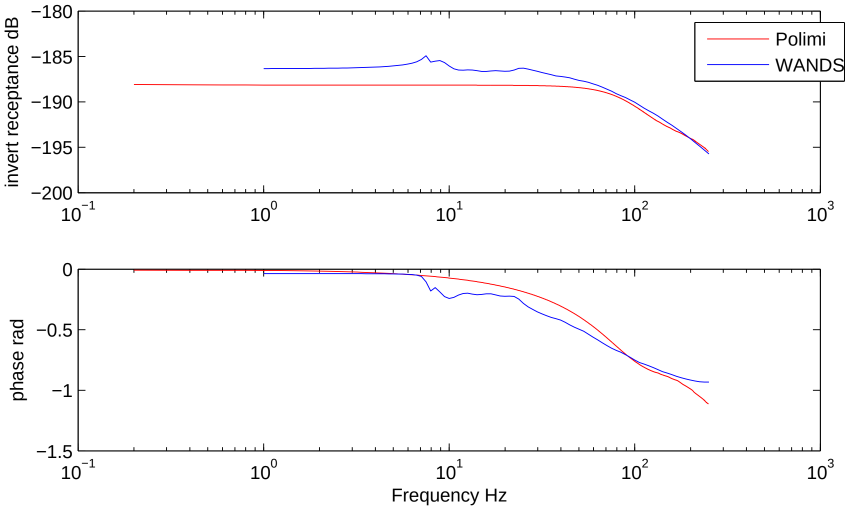

Figure 4.18: Tunnel invert receptance obtained with WANDS model compared to Polimi model with equivalent wall hight

been made in order to see if they actually affect the response that much, the density of the walls has been changed to maintain the same mass found before.

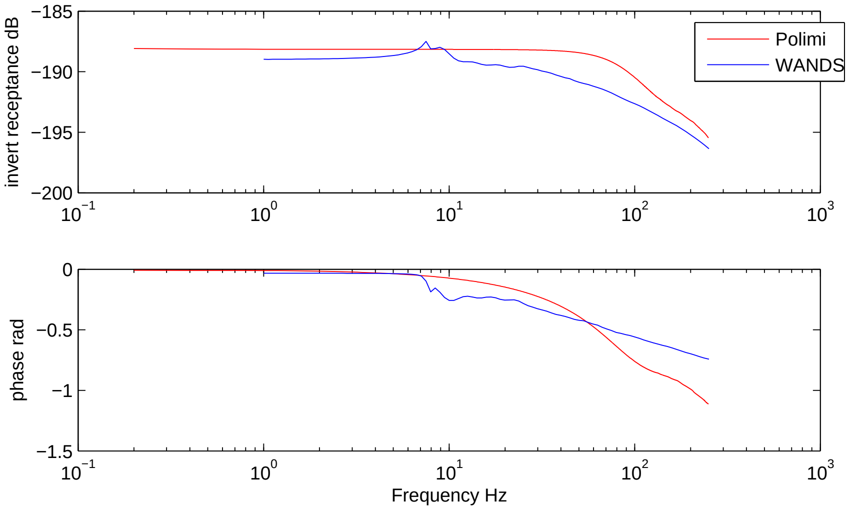

Figure 4.19: Tunnel invert receptance obtained with WANDS model compared to Polimi model with thick walls

Fig. 4.19 shows the invert receptance of the WANDS model after making the walls of the tunnel as thick as the circumferential stiffeners. It can be seen that the thickness of the walls has a big effect on the response but by making the walls as thick as the stiffeners rings gives a response which is too low, this is because the stiffeners in Polimi's model are periodically spaced. Since in WANDS is not possible to implement a periodic behavior an equivalent hight has to be found.

Fig. 4.20 shows the invert receptance of the WANDS model after adjusting the walls thickness and walls density. It can be seen that now that the right hight of the tunnel walls has been found there is good agreement between the frequency responses of the two cases.

The dispersion curve and the transfer function of the ground surface can also be inspected. As seen before from the dispersion curve it is possible to evaluate the wave speed of the propagating waves while the transfer functions give the level of vibration.

Fig. 4.21 shows the dispersion curve for the ground surface in the vertical direction due to a force on the tunnel invert. With the simplified procedure

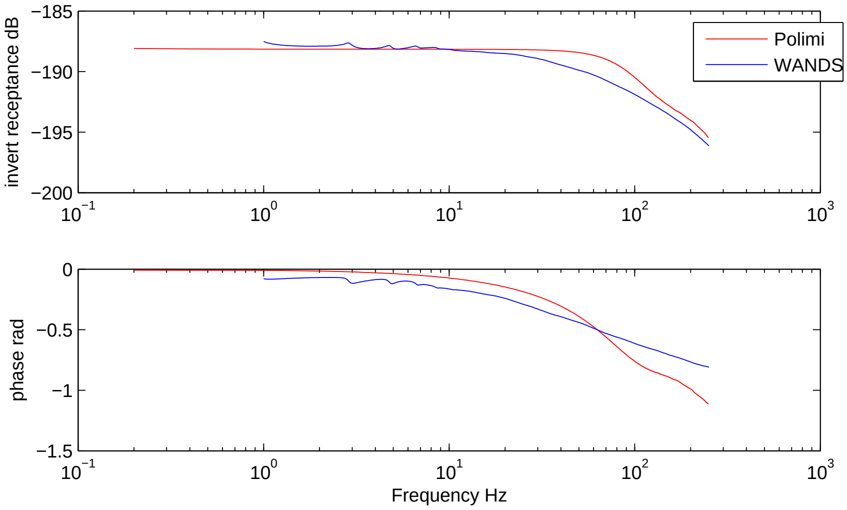

Figure 4.20: Tunnel invert receptance obtained with WANDS model compared with Polimi model with right thickness of walls

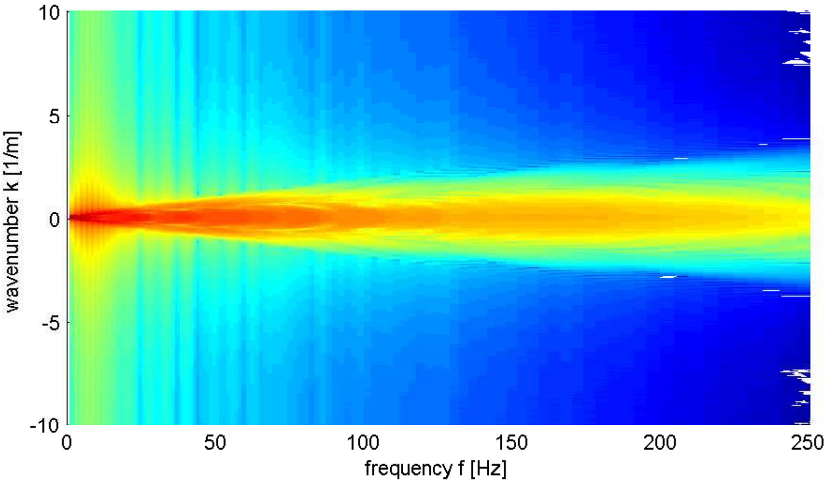

Figure 4.21: Dispersion curve for the ground surface

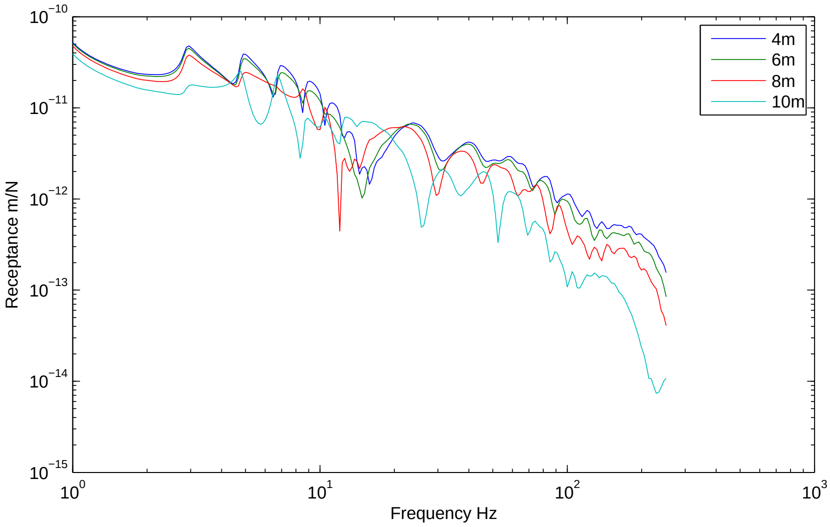

Figure 4.22: Ground surface transfer functions from 0 m (top line) to 24 m (bottom)

presented before it is possible to calculate the S-wave speed for this ground that is around 250 m/s. This is in accordance with the data found in [26] for the ground parameters.

Fig. 4.22 shows the transfer functions of the ground surface due to a force on the tunnel invert. It can be noticed that they are all very close due to the fact that the tunnel is very far underground.

Chapter 5

Results from the hybrid formulation

This Chapter presents the results from the hybrid model for the different configurations of ground and track, in terms of RMS of the velocity. The ground responses are obtained with the hybrid formulation presented in Section 2.3. In order to show the results four different distances from the point of application of the force have been selected. This gives the opportunity of investigate how the ground response is affected by the distance. The results for the three different types of ground are presented: the simple halfspace, the two layered ground and the deep bored tunnel. At these grounds have been applied the forces from the two different rails, with and without the joint, in order to obtain the responses.

The position considered to show the results of the ground vibration are 4, 6, 8 and 10 m away from the section at which the force is applied, along the y axis.

The results are also compared with the International Standard ISO 2631 that reports the limit levels for the human exposure to whole-body vibration. The curve reported on the graphs is the 24 hours exposure which is the most restrictive.

Halfspace with simple track

Here are presented the levels of vibration of the receiver, for the case of the halfspace, with a regular track laying on top of it. The test train used for the time domain simulations is a three cars train with two motor cars and one trailer car. In order to obtain these results 153 sleepers have been considered with a total length of the track of 160 m and a total time of the pass-by of $T = 22.5$ s. Since the level of the response depend on the total time of the pass-by, due to the auto and cross spectra of the forces, a normalization has been used to report the levels to the length of the train by adding $10 \log_{10} T/t_v$ where t_v is the length of the train divided by its speed.

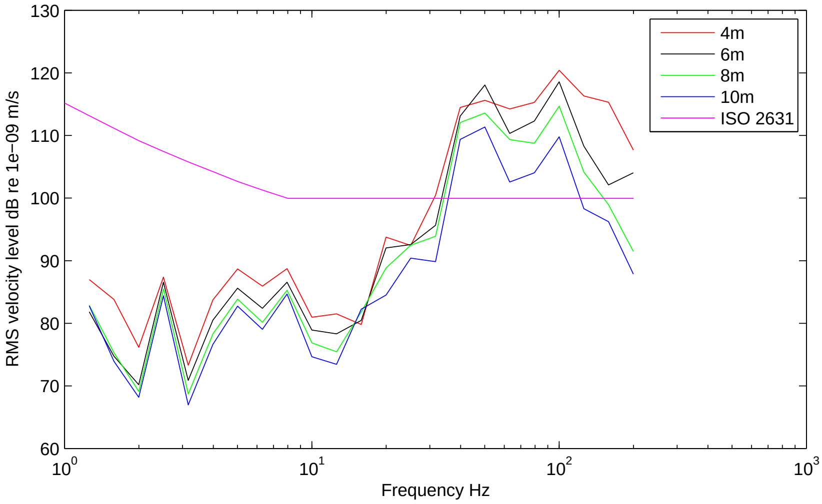

Figure 5.1: Third octave bands ground response to train pass-by for the soft halfspace with regular track

Fig. 5.1 shows the results for the pass-by of the train on a track laying on a halfspace with the characteristics of the upper layer presented in table 4.1, in third octave bands.

Fig. 5.2 shows the results for the pass-by of the train on a track laying on a halfspace with the characteristics of the halfspace presented in table 4.1, in third octave bands.

Fig. 5.3 shows the results for the pass-by of the train on a track laying on a halfspace with the characteristics presented in table 4.2, in third octave bands.

It can be noticed that the shape of the spectra of the responses of the ground remains almost the same as the distance from the point of application of the force increases while the magnitude decreases. This is due to the transfer functions of the ground, as seen in Section 4.2.1. While the shape

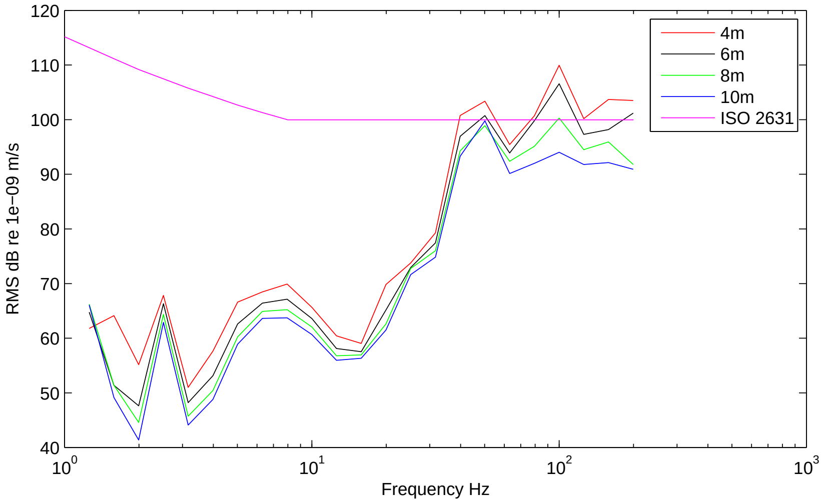

Figure 5.2: Third octave bands ground response to train pass-by for the stiff halfspace with regular track

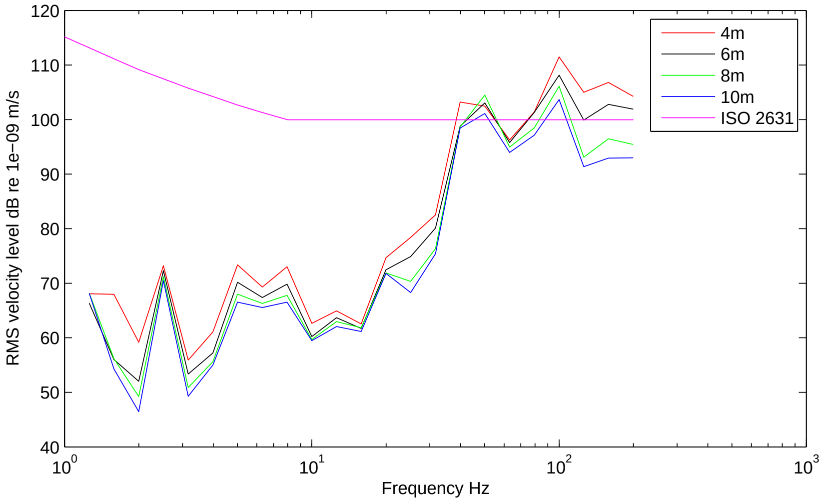

Figure 5.3: Third octave bands ground response to train pass-by for the Horstwalde halfspace with regular track

mainly depends on the shape of the spectra of the force used as input because the transfer functions of the ground are almost flat up to 100 Hz. It can also be noticed that the magnitude of the velocity decreases as the stiffness of the ground increases and that there are two main peaks at around 50 and 100 Hz. By looking at the standard levels it could be noticed that for the distances considered the levels are, almost for all cases, over the limit this means that if a building where people have to live or work need to be built it has to be farther than 10 m away otherwise vibration mitigation mechanisms have to be taken into account.

Halfspace with track containing joint

Here are presented the results for the case of the halfspace, with a track containing a joint laying on top of it. The parameters choose for the analysis are the same as the one of the previous case.

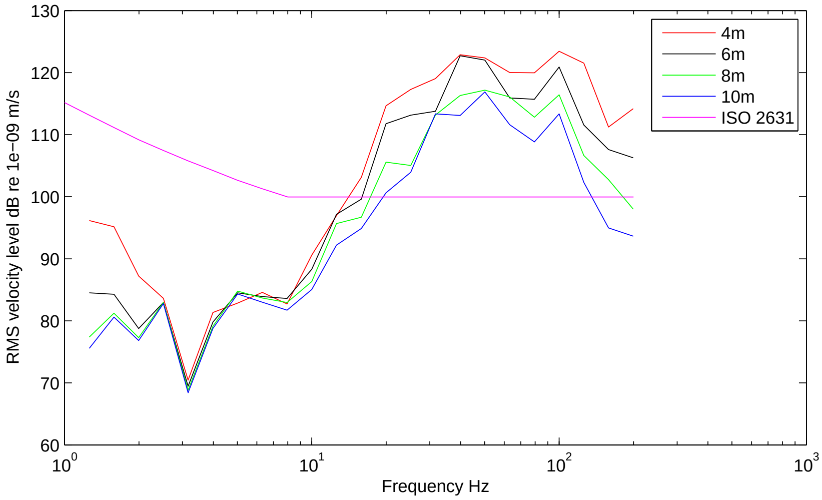

Figure 5.4: Third octave bands ground response to train pass-by for the soft halfspace with joint

Fig. 5.4 shows the results for the pass-by of the train on a track with joints laying on a halfspace with the characteristics of the upper layer presented in table 4.1, in third octave bands.

Fig. 5.5 shows the results for the pass-by of the train on a track with joints laying on a halfspace with the characteristics of the halfspace presented in table 4.1, in third octave bands.

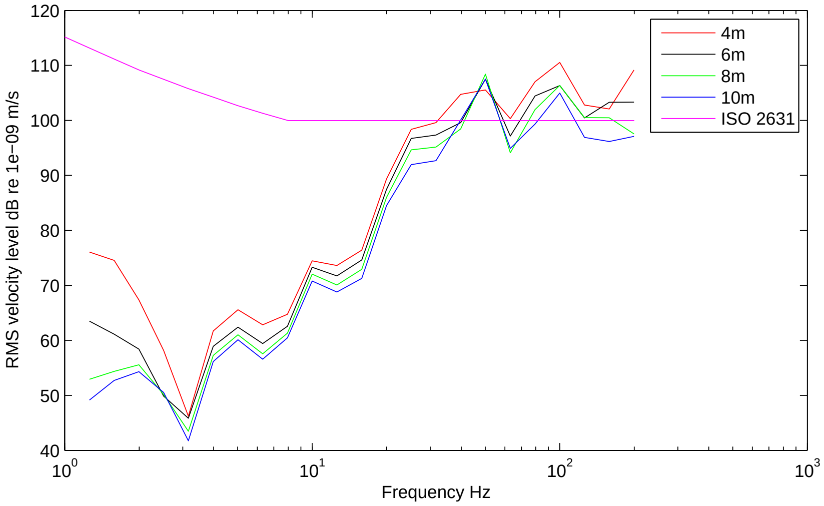

Figure 5.5: Third octave bands ground response to train pass-by for the stiff halfspace with joint

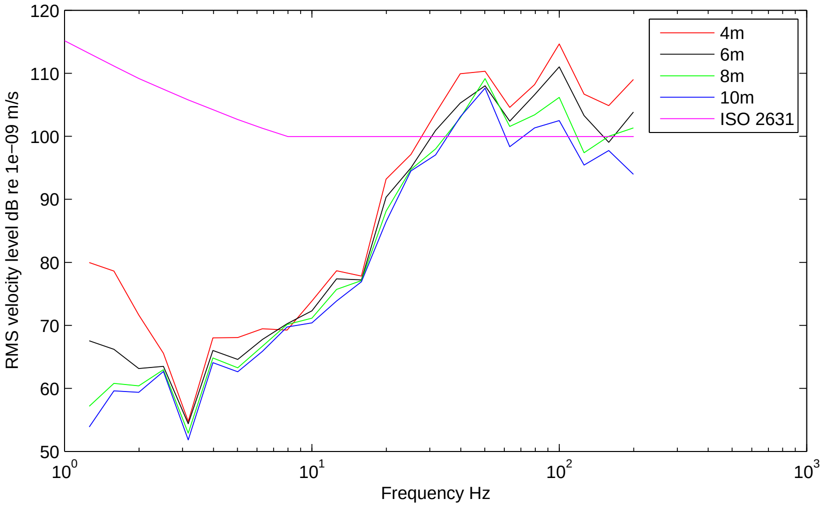

Figure 5.6: Third octave bands ground response to train pass-by for the Horstwalde halfspace with joint

Fig. 5.6 shows the results for the pass-by of the train on a track with joints laying on a halfspace with the characteristics presented in table 4.2, in third octave bands.

It can be noticed that the addition of the joint gave a higher level of the force for all three grounds. This is reasonable due to what was found in Section 3.2.5.

Two layered ground

Here are presented the levels of vibration for the case of the two layered ground with characteristics shown in table 4.1, the first with a regular track and the second with a track with joints. Also for this case the other parameters are the same as for the first case presented.

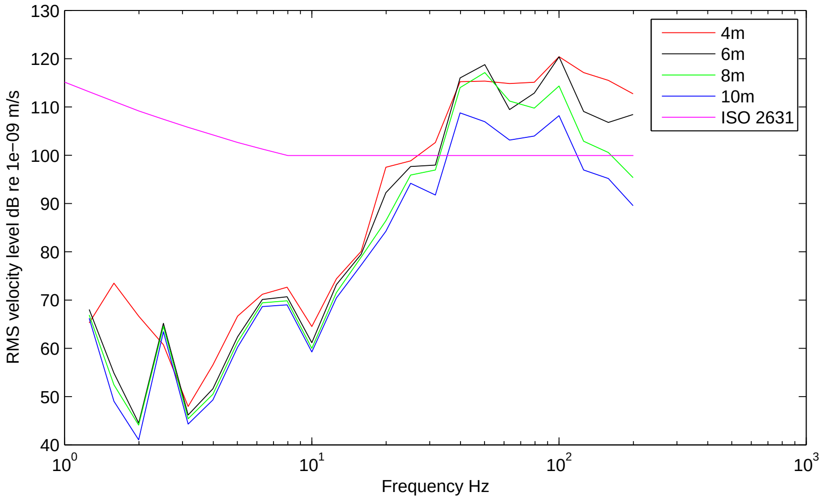

Figure 5.7: Third octave band ground response to train pass-by for the two layered ground with regular track

Fig. 5.7 shows the results for the pass-by of the train on a regular track laying on a two layers ground. It can be noticed that the magnitude of this case is higher than the one of the halfspaces presented before, this is congruent with what found for the ground transfer functions in Section 4.2.2. For this case due to the wave reflection at the interface between the first and second layer there is an increase in the vibration levels. The two peaks at 50 and 100 Hz are still present but the difference is not as sharp as for the halfspaces.

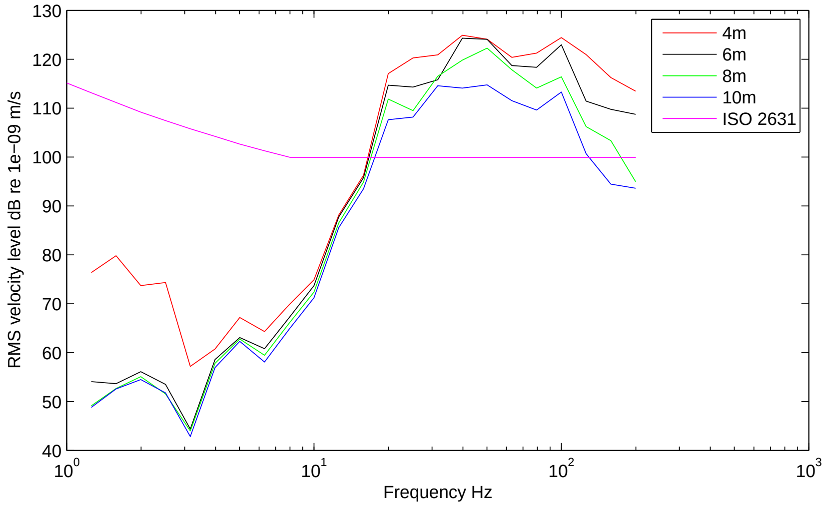

Figure 5.8: Third octave band ground response to train pass-by for the two layered ground with joint

Fig. 5.8 shows the results for the pass-by of the train on a track containing joints.

Underground tunnel

Here are presented the levels of vibration for the case of the underground tunnel embedded in the ground. At first are proposed the results for the regular track and than for the track containing the joints. Also for this case the other parameters are the same as for the first case presented.

Fig. 5.9 shows the results on the ground surface due to the pass by of the train on a regular track inside an underground tunnel. It can be seen that the responses are not very different because the levels of the ground mobilities are not very different at different distances. This is due because the tunnel is berried very deep in the ground and this gives a similar response at different distances. Also for this case can be shown the results for the pass by of the train on a track containing joints.

Fig. 5.10 shows the results on the ground surface due to the pass by of the train on a track containing joints. Also for this case can be noticed that the levels increased and also the peak is less narrow this means that the energy introduced by the joints is relevant.

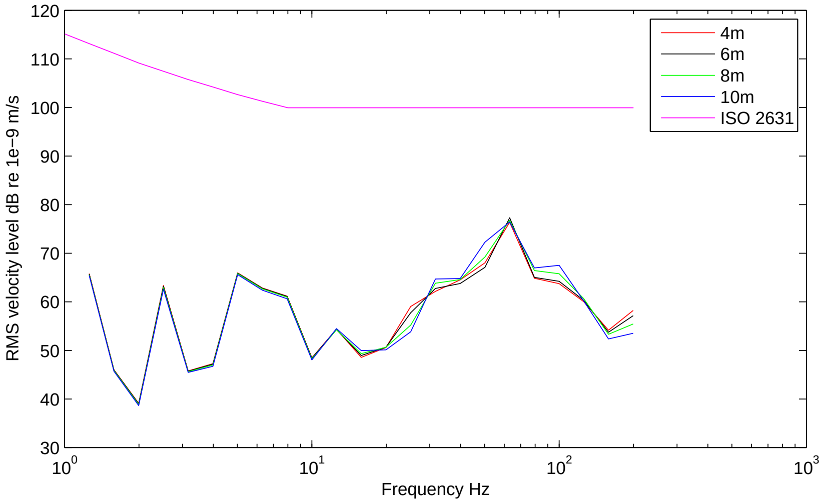

Figure 5.9: Third octave band ground surface response to train pass-by for the underground tunnel with regular track

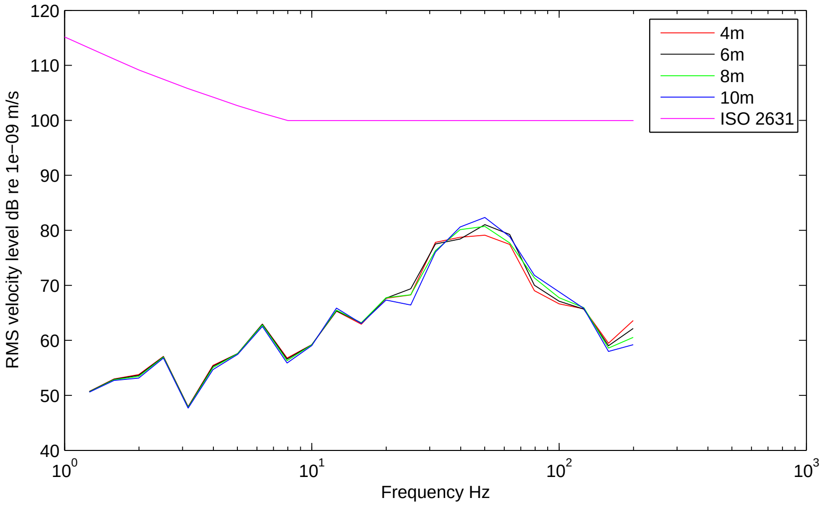

Figure 5.10: Third octave band ground surface response to train pass-by for the underground tunnel with joint

Comparison with the old hybrid model

A comparison of the results from the old version of the hybrid model and the new version implemented for this work of thesis is made in order to verify if the new model gives reasonable results.

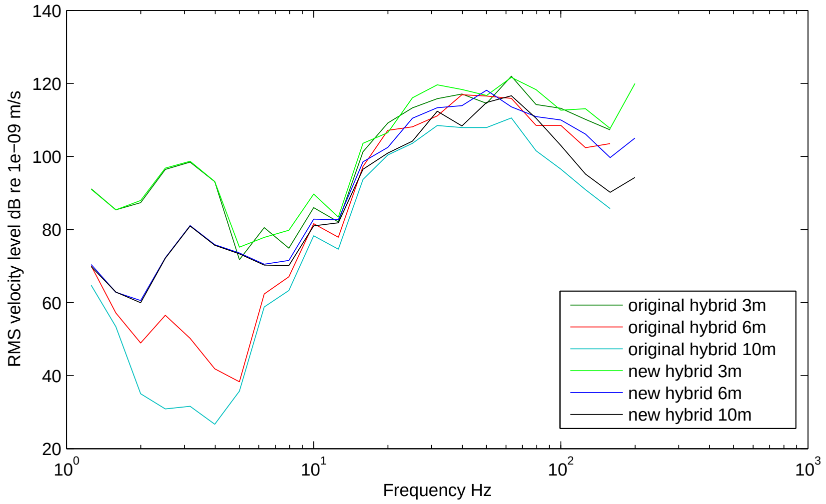

Figure 5.11: Comparison between old and new hybrid model

Fig. 5.11 shows the comparison of the results from the two different hybrid models at three different distances. The simulation has been carried on with the same parameters in order to investigate if the responses of the two different models are comparable. It can be noticed that there is good agreement between the two models. This is an important result because the previous hybrid model has been compared with the model TGV which has been compared with experimental results and both have good agreement with the experimental data so this means that also the new hybrid model has good agreement with the experimental data used to verify the TGV model, [24].

Unfortunately the results from the underground tunnel do not match well with the experimental data found in the CONVURT project but the reason is uncertain. It could be because of the different top layer properties that was not model in the ground model or to a different magnitude of the forces exchanged between the train and the rail.

Conclusions

Because of the competitiveness of rail over other forms of transport new, heavier and faster trains and an increasing amount of underground lines are being built; therefore concern is growing regarding the impact on society of rail transport systems and ground-borne noise and vibration are therefore important issues for railway companies. The research carried out in this thesis was aimed at assessing ground vibration levels due to a train pass-by in the frequency range 20-200 Hz.

In the field of ground-induced vibration, historically there have always been two separate fields, one that studies the vehicle dynamics and the wheel/rail interaction phenomenon, usually in the time domain, and one that studies the propagation of the waves in the ground, usually in the frequency/wavenumber domain. Recently a new way of studying the problem of train-induced ground vibration has arise called hybrid method, [24]. This thesis presents this novel method that combines the time domain vehicle dynamics with the wavenumber/frequency domain wave propagation in solids and shows a few examples where the method can be applied. To do so the work was carried on at two different universities: Politecnico di Milano contributed with knowledge on vehicle dynamics and wheel/rail contact problems while the University of Southampton shared expertise on wave propagation and ground dynamics.

This enabled the use of two powerful softwares developed in the last decades in these two universities. The software from Politecnico di Milano models the train as a mixed rigid/flexible multi-body model and the structure as a finite element model. It integrates the pass-by of the train in the time domain giving as outputs the time histories of the forces, displacements, velocities and accelerations of the nodes the structure and the trainset. The software from University of Southampton is a linear model of the ground that operates in the frequency/wavenumber domain (so called 2.5D). It uses the finite element and boundary element method to describe the cross section of the ground and then the wave propagation in the third direction is reconstructed by means of wavenumbers.

The hybrid method presented in this work uses the forces transmitted to the ground obtained from the time domain calculation and the transfer functions of the the ground between the point of application of the force and the position of the receiver. The linking between the two results is done using the auto and cross spectra of the forces; in this way the information about the phase of the force is not lost, thus taking into account the movement of the train in time and space. The result of this linking process is the PSD of the velocity at a receiver position located anywhere on the ground surface.

During this research this methodology was used to predict the levels of vibration induced by trains transiting on a surface railway line and on an underground railway. A possible application is its adoption during the design stage of a new line to investigate if the new railway would significantly affect or not the people living or working in the surrounding area. It can also be used to investigate whether a vibration mitigation solution proposed for an existing or for a new line would be effective or not.

The main disadvantage of this method is the computational time needed to run both the time domain calculation and the frequency domain calculation. As an example the time needed to solve the time domain pass-by of the train in the tunnel structure, on the Politecnico's server, takes about 24 hours while the frequency/wavenumber domain model of the two layer ground, with 1024 wavenumbers, takes about 12 hours on the University of Southampton's cluster. For a case of an underground railway the contribution of the tunnel can be considered in the frequency wavenumber domain calculation because only a limited number of nodes is needed. This would speed up the time domain calculation and will not slow down too much the frequency wavenumber domain one.

Both improvements in computational time and measurement validation are required before the process can be successfully transfered to the industry and these are the topics where further developments are needed in the near future.

Appendix A

CONVURT experimental data

First of all is reported the experimental set and data found from the CONVURT (CONtrol of Vibrations from Underground Rail Traffic) project which has been used to validate the models developed, [26]. This was a project carried on as a collaboration among different universities and different companies. Its aim was to create validated innovative and quantitative modelling tools to enable prediction of locations where ground-borne vibration transmission and thereby noise would occur in metropolitan railway networks.

The measurements have been taken at a site in Regent's Park on the Bakerloo line of London Underground. The track in the tunnel is of the conventional London Underground type. It is a non-ballasted concrete slab track with a 47 kg Bullhead rail supported on hard Jarrah wooden sleepers nominally spaced at 0.95 m with cast iron chairs, table A.1 shows the rail characteristics for the Bakerloo line. The space between the sleepers is filled with shingle, which does not support the sleepers but provides drainage and a flat surface for evacuation in case of emergencies. The rails are not supported by rail pads and the resilience is mainly provided by the local resilience of the timber sleeper, which has a stiffness of approximately 70 kN/mm.

From the CONVURT reports it's known that the rail receptance measurements have been performed in an unloaded track condition by applying lateral and vertical excitations to the rail head at two positions, directly over the sleeper and at mid-span between sleepers. Two instrumented ham-

A	$5490\ 10^{-6}$	m^2
E	$2.06\ 10^{11}$	Pa
ν	0.3	
J_{22}	$1602\ 10^{-12}$	m^4
J_{33}	$171\ 10^{-12}$	m^4
ρ	7800	kg/m^3
m_s	70	kg

Table A.1: Characteristics of the rail, [34]

mers have been used to improve the accuracy of the frequency response and to cover the frequency range up to 5 kHz: a relatively big hammer with an effective mass of 4.218 kg and a soft plastic tip, covering the frequency range up to 1 kHz, and a smaller hammer with an effective mass of 0.646 kg with a harder tip, covering the frequency range up to 5 kHz at lower force levels.

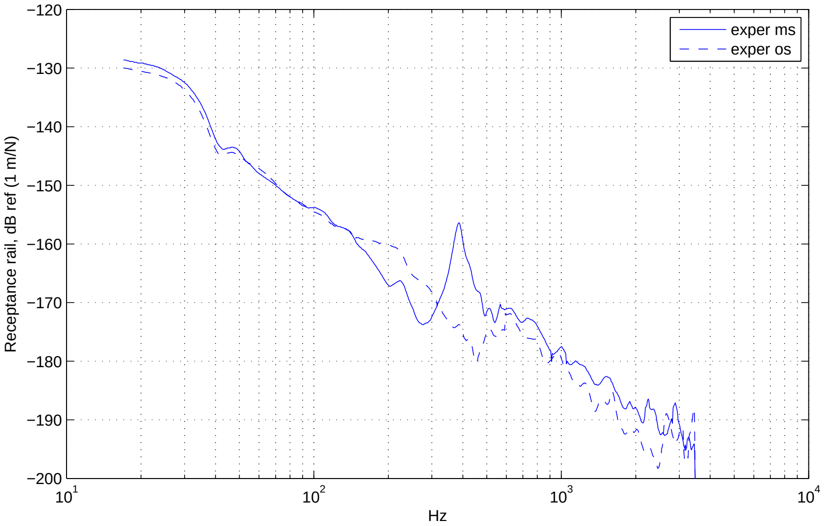

Figure A.1: Experimental rail receptance from the CONVURT project, [26]

Fig. A.1 shows the vertical rail receptance measured over the sleeper and at mid span taken from [26]; the latter curve clearly shows a 'pinned–pinned' resonance frequency of 380 Hz. The 'pinned-pinned' resonance occurs when a half wavelength corresponds with the length between the sleepers, hence this depends firstly of the spacing between the supports and than also on the bending stiffness of the rail. In fig. A.1 it's evident that at low frequency the response of the track keeps on growing, this is not what usually is observed and it is not what has been found using the numerical or analytical models [39], so it's possible that below 100 Hz the experimental frequency response of the rail suffers of some errors due to the way the frequency response has been measured, this could be verified by looking at the phase information of the receptance but from [26] there is no information regarding the phase of the receptance.

From the CONVURT project there are also the specification for the tunnel on the Bakerloo line. It is a deep-bored tunnel with a cast iron lining and a single track, embedded in London clay at a depth of about 28 m below the surface. The tunnel has an external radius of 1.953 m, while the thickness of the lining is 0.022 m. There are six longitudinal stiffeners (with a height of 0.102 m and a width of 0.057 m) and one circumferential stiffener at an interval of 0.508 m in the longitudinal direction, resulting in a periodic tunnel structure

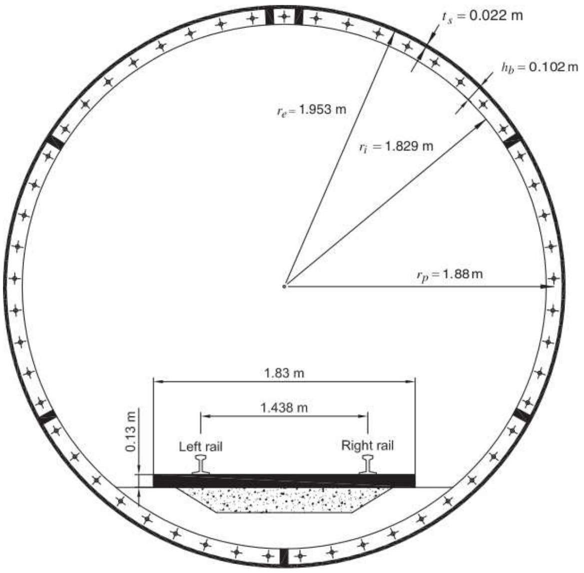

Figure A.2: Drawing of the tunnel from the CONVURT project [26]

Fig. A.2 shows the drawing of the tunnel at the sight considered in [26].

Table A.2 show the materials characteristics of the tunnel found in [26]. These characteristics are not present in the paper but have been found in the literature.

During the experimental campaign of the CONVURT project also cone

		Cast iron	Concrete
ρ	kg/m^3	7200	2000
E	Pa	$1.2\ 10^{11}$	$3.5\ 10^{10}$
ν		0.3	0.28

Table A.2: Characteristics of the tunnel

penetration tests were performed in different positions up to a depth of 21 m. Two different layers have been identified: a shallow top one which were found to be not very homogeneous made of clay with inclusions of sand; a second very deep layer which were found to be very homogeneous.

		Upper layer	Halfspace
P-wave speed	m/s	1964	1571
S-wave speed	m/s	275	220
ρ	kg/m^3	1980	1980
β		0.042	0.039

Table A.3: Characteristics of the soil, [26]

Table A.3 reports the characteristics of the soil found in the test site in London.

The test train used for the data acquisition is a normal refurbished 1972 passenger train, consisting of seven cars: a driving motor car, a trailer car, two non-driving motor cars, two trailer cars and a driving motor car. The length of a motor car is 16.09 m, while the length of a trailer car is 15.98 m. The bogie and axle distances on all cars are 10.34 and 1.91 m, respectively. The total length of the test train is 112.29 m, while the distance between the first and the last axle of the train is 108.33 m. The wheels are of the monobloc type and have a diameter of about 0.70 m. The tare mass of a motor car is 15330 kg, while the bogie mass is 6690 kg and the mass of a wheelset is 1210 kg. The tare mass of a trailer car is 10600 kg, while the bogie mass is 4170 kg and the mass of a wheelset is 950 kg.

Appendix B

Infinite plate strip

To better understand how the program WANDS works a simple structure is been investigated: the simply supported plate strip. Two different finite element types have been used: the plate elements and the solid elements. The advantage of the plate elements is that the number of nodes, compared with the solid elements, is much smaller but the solid elements are easier to couple with other elements.

Table B.1 shows the characteristics of the plate chose as example.

L	1	m
h	6e-3	m
E	7.100e+10	Pa
ν	0.332	
ρ	2700	kg/m^3
η	0.100	

Table B.1: Plate specifications

B.1 Analytical solution

For a thin undamped plate, the out-of-plane displacement $w(x, y, t)$ in the absence of external forces satisfies the following differential equation

$$D\left(\frac{\partial^4 w}{\partial x^4} + 2\frac{\partial^4 w}{\partial x^2 \partial y^2} + \frac{\partial^4 w}{\partial y^4}\right) + (\rho h)\frac{\partial^2 w}{\partial t^2} = 0 \qquad \text{(B.1)}$$

Where $D = \frac{Eh^3}{12(1-\nu^2)}$ is the plate bending stiffness.

Harmonic motion is assumed at the angular frequency ω, with a time dependence $e^{j\omega t}$. Due to the use of simply supported boundaries, the response amplitude w of the plate may be separated into its x and y components and written as a summation over components with m half-sine waves across the width L

$$w(x, y) = \sum_{m=1}^{\infty} w_m(x) \sin\left(\frac{m\pi y}{L}\right) \tag{B.2}$$

where $w_m(x)$ is the complex amplitude of the m^{th} component that depends on the excitation. This series forms a complete set of functions which satisfy the boundary conditions on $y = 0$ end $y = L$. Considering one term in the series, substituting this into equation (B.1) yields

$$\left(\frac{d^4 w_m}{dx^4} - 2\left(\frac{m\pi}{L}\right)^2 \frac{d^2 w_m}{dx^2} + \left(\frac{m\pi}{L}\right)^4 w_m\right) - \frac{\rho h}{D}\omega^2 w_m = 0 \tag{B.3}$$

Seeking solutions of the form $w_m(x) = e^{-jk_{x,m}x}$ gives

$$\left(k_{x,m}^4 + 2\left(\frac{m\pi}{L}\right)^2 k_{x,m}^2 + \left(\frac{m\pi}{L}\right)^4\right) - \frac{\rho h}{D}\omega^2 = 0 \tag{B.4}$$

which can be written as

$$\left(k_{x,m}^2 + \left(\frac{m\pi}{L}\right)^2\right)^2 = k_B^4 \tag{B.5}$$

where $k_B = \sqrt{\omega}\sqrt[4]{\frac{\rho h}{D}}$ is the free bending wavenumber of the plate. Equation (B.5) has four solutions which can be divided in two fundamentally different wave-type solutions for each m

$$k_{x_1,m} = \pm\sqrt{k_B^2 - \left(\frac{m\pi}{L}\right)^2} \tag{B.6}$$

$$k_{x_2,m} = \pm\sqrt{-k_B^2 - \left(\frac{m\pi}{L}\right)^2} \tag{B.7}$$

Real wavenumbers represent propagating waves while imaginary wavenumbers represent evanescent waves which decay with distance. At low frequency, $k_B < m\pi/L$, all four wavenumbers are imaginary so that all four waves behave as evanescent or nearfield waves. In contrast, when $k_b > m\pi/L$, $k_{x_1,m}$ is real but $k_{x_2,m}$ remains imaginary. Therefore, both propagat-

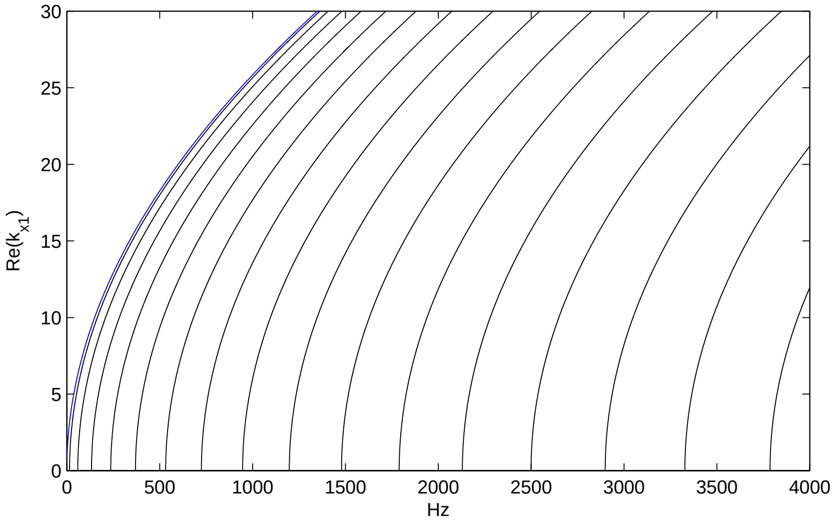

Figure B.1: Analytical dispersion curves for simply supported plate strip

ing waves and nearfield waves are present for the latter case. The frequency at which $k_B = m\pi/L$ is referred to as the m^{th} cut-on frequency ω_m and is given by

$$\omega_m = \left(\frac{m\pi}{L}\right)^2 \sqrt{\frac{D}{\rho h}} \tag{B.8}$$

The relation between the real part of the wavenumbers $k_{x_1,m}$ and frequency ω gives the dispersion curves shown in fig. B.1 where the blue line corresponds to the free bending wavenumber, k_B, these are calculated for the example parameters listed in table B.1 While fig. B.2 reports the dispersion curves due to the relation between the imaginary part of the wavenumbers $k_{x_2,m}$ where the blue line, again, corresponds to the free bending wavenumber.

Response due to a point force

There are two wave solutions for each m in equation (B.6) and two wave solutions for each m in equation (B.7), allowing the complete solution to be written as

$$\begin{aligned} w(x,y) = \sum_m \Big\{ & A_{1,m}e^{jk_{x_1,m}x} + A_{2,m}e^{jk_{x_2,m}x} + A_{3,m}e^{-jk_{x_1,m}x} + \\ & + A_{4,m}e^{-jk_{x_2,m}x} \Big\} \sin\left(\frac{m\pi y}{L}\right) \end{aligned} \tag{B.9}$$

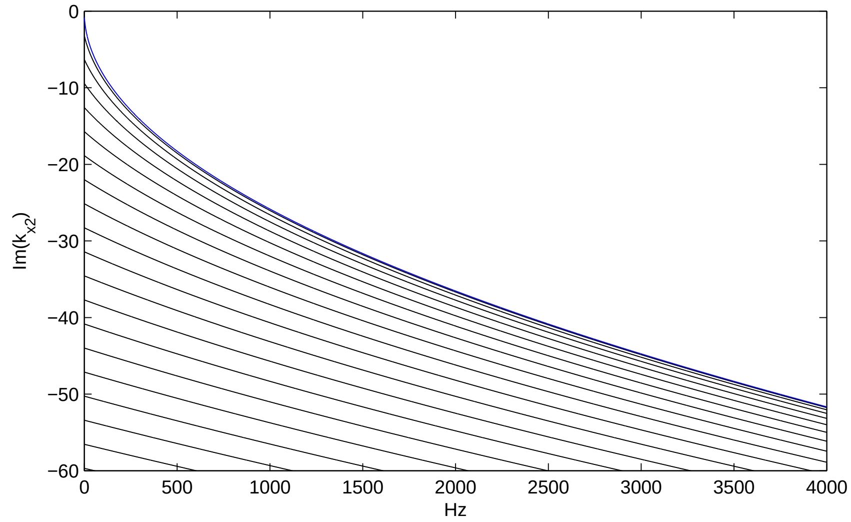

Figure B.2: Analytical dispersion curves for simply supported plate strip

In order to determine the constants $A_{1,m}$, $A_{2,m}$, $A_{3,m}$ and $A_{4,m}$, boundary conditions are required. In Appendix C the mathematical steps to determine the point mobility of the plate strip are presented.

The point mobility for the structure can be found by setting $x = 0$ and $y = y_0$

$$Y(\omega) = \sum_{m=1}^{\infty} \frac{\omega}{DLk_{x1,m}\left(k_{x1,m}^2 - k_{x2,m}^2\right)} \left[1 - \frac{k_{x1,m}}{k_{x2,m}}\right] \sin^2\left(\frac{m\pi y_0}{L}\right) \tag{B.10}$$

Considering a finite number of cut-on frequencies the point mobility becomes

Fig. B.3 show the analytical point mobility of the plate strip for two different values of the loss factor: $\eta = 0$ and $\eta = 0.1$. The red line is the point mobility of an infinite plate.

B.2 Finite Element Modelling

To investigate better how WANDS works and the differences between the solid topologies two different models have been tested: one of the plate assembled using plate elements; and on of the plate assembled using eight nodes solid elements.

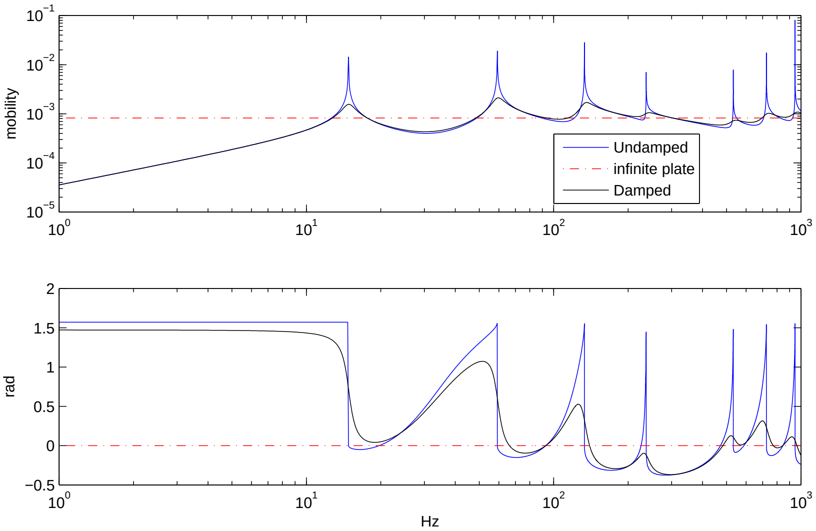

Figure B.3: Analytical point mobility of the plate strip with loss factor $\eta = 0$ and loss factor $\eta = 0.1$

B.2.1 Plate elements

In WANDS the plate element has 4 degree of freedom, $\{x_i,\ y_i,\ z_i,\ \theta_i\}$, each node so in order to obtain a simply supported plate we have to restrain the $\{x,\ y,\ z\}$ displacements of the first and last node of the plate.

In Appendix D.1 are reported all the mathematical steps to obtain the system equations with the system matrices. From equation (D.10), using the unforced solution, can be obtained the dispersion relations for the plate by substituting the solution e^{-jk} where k is the wavenumber

$$\boldsymbol{K_4} k^4 - \boldsymbol{K_2} k^2 - j\boldsymbol{K_1} k + \boldsymbol{K_0} - \omega^2 \boldsymbol{M_2} = 0 \tag{B.11}$$

Since there are two variables, ω and k, there are two main ways to obtain the dispersion relations. The first and easier way is to impose the vector for k and to invert the equation (B.11). Using this method we obtain that the only variable is ω and it becomes

$$\omega = \sqrt{\boldsymbol{M_2}^{-1} \left[\boldsymbol{K_4} k^4 - \boldsymbol{K_2} k^2 - j\boldsymbol{K_1} k + \boldsymbol{K_0}\right]} \tag{B.12}$$

This way the values for ω correspond to the eigenvalues of the term on the right and the modeshapes correspond to the eigenvectors.

Otherwise a vector for ω can be impose and solve equation (B.11) for k. This method needs to be implemented numerically as shown for example in [40] and [41].

Since the first method is easier to implement and requires a lower computational time, and for simple geometries, like the simply supported plate, gives reasonable results this method has been used. The solution of equation (B.11) gives as output the eigenvalues, ω, and the eigenvectors, $\boldsymbol{\Phi_i}$, of the matrix at the frequency ω_i.

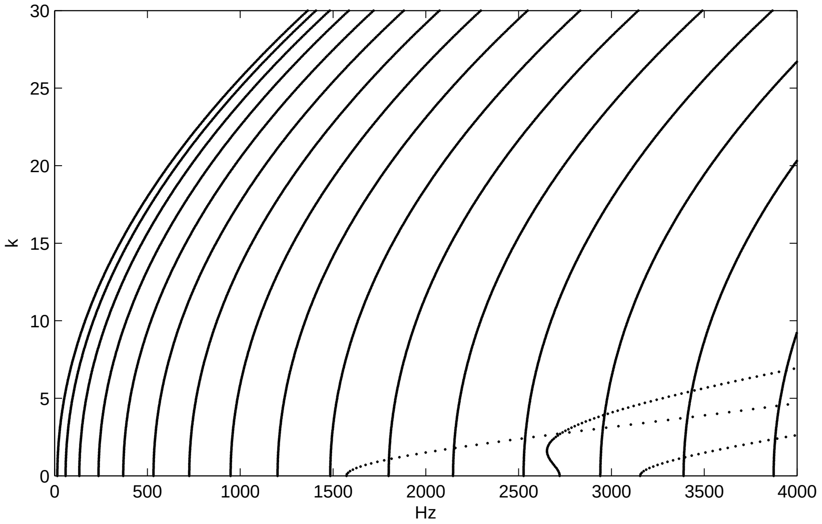

Figure B.4: FE model strip plate dispersion relations with plate elements

In fig. B.4 can be seen that there are also some wavenumbers completely different from the analytical solution, this because with the FE solution we obtain also the wavenumbers for $k_{y,m}$ and $k_{z,m}$ that in the analytical solution shown before are not considered. In fig. B.5 are showed the first three modeshapes for the plate modeled with plate elements.

Response due to a point force

The response due to a point force is obtained by the numerical integration of the structure. The outputs are the displacements of the nodes of the structure due to a force that changes in frequency applied to a node of the structure. Unfortunatly for this type of elements the forced response has not been fully implemented yet so it won't be possible to show the force

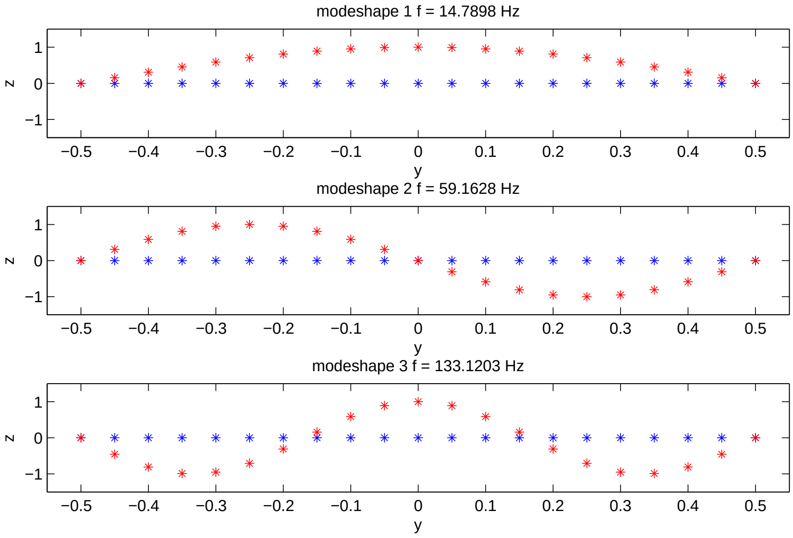

Figure B.5: FE model strip plate modeshapes with plate elements normalized by the maxima of each modeshape

response of the plate for the plate elements.

B.2.2 Solid elements

The program WANDS offers two different kind of solid elements: the four nodes and eight nodes elements. This kind of element has 3 degree of freedom per node $\{x_i,\ y_i,\ z_i\}$. It's been notice that if the nodes on the corners of the plate are restrained different results from the analytical solution are obtained, this because of the coupling of the waves at the corner. In order to obtain the same results of the analytical solution a node at the center of the thickness of the plate has to be restrain. The eight nodes elements already give this opportunity also with only one element in the thickness, instead the four nodes elements don't, so at least two rows of elements has to be used in the thickness in order to obtain right results with this topology of elements. In this case the eight nodes elements have been used.

In Appendix D.2 are reported all the mathematical steps to obtain the system equtions with the system matrices. Making the same assumptions that we made in Appendix B.2.1 the dispersion relations can be obtain as before

$$\omega = \sqrt{\boldsymbol{M_2}^{-1}\left[-\boldsymbol{K_2}k^2 - j\boldsymbol{K_1}k + \boldsymbol{K_0}\right]} \tag{B.13}$$

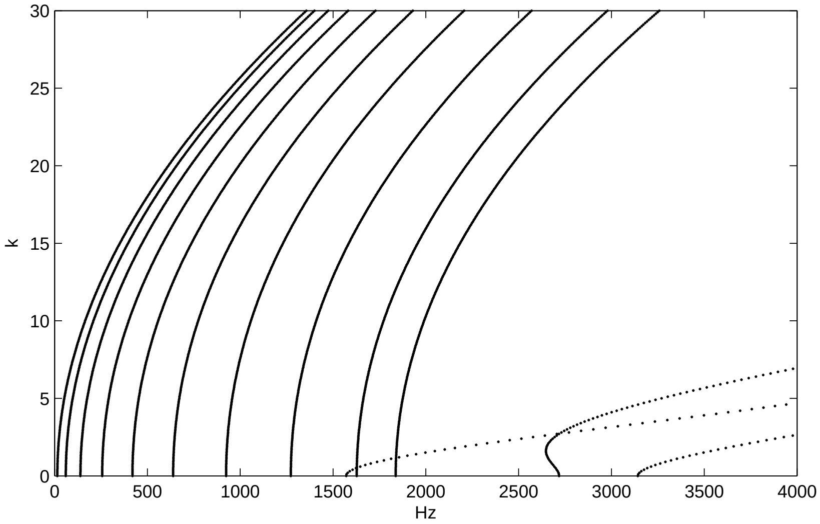

Figure B.6: FE model strip plate dispersion relations with solid elements

In fig. B.6 are represented the dispersion relations for the plate modeled with solid eight nodes elements. In fig. B.7 are showed the first three modeshapes for the plate modeled with solid elements. As it can be seen there are some differences in the frequency of the modeshape, that increase with the increasing of the modeshape number, this is due to the type and number of elements used. Increasing the number of elements for both models this difference decreases.

Response due to a point force

As show in the above section the mobility of the plate can be obtained multiplying the outputs of the point force frequency response, obtained with the numerical integration, by $j\omega$

Fig. B.8 shows the comparison between the analytical point mobility and the numerical point mobility of the plate modelled with solid FE. It can be noticed that at low frequency there is a very good agreement between the analytical and the numerical solution. Growing with the frequencies the numerical solution becomes less accurate, this could be because of the FE discretization.

From the numerical integration in WANDS also the dispersion curves are obtained. These can be compared with the ones obtained with the analytical model and by the system matrices.

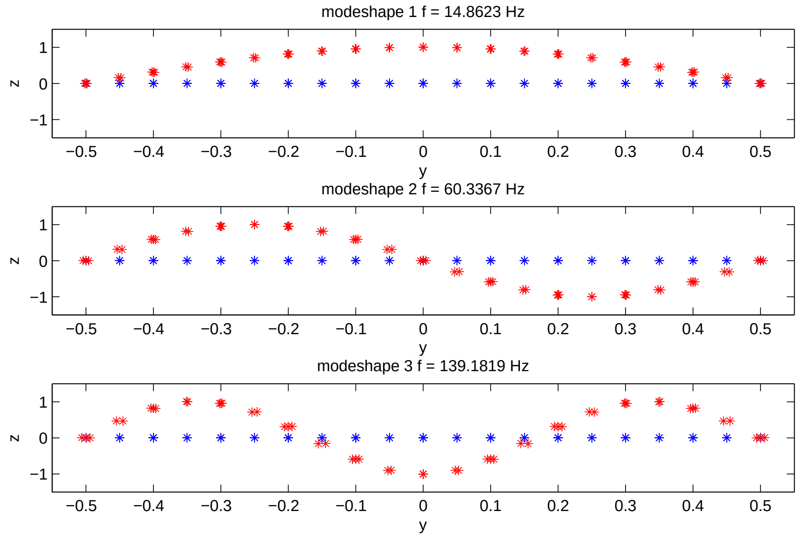

Figure B.7: FE model strip plate modeshapes with solid elements normalized by the maxima of each modeshape

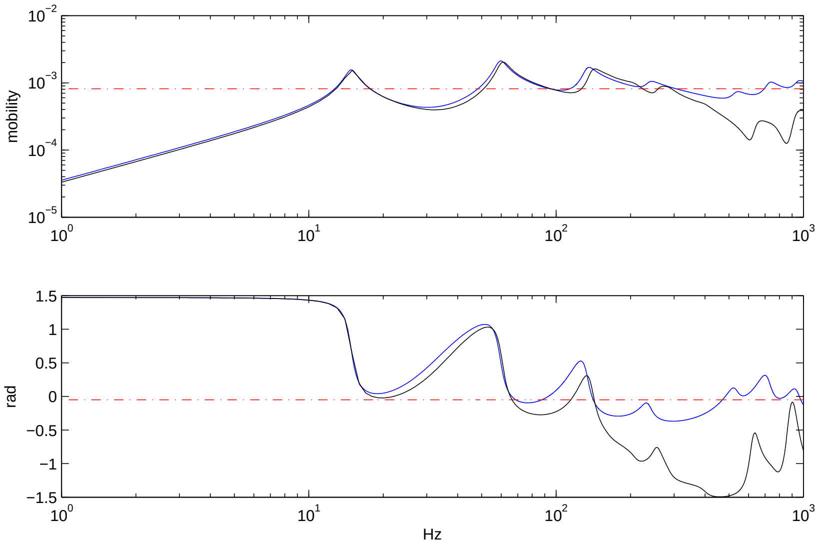

Figure B.8: Comparison between analytical point mobility and numerical point mobility for the same value of the loss factor $\eta = 0.1$

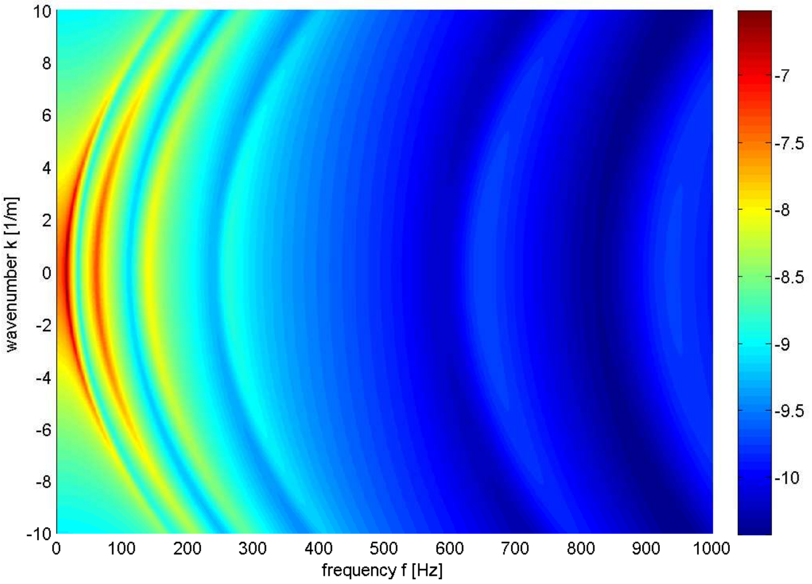

Figure B.9: Dispersion curves of the plate described with solid FE obtained with the numerical integration

Fig.B.9 shows the dispersion curves for the plate described with the solid FE method. The higher picks correspond to the dispersion curves. From fig. B.9 can be seen that the cut-on frequencies correspond to the ones obtained with the analytical solution. Since the damping is considered the dispersion curves are spread over the whole are of the frequency wavenumber range considered.

Fig. B.10 shows the displacements of the plate along the X direction per every frequency. It can be seen that waves at lower cut-on frequencies propagate further than waves at higher cut-on frequencies.

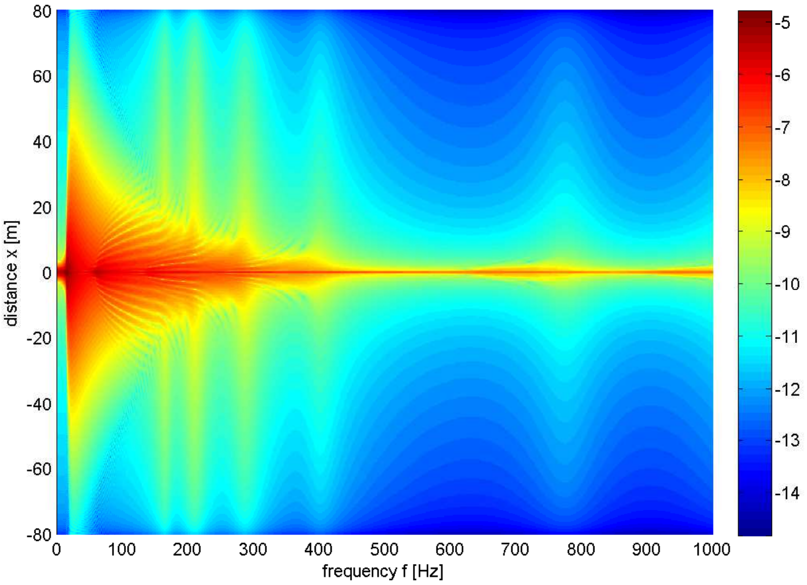

Figure B.10: Displacements in the X direction per every frequency

Appendix C

Analytical point mobility of infinite plate strip

In order to solve equation B.9 the boundary conditions have to be applied. For a force applied at $x = 0$ it should be noted that, to ensure that waves decay in both directions, $A_{1,m}$ and $A_{2,m}$ are zero in the region $x \geq 0$ while $A_{3,m}$ and $A_{4,m}$ are zero in the region $x \leq 0$. These assumptions give as result that the out of plane displacement of the infinite plate strip, for every mode m, becomes

$$w_m(x \leq 0, y) = A_{1,m} e^{jk_{x_1,m}x} + A_{2,m} e^{jk_{x_2,m}x} \tag{C.1}$$

$$w_m(x \geq 0, y) = A_{3,m} e^{-jk_{x_1,m}x} + A_{4,m} e^{-jk_{x_2,m}x} \tag{C.2}$$

The generalized force acting on the m^{th} order motion is

$$F_m = \frac{2F}{L} \sin\left(\frac{m\pi y_0}{L}\right) \tag{C.3}$$

The boundary conditions for this structure evalueted at $x = 0$ are

- Continuity equation: $w_m(0)_- = w_m(0)_+$

$$A_{1,m} + A_{2,m} = A_{3,m} + A_{4,m} \tag{C.4}$$

- Continuity of rotation: $\frac{\partial w_m}{\partial x}\Big|_{x=0_-} = \frac{\partial w_m}{\partial x}\Big|_{x=0_+}$

$$jk_{x_1,m}A_{1,m} + jk_{x_2,m}A_{2,m} = -jk_{x_1,m}A_{3,m} - jk_{x_2,m}A_{4,m} \tag{C.5}$$

- Continuity of bending moment: $\left.\frac{\partial^2 w_m}{\partial x^2}\right|_{x=0_-} = \left.\frac{\partial^2 w_m}{\partial x^2}\right|_{x=0_+}$

$$-k_{x_1,m}^2 A_{1,m} - k_{x_2,m}^2 A_{2,m} = -k_{x_1,m}^2 A_{3,m} - k_{x_2,m}^2 A_{4,m} \tag{C.6}$$

- Force equilibrium condition: $S_m(0,y)_+ - S_m(0,y)_- = F_m$

$$\begin{aligned}&\left(\left[jA_{3,m}k_{x_1,m}^3 + jA_{4,m}k_{x_2,m}^3\right] - \left[(2-\nu)\left[-jA_{3,m}k_{x_1,m} - \right.\right.\right.\\ &\left.\left.\left. -jA_{4,m}k_{x_2,m}\right]\left(\frac{m\pi}{L}\right)^2\right]\right) - \left(\left[-jA_{1,m}k_{x_1,m}^3 - jA_{2,m}k_{x_2,m}^3\right] - \right.\\ &\left. - \left[(2-\nu)\left[jA_{1,m}k_{x_1,m} + jA_{2,m}k_{x_2,m}\right]\left(\frac{m\pi}{L}\right)^2\right]\right) = \frac{F_m}{D}\end{aligned} \tag{C.7}$$

From the boundary conditions four equations are obtained. Solving the four equations if four variables problem the coefficients $A_{1,m}$, $A_{2,m}$, $A_{3,m}$ and $A_{4,m}$ are obtained. From equation (C.4) and equation (C.6) the following relations are obtained

$$A_{1,m} = A_{3,m} \tag{C.8}$$

$$A_{2,m} = A_{4,m} \tag{C.9}$$

$$A_{4,m} = -\frac{k_{x_1,m}}{k_{x_2,m}} A_{3,m} \tag{C.10}$$

By solving the system of equations can be found that

$$A_{1,m} = \frac{-jF_m}{2Dk_{x_1,m}\left(k_{x_1,m}^2 - k_{x_2,m}^2\right)} \tag{C.11}$$

Based on these coefficients, the solution may be written as follows

$$w_m(x \le 0) = \frac{-jF_m}{2Dk_{x_1,m}\left(k_{x_1,m}^2 - k_{x_2,m}^2\right)}\left[e^{jk_{x_1,m}x} - \frac{k_{x_1,m}}{k_{x_2,m}} e^{jk_{x_2,m}x}\right] \tag{C.12}$$

$$\begin{aligned}w_m(x \ge 0) = \frac{-jF_m}{2Dk_{x_1,m}\left(k_{x_1,m}^2 - k_{x_2,m}^2\right)} &\left[e^{-jk_{x_1,m}x} - \right.\\ &\left. - \frac{k_{x_1,m}}{k_{x_2,m}} e^{-jk_{x_2,m}x}\right]\end{aligned} \tag{C.13}$$

The complete solution is than given by

$$\begin{aligned} w_m(x \leq 0, y) = \sum_{m=1}^{\infty} \frac{-jF_m}{2Dk_{x_1,m}\left(k_{x_1,m}^2 - k_{x_2,m}^2\right)} \Big[e^{jk_{x_1,m}x} - \\ - \frac{k_{x_1,m}}{k_{x_2,m}} e^{jk_{x_2,m}x} \Big] \sin\left(\frac{m\pi y}{L}\right) \end{aligned} \tag{C.14}$$

$$\begin{aligned} w_m(x \geq 0, y) = \sum_{m=1}^{\infty} \frac{-jF_m}{2Dk_{x_1,m}\left(k_{x_1,m}^2 - k_{x_2,m}^2\right)} \Big[e^{-jk_{x_1,m}x} - \\ - \frac{k_{x_1,m}}{k_{x_2,m}} e^{-jk_{x_2,m}x} \Big] \sin\left(\frac{m\pi y}{L}\right) \end{aligned} \tag{C.15}$$

From equation (C.14) and equation (C.15) the mobility for the infinite plate strip $Y = \frac{\dot{w}}{F} = j\omega\frac{w}{F}$ can be derived as

$$\begin{aligned} Y(x, y, \omega) = j\omega \sum_{m=1}^{\infty} \frac{-j\frac{2}{L}\sin\left(\frac{m\pi y_0}{L}\right)}{2Dk_{x_1,m}\left(k_{x_1,m}^2 - k_{x_2,m}^2\right)} \Big[e^{-jk_{x_1,m}|x|} - \\ - \frac{k_{x_1,m}}{k_{x_2,m}} e^{-jk_{x_2,m}|x|} \Big] \sin\left(\frac{m\pi y}{L}\right) \end{aligned} \tag{C.16}$$

Appendix D

WANDS FE theory

A variation of a Lagrangian is defined by

$$\delta L = \int_{t_1}^{t_2} \delta(U - T) - \delta W \, dt \tag{D.1}$$

where δ denotes first variation, t_1 and t_2 are the interval ends, U and T are the potential and kinetic energies and δW is the virtual work of the forces. In the absence of other systems Hamilton's modified principle states that for any given t_1 and t_2

$$\delta L = 0 \tag{D.2}$$

This means that the system state at t_1 and t_2 is irrelevant, given that harmonic motion over a long period of time is considered. Thus, t_2 and t_1 may tend to $\pm\infty$ respectively without any loss of information.

Parseval's identity for two real valued functions, $f(t)$ and $g(t)$ yields

$$\int_{-\infty}^{+\infty} f(t)g(t) \, dt = \int_{-\infty}^{+\infty} \hat{f}(\omega)^* \hat{g}(\omega) \, d\omega \tag{D.3}$$

where t is time, ω is the angular frequency, * denotes complex conjugate and $\hat{}$ denotes the Fourier transform. Applying Parseval's identity on equation (D.1) gives

$$\delta L(\omega) = \int_{-\infty}^{+\infty} \delta U(\omega) - \delta T(\omega) - \delta W(\omega) \, d\omega \tag{D.4}$$

Calculate response at different frequencies are independent when linear systems are considered. Consequently, a variation formulation defined for each frequency is given by

$$\delta L_\omega = \delta U(\omega) - \delta T(\omega) - \delta W(\omega) \tag{D.5}$$

Depending on what element type it's used there is a different formulation of the potential and kinetic energies

D.1 Plate elements

In order to solve equation (D.5) all the single terms have to be identified for the plate element.

Potential energy

Following thin plate theory and considering the frequency domain the first variation of potential energy in an area A may be written as

$$\delta U = \int_A \begin{bmatrix} \delta\varepsilon^H & \delta\kappa^H \end{bmatrix} \boldsymbol{D} \begin{bmatrix} \varepsilon \\ \kappa \end{bmatrix} dA \tag{D.6}$$

where ε are the strains and κ are the curvatures of the plate.

As shown in [20] it can be seen that the potential energy can be written as

$$\int \sum_{i=0}^{2} \sum_{j=0}^{2} \frac{\partial^i \delta\tilde{u}^H}{\delta x^i} a_{ij} \frac{\delta^j \tilde{u}}{\delta x^j} \, dx \tag{D.7}$$

This can be seen as a weak form equation for the potential energy.

Kinetic energy

The first variation of the kinetic energy in the frequency domain is

$$\delta T = \int_A \rho h \begin{bmatrix} \delta u^* & \delta v^* & \delta w^* \end{bmatrix} \begin{bmatrix} u \\ v \\ w \end{bmatrix} dA \tag{D.8}$$

With the approximation of chapter 4 of [20] the kinetic energy becomes

$$\delta T = \int_x \delta\tilde{u}^H m_2 \tilde{u} \, dx \tag{D.9}$$

Inserting variations of potential and kinetic energies into Hamilton's principle, followed by integration by parts while neglecting boundary terms of the ends of the waveguide and subsequently applying calculus of variation yields

$$\left[\boldsymbol{K_4}\frac{\partial^4}{\partial x^4}+\boldsymbol{K_2}\frac{\partial^2}{\partial x^2}+\boldsymbol{K_1}\frac{\partial}{\partial x}+\boldsymbol{K_0}-\omega^2\boldsymbol{M_2}\right]\tilde{u}-\tilde{f}=0 \tag{D.10}$$

Where ω is the round frequency. The program WANDS gives as output the matrices $\boldsymbol{K_4}$, $\boldsymbol{K_2}$, $\boldsymbol{K_1}$, $\boldsymbol{K_0}$ and $\boldsymbol{M_2}$.

D.2 Solid elements

In order to solve equation (D.5) all the single terms have to be identified for the solid element.

Potential energy

The first variation of potential energy in the frequency domain is given by

$$\delta U(\omega)=\int_V \delta\hat{\varepsilon}^H\boldsymbol{D}\hat{\varepsilon}\,dV \tag{D.11}$$

This can be rewrite as

$$\delta U(\omega)=\int_x \frac{\partial^i\delta\tilde{u}}{\partial x^i}\sum_{i=0}^{1}\sum_{j=0}^{1}a_{ij}\frac{\partial^j\tilde{u}}{\partial x^j}\,dx \tag{D.12}$$

Kinetic energy

The first variation of the kinetic energy in the frequency domain is given by

$$\delta T(\omega)=\omega^2\int_x \delta\tilde{u}^H\boldsymbol{m_2}\tilde{u}\,dx \tag{D.13}$$

External forces

The virtual energy in the frequency domain is given by

$$\delta W(\omega)=\int_x \delta\tilde{u}^H\tilde{f}\,dx \tag{D.14}$$

Inserting the expressions for δU, δT and δW in equation (D.5) yields

$$\delta L_\omega = \int_x \sum_{i=0}^{1} \sum_{j=0}^{1} \frac{\partial^i \delta \tilde{u}}{\partial x^i} a_{ij} \frac{\partial^j \tilde{u}}{\partial x^j} - \omega^2 \delta \tilde{u}^H \boldsymbol{m_2} \tilde{u} - \delta \tilde{u}^H \tilde{f} \, dx \tag{D.15}$$

This equation may be denoted as the weak form of the waveguide-FE model.

Hamilton's principle integration by parts with respect to the x-coordinate and calculus of variation yields

$$\left[\boldsymbol{K_2} \frac{\partial^2}{\partial x^2} + \boldsymbol{K_1} \frac{\partial}{\partial x} + \boldsymbol{K_0} - \omega^2 \boldsymbol{M_2} \right] \tilde{u} - \tilde{f} = 0 \tag{D.16}$$

Appendix E

Traction vector

The traction vector is related to the shape functions of the boundary element and since it is in WANDS only the quadratic boundary element is implemented, its shape functions are described in equation (E.1)

$$\begin{cases} \phi_1(\xi) = \frac{1}{2}\xi(\xi - 1) \\ \phi_2(\xi) = 1 - \xi^2 \\ \phi_3(\xi) = \frac{1}{2}\xi(\xi + 1) \end{cases} \tag{E.1}$$

where $-1 \leq \xi \leq 1$ is the non dimensional local coordinate of the boundary element $\xi = y/a$, where a is half of the boundary element length. In equation (E.1) the number 1, 2 and 3 correspond to the local nodes of the element.

Fig. E.1 shows the shape functions for the three nodes of the boundary element.

There is an issue on the point of application of the force and the shape functions. If the equivalent point force is applied to the center node of an element than the traction vector is spread over the same boundary element with a shape equal to the shape function ϕ_2. The equivalent point force is

$$F_{eq} = a \int_{-1}^{1} \phi_2(\xi) p \, d\xi \tag{E.2}$$

where F_{eq} is the equivalent point force at the center node of the boundary element for the given traction vector p. If the point force is applied to a node at the edge of the boundary element the traction vector is spread on both element that the node describes. The shape of the traction vector is than

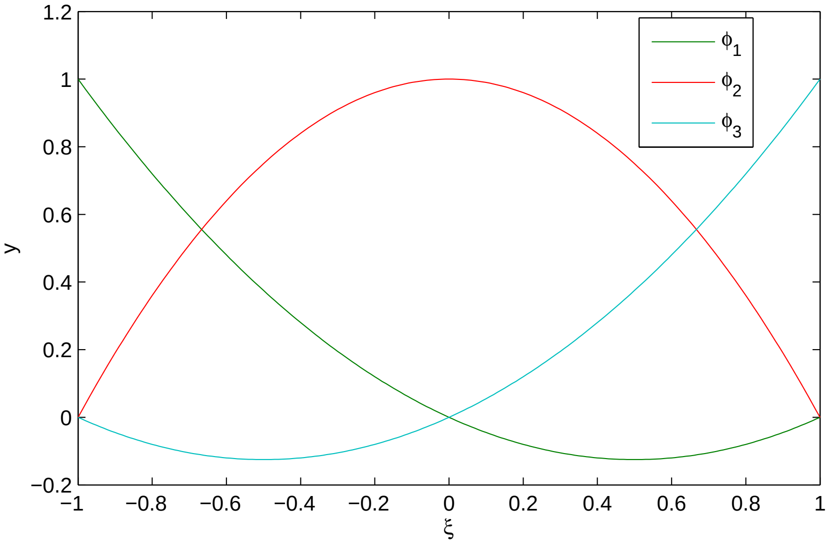

Figure E.1: Shape functions for the three nodes of the boundary element

the union of shape function $\phi_3(\xi)$ for the boundary element at the left of the node and $\phi_1(\xi)$ for the element at the right of the node. The equivalent point force is than calculated as

$$F_{eq} = a \int_{-1}^{1} [\phi_1(\xi) + \phi_3(\xi)]\, p\, d\xi \tag{E.3}$$

Since in wands to the boundary elements can not be applied a point force but only a traction vector it is necessary to understand what is the equivalent traction vector in order to obtain the point force wanted. To do so is than needed to know at which node of the boundary element is applied the point force, than a simple loop on the residual of the equivalent force obtained with equation (E.2) or (E.3) whit as variable the traction vector p has to be used. This returns the equivalent traction vector to be given as input to WANDS in order to obtain a desired point force on the boundary element.

In this thesis the trapezoidal numerical integration has been used in order to obtain the equivalent point force. In particular the MatLab implemented routine *trapz* has been used.

Bibliography

[1] P. Grootenhuis. Floating track slab isolation for railways. *Journal of Sound and Vibration*, 51:443–448, 1977.

[2] B. Hemsworth. Reducing groundborne vibrations: State-of-the-art study. *Journal of Sound and Vibration*, 231(3):703–709, March 2000.

[3] X. Sheng, C. J. C. Jones, and M. Petyt. Ground vibration generated by a load moving along a railway track. *Journal of Sound and Vibration*, 228(1):129–156, November 1999.

[4] K. Popp, H. Kruse, and I. Kaiser. Vehicle-Track Dynamics in the Mid-Frequency Range. *Vehicle System Dynamics*, 31(5-6):423–464, June 1999.

[5] S. Alfi and S. Bruni. Mathematical modelling of train–turnout interaction. *Vehicle System Dynamics*, 47(5):551–574, April 2009.

[6] E. Kassa, C. Andersson, and J. C. O. Nielsen. Simulation of dynamic interaction between train and railway turnout. *Vehicle System Dynamics*, 44(3):247–258, March 2006.

[7] H. Hertz. On the contact of elastic solids. *Journal für die Reine und Angewandte Mathematik*, 92:156–171, 1881.

[8] A. A. Shabana, K. E. Zaazaa, J. L. Escalona, and J. R. Sany. Development of elastic force model for wheel/rail contact problems. *Journal of Sound and Vibration*, 269(1-2):295–325, January 2004.

[9] S. Bruni, A. Collina, G. Diana, and P. Vanolo. Lateral dynamics of a railway vehicle in tangent track and curve: tests and simulation. *Supplement to Vehicle System Dynamics*, 33:464–477, 2000.

[10] D. J. Thompson. *Railway noise and vibration: mechanisms, modelling and means of control*. Elsevier Science, 2009.

[11] J. A. Forrest and H. E. M. Hunt. A three-dimensional tunnel model for calculation of train-induced ground vibration. *Journal of Sound and Vibration*, 294(4-5):678–705, July 2006.

[12] J. A. Forrest and H. E. M. Hunt. Ground vibration generated by trains in underground tunnels. *Journal of Sound and Vibration*, 294(4-5):706–736, July 2006.

[13] X. Sheng, C. J. C. Jones, and D. J. Thompson. Ground vibration generated by a harmonic load moving in a circular tunnel in a layered ground. *Low Frequency Noise, Vibration and Active Control*, 22:83–96, 2003.

[14] A. H. D. Cheng and D. T. Cheng. Heritage and early history of the boundary element method. *Engineering Analysis with Boundary Elements*, pages 268–302, 2005.

[15] K. H. Chua, K. W. Lo, and T. Balendra. Building response due to subway train traffic. *Journal of Geotechnical Engineering*, 121:747–754, 1995.

[16] D. Clouteau, M. Arnst, T. M. Al-Hussaini, and G. Degrande. Freefield vibrations due to dynamic loading on a tunnel embedded in a stratified medium. *Journal of Sound and Vibration*, 283(1-2):173–199, May 2005.

[17] M. G. Floquet. Sur les équations différentielles linéaires à coefficients périodiques. *Annales Scientifiques de l'École Normale Supérieure*, 12:47–88, 1883.

[18] D. Clouteau, D. Aubry, and G. Bonnet. Modeling of wave propagation due to fixed or mobile sources. *Wave propagation and reduction of vibrations*, pages 109–121, 1994.

[19] X. Sheng, C. J. C. Jones, and D. J. Thompson. Prediction of ground vibration from trains using the wavenumber finite and boundary element methods. *Journal of Sound and Vibration*, 293(3-5):575–586, June 2006.

[20] C. M. Nilsson and C. J. C. Jones. *Theory Manual for WANDS 2.1*, August 2007.

[21] J. T. Nelson and H. J. Saurenman. A Prediction Procedure for Rail Transportation Ground-Borne Noise and Vibration. *Transportation Research Record*, 1143:26–35, 1987.

[22] R. J. Greer. AEL methodology for the prediction of the re-radiated noise in residential buildings from trains travelling in tunnels. In *INTER-NOISE and NOISE-CON Congress and Conference Proceedings*, volume 1993, pages 483–488. Institute of Noise Control Engineering, 1993.

[23] R. A. Hood, R. J. Greer, M. Breslin, and P. R. Williams. The calculation and assessment of ground-borne noise and perceptible vibration from trains in tunnels. *Journal of Sound and Vibration*, 193(1):215–225, May 1996.

[24] N. Triepaischajonsak. *The influence of various excitation mechanisms on ground vibration from trains.* PhD thesis, February 2012.

[25] F. Cheli and R. Corradi. On rail vehicle vibrations induced by track unevenness: Analysis of the excitation mechanism. *Journal of Sound and Vibration*, 330(15):3744–3765, July 2011.

[26] G. Degrande, M. Schevenels, P. Chatterjee, W. Van de Velde, P. Hölscher, V. Hopman, A. Wang, and N. Dadkah. Vibrations due to a test train at variable speeds in a deep bored tunnel embedded in London clay. *Journal of Sound and Vibration*, 293(3-5):626–644, June 2006.

[27] F. Braghin, S. Bruni, and G. Diana. Experimental and numerical investigation on the derailment of a railway wheelset with solid axle. *Vehicle System Dynamics*, 44:305–325, April 2006.

[28] F. E. Richart, J. R. Hall, and R. D. Woods. *Vibrations of soils and foundations.* Prentice-Hall, 1970.

[29] K. F. Graff. *Wave motion in elastic solids.* Oxford University press, 1975.

[30] X. Sheng, C. J. C. Jones, and D. J. Thompson. Modelling ground vibration from railways using wavenumber finite- and boundary-element methods. *Proceedings of the Royal Society A: Mathematical, Physical and Engineering Science*, 461(2059):2043–2070, July 2005.

[31] J. P. Berenger. A Perfectly Matched Layer for the Absorption of Electromagnetic Waves. *Journal of Computational Physics*, (114), 1994.

[32] K. Shin and J. K. Hammond. *Fundamentals of Signal Processing for sound and vibration engineers*. Wiley, 2008.

[33] S. M. Han, H. Benaroya, and T. Wei. Dynamics of transversely vibrating beams using four engineering theories. *Journal of Sound and Vibration*, 225(5):935–988, September 1999.

[34] F. Schmid. *Wheel-Rail Best Practice Handbook*. University of Birmingham, 2010.

[35] S. Gupta, G. Degrande, and G. Lombaert. Experimental validation of a numerical model for subway induced vibrations. *Journal of Sound and Vibration*, 321(3-5):786–812, April 2009.

[36] Altavia. *Infrastrutture delle grandi opere*.

[37] Cahier des charges pour un bogie a caracteristiques ameliorees pour la circulation ed courbe. Technical report.

[38] E. Kausel and J. M. Roesset. Stiffness matrices for layered soils. In *Bulletin of the Seismological Society of America*, volume 71, pages 1743–1761, December 1981.

[39] A. Nordborg. Vertical Rail Vibrations: Pointforce Excitation. *Acta Acustica united with Acustica*, pages 280–288.

[40] U. Orrenius and S. Finnveden. Calculation of wave propagation in rib-stiffened plate structures. *Journal of Sound and Vibration*, 198(2):203–224, November 1996.

[41] I. Bartoli, A. Marzani, F. Lanza di Scalea, and E. Viola. Modeling wave propagation in damped waveguides of arbitrary cross-section. *Journal of Sound and Vibration*, 295(3-5):685–707, August 2006.

List of Figures

List of Tables